Raman spectroscopy of graphene: probing phonons, electrons and electron-phonon interactions

Leandro Malard Moreira

Raman spectroscopy of graphene: probing phonons, electrons and electron-phonon interactions

Leandro Malard Moreira

Orientador: Prof. Marcos Assunção Pimenta

Tese de doutorado apresentado à UNIVERSIDADE FEDERAL DE MINAS GERAIS.

Setembro de 2009

Agradecimentos

À minha família, pelo amor e apoio.

À Tati, pelo seu amor e por me aguentar falando de trabalho.

Ao Markin, pela excelente orientação e por dar apoio às minhas ídeias que quase sempre dão errado. Por me ensinar a ser crítico e ver que fênomenos físicos complicados podem ser entendidos de uma maneira simples. Pela sua amizade, cervejadas e churrascadas no Tangará.

Ao Ado, pela sua contagiante visão da nanociencia. Por todas as discussões de física ou de bobagem mesmo. Por me lembrar que existem algumas músicas da década de 80 que prestam, pelo menos uma, Katia Flávia.

Ao Gusta e ao Cris, pela grande ajuda no meu doutorado com discussões e ajudas técnicas no lab.

Aos ramanistas, e aos nearfieldistas pelos inúmeros galhos quebrados, amizade e muiiiitooos cafés.

A todo corpo técnico e aos funcionários do departamento de física, porque sem eles não existe ciência. Em especial à Idalina por toda sua dedicação.

A todos os professores do departamento, pela ótima convivência, empréstimos de material (que não foram poucos) e discussões pelos corredores. Em especial, ao Mário Sérgio, Chacham, Elmo e Sampaio por sanar minhas dúvidas de estado sólido.

Ao Daniel, Juliana, Thiago, Jorge, Elmo e Flávio pela colaboração científica.

Ao Antônio Castro Neto, pelas discussões no grafeno e constantes visitas.

To Millie Dresselhaus for all the discussions and important insights on the

aspects of the carbon nanoscience.

À roça do custela, da Fê e da Júlia, à Fazenda da Barra e ao Emprale.

A todos os amigos!!!

Ao Kimmel.

Ao CNPq, à CAPES, à FAPEMIG e à Nacional de Grafite, que também acreditam na pesquisa científica de qualidade no Brasil.

Figure 0.1: First picture from top to bottom left to right: Vladmir, Leo Campos, Paulo Araújo, Ado Jório, Daniela Mafra, Leandro Malard (Xubaka), Mathias Steiner, Rodrigo Gribel, Daisuke Nishide, Luiz Gustavo Cancado, Marcos Pimenta and Ana Paula Gomes. Second picture from left to right: Paulo, Leo, Mario Hoffman, Xubaka, Tati, Marcos, Ya Ping, Luciano Moura, Cristiano Fantini and Pedro Pesce.

Ao doutorado pelo crescimento profissional e pessoal. Muito obrigado.

Resumo

Desde a identificação de uma ou poucas camadas de grafeno em um substrato em 2004, trabalhos intensivos têm sido feitos para se caracterizar esse novo material. Em particular, a espectroscopia Raman tem sido muito importante para a elucidar propriedades físicas e químicas em sistemas de grafeno. A espectroscopia Raman ressonante também vem se mostrado como uma ferramenta importante para se estudar fônons, elétrons e interações elétron-fônon em grafeno.

Nesta tese, ao usarmos diferentes energias de laser de excitação, nós obtivemos propriedades importantes sobre as estruturas eletrônicas e vibracionais para uma e duas camadas de grafeno. Para uma monocamada de grafeno, nós determinamos a dispersão de fônons perto do ponto de Dirac para o modo óptico transversal no plano (iTO) e para o modo acústico longitudinal no plano (iLA). Comparamos nossos resultados experimentais com cálculos téoricos recentes para a dipersão de fônons nas proximidades do ponto K. Para a bicamada de grafeno, nós obtivemos os parâmetros de estrutura eletrônica do modelo de Slonczewski-Weiss-McClure. Nossos resultados mostram que a bicamada de grafeno possue uma forte assimetria eletron-buraco, que por sua vez é mais forte que no grafite.

Em experimentos aplicando uma tensão de porta, variamos o nível de Fermi em uma bicamanda de grafeno, o que levou uma quebra de simetria, deixando assim ambos os modos de vibração simétricos (S) e anti-simétricos (AS) ativos em Raman. A dependência da energia e do amortecimento desses modos de fônons com a energia de Fermi é explicada através do acoplamento elétron-fônon, que é distinto entre os fônons A e AS com pares elétron-buraco intra- ou inter- banda. Nossos resultados experimentais deram suporte às previsões teóricas para interações elétron-fónon em uma bicamada de grafeno.

Estudamos também, através de teoria de grupo, as propriedades de simetria de elétrons e fônons em sistemas de N-camadas de grafeno. Derivamos as regras de seleção para interações elétron-luz e elétron-fônon em todos os pontos da primeira zona de Brillouin. Ao considerarmos estas regras de seleção, nós discutimos o mecanismo de espalhamento Raman de dupla ressonância em função do número de camadas. As regras de seleção para a mono- e a bi-camada, também foram discutidas na presença de um campo elétrico perpendicular ao plano da amostra.

Abstract

Since the identification of mono and few graphene layers in a substrate in 2004, intensive work has been devoted to characterize this new material. In particular, Raman spectroscopy played an important role in unraveling the properties of graphene systems. Moreover resonant Raman scattering (RRS) in graphene systems was shown to be an important tool to probe phonons, electrons and electron-phonon interactions.

In this thesis, by using different laser excitation energies, we obtain important electronic and vibrational properties of mono- and bi-layer graphene. For monolayer graphene, we determine the phonon dispersion near the Dirac point for the in-plane transverse optical (iTO) mode and the in-plane longitudinal acoustic (iLA) mode. These results are compared with recent theoretical calculations for the phonon dispersion around the K point. For bilayer graphene we obtain the Slonczewski-Weiss-McClure band parameters. These results show that bilayer graphene has a strong electron-hole asymmetry, which is larger than in graphite.

In a gating experiment, we observe that the change in Fermi level of bilayer graphene gives rise to a symmetry breaking, allowing the observation of both the symmetric (S) and anti- symmetric (AS) phonon modes. The dependence of the energy and damping of these phonons modes on the Fermi level position is explained in terms of distinct couplings of the S and AS phonons with intra- and inter-band electron-hole transitions. Our experimental results confirm the theoretical predictions for the electron-phonon interactions in bilayer graphene.

We also study the symmetry properties of electrons and phonons in graphene systems as a function of the number of layers, by a group theory approach. We derive the selection rules for the electron-radiation and for the electron-phonon interactions at all points in the Brillouin zone. By considering these selection rules, we address the double resonance Raman scattering process. The selection rules for monolayer and bilayer graphene in the presence of an applied electric field perpendicular to the sample plane are also discussed.

Contents

CHAPTER 1

Introduction

1.1 Why study graphene?

The study of carbon materials is one of the most exciting fields in basic and applied science research, and applications of these materials in industry have been grown since the discovery of graphite many centuries ago[1]. Graphite has been largely used as lubricants, steelmaking, batteries components and, of course, as a writing material. However, it was only around 1950 that the electronic structure of graphite was studied in depth [1, 2]. Experimental work devoted to the understanding of the electronic transport, electronic structure, vibrational and mechanical properties of graphite started after the production of synthetic graphite, namely Highly Oriented Pyrolytic Graphite (HOPG).

The next step in the carbon research came with the fabrication of other forms of carbon, which contributed greatly to the beginning of the nanotechnology [2]. The zero-dimensional form of carbon, the fullerene was discovered in 1985 by Harold Kroto, Richard Smalley and Robert Curl [3]. This discovery was an important step into the nanotechnology world and until today there is considerable research effort to understand and apply its physical properties. Some years later, in 1991 the one-dimensional form of carbon, the carbon nanotubes, was discovered by Ijima [4]. Carbon nanotube turns out to be also a hot research topic, due to its interesting physical properties. It can be a semiconductor or a metal depending on the chiral indices, it is one of the materials with highest Young modulus, and it conducts heat. The two-dimensional form of carbon bounded in a sp-2 configuration is

---

[1] Graphite was named by by Abraham Gottlob Werner, a German geologist, in 1789.

[2] The concept of nanotechnology was first introduced in a talk given by the physicist Richard Feynman at an American Physical Society meeting at Caltech on December 29, 1959.

named graphene[3]. Graphene is only one atom thick, and it represents the basic form of the other kinds of carbon systems described above. Graphite is formed by stacking of graphene layers, carbon nanotubes are rolled graphene sheets and fullerenes are cuts of graphene bulk in a form of a ball (see Fig. 1.1).

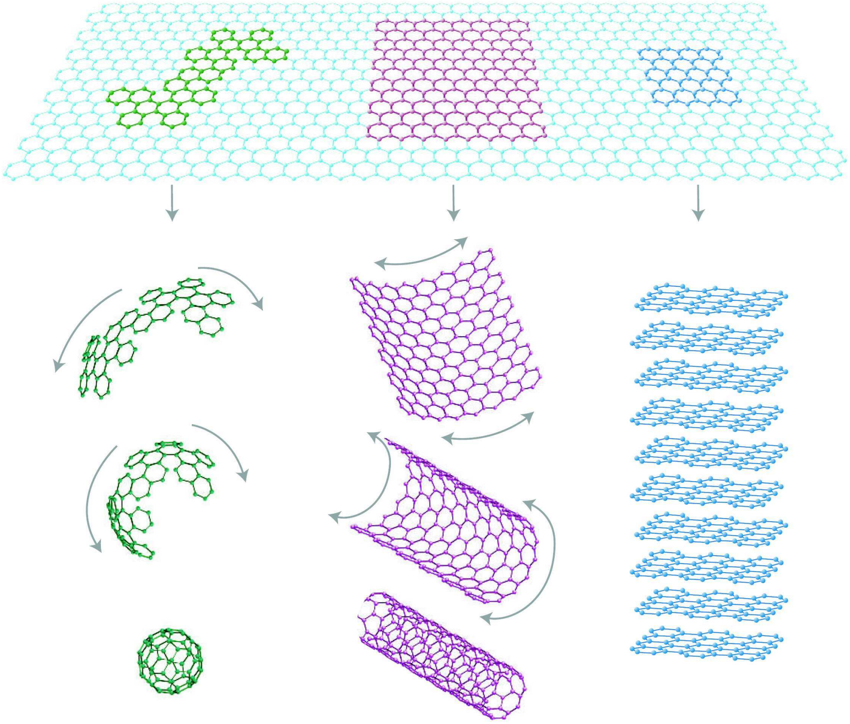

Figure 1.1: Diagram showing how graphene can be transformed into fullerenes, carbon nanotubes and graphite. Adapted from Ref. [5]

However pure two-dimensional systems were believed not to exist in nature, since it would be thermodynamically unfavorable [6], and it should bulk into some tri-dimensional form [4]. Some efforts have been previously made to produce graphene, but only in 2004 it was possible for the first time to identify and measure this one-atom thick material [8, 9]. Since then, graphene turns out to be also a very exciting material, since it shows an unusual quantum Hall effect [10, 11], can sustain very high electrical currents without deterioration, is also one

---

[3] In the sp-2 configuration, the 2s and two 2p orbitals mix to form three in plane covalent bonds. Each carbon atom has three nearest neighbors, forming a hexagonal planar network of graphene.

[4] In fact it was experimentally proposed that freely suspendended graphene has ripples [7], and thus it is not a truly two-dimensional system.

of the materials with high young modulus, its electrons move through large distances (few microns) without dissipation (for a review of these properties see Refs. [5, 12]). Also the electron dispersion is described by the Dirac equation, where the electrons have no mass [13]. Therefore, for the first time, it is possible to engineer relativistic quantum phenomena in a *table-top* experiment [10, 11, 14, 13].

Most of the graphene applications euphoria is due to its capacity of integration with electronic circuits. Graphene has one the largest electron mobilities at room temperature, and much effort has been done to improve this property. Large mobility means less dissipation in the form of heat giving rise to fast electronic devices. Unlike semiconducting nanotubes, graphene is metallic, and, in principle, it is unlikely that grapene can act as a field effect transistor with high ON/OFF ratios. However, gap opening can occur by confinement of the electron wavefunction in one direction, like in graphene nanoribbons [15, 16, 17], or by chemical modification of graphene.

Graphene nanoribbons present very interesting phenomena, where physical properties like electronic structure and spin transport depend on the width and geometrical structures of the edges [15, 16, 17]. However, unlike carbon nanotubes, which exhibit metallic or semiconducting behavior, graphene nanoribbons are expected to show only a semiconducting behavior [17]. This is a good property for transistor applications, where the existence of a gap is desirable. Moreover, the edges of the nanoribbons can be chemically modified in order to change their physical properties. In another approach, chemical modification of graphene like hydrogenation (the so-called graphane) has been done [18], showing a possible gap in the electronic structure.

Bilayer graphene also exhibit many interesting phenomena. However, bilayer graphene does not exhibit a linear electronic dispersion. Instead, its electronic dispersion is described by a zero gap parabolic equation [13]. Moreover, bilayer graphene shows a different type of quantum Hall effect [19] and one the most striking features of bilayer is the fact that a gap can be opened by applying a perpendicular electric field [20, 21, 22, 23, 24], and this gap can be tuned by the strength of this electric field.

The industrial application of graphene depends on large scale production methods [12]. The mechanical exfoliation of graphene (pelling of graphite with a scotch tape) done in the work of Novoselov *et al.* in 2004 [8, 9] succeed in producing graphene with very large quality (high electron mobility at room temperature), but this sample preparation method is difficult to be integrated into a production line. Large scale methods like ultrasonification of graphite in solvents [25, 26] and epitaxial growth on Ni [27] or silicon carbide surfaces have been successfully reported recently [28, 29, 30]. Although the electronic properties of these types of graphene samples are not so good and less uniform as compared to exfoliated graphene, these methods present important steps towards industrialization of graphene. Figure 1.2 shows four different types of graphene samples prepared by different techniques.

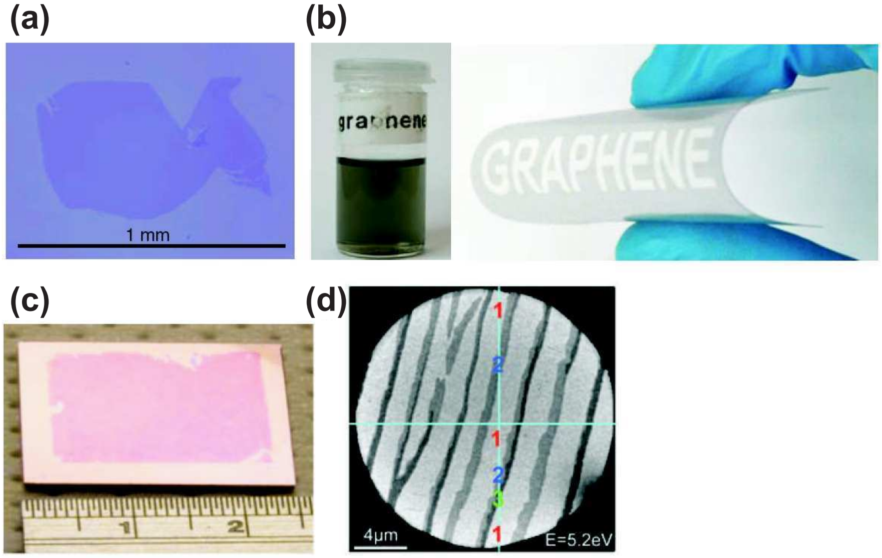

Figure 1.2: (a) Mechanical exfoliated graphene. (b) Suspension of graphene obtained by ultrasonification of graphite and a spray coating in the flexible substrate of the same graphene suspension. (c) Graphene grown in nickel and transferred to silicon oxide substrate. (d) Graphene islands grown in silicon carbide substrate. Adapted from Ref. [12]

Graphene already has given important contributions to nanoscience, presenting many new physical properties and potential applications [5, 12]. However, progress for industrial applications of graphene are still in a very early stage, and the research on this novel material is important to determine its applicability.

1.2 Why study graphene with Raman spectroscopy?

Optical spectroscopies have been applied to the study of condensed matter since the early beginning of materials research. Raman spectroscopy was born in 1928 after C. V. Raman [31], who experimentally verified the apparition of faint lights with different frequencies from the frequency of the incident light on liquids. Since then, Raman spectroscopy has grown with the condensed matter research, and experiments are now relatively simple to be performed.

Raman spectroscopy has historically played an important role in the structural characterization of carbon materials [32, 33]. It has been used in the last decades to characterize graphite, carbon nanotubes, nanographite, amorphous carbon and, more recently, graphene. The Raman spectra for these different kinds of carbon materials are different from each other as shown Fig. 1.3. Although the main Raman bands can be observed in the spectra in every graphitic form, their shape, position and intensity are different. For example the G band around 1600 cm^{-1} in Fig. 1.3 is a single peak for graphene and graphite, but for SWNT the G band is composed by two peaks.

Raman spectroscopy in graphite has been used to probe the degree of disorder, making possible to evaluate crystalline size along the plane and also to measure the degree of stacking order of the graphene layers [34, 35, 36]. In carbon nanotubes, Raman spectroscopy has been intensively used to characterize their diameters, environmental effects, defects and optical transition energies [37]. The first Raman spectroscopy experiments in graphene came in 2006, when it was shown that Raman spectroscopy provides the perfect tool for determining the number of graphene layers (from 1 to 5 layers) [38, 39, 40]. Beyond that, Raman spectra of graphene provided a better knowledge about charge effects in the phonon energies [41, 42, 43, 44] as well as an experimental tool to estimate and monitor doping in graphene [45]. In Fig. 1.4 (a) we show the use of Raman spectroscopy to probe the number of layers and Fig. 1.4 (b) shows how it is possible to monitor the frequency of the Raman band as a function of the charge density in graphene. Moreover, due to the specific electron dispersion of graphene near the Dirac point, the vibrational and electronic structures of graphene systems were probed with the use of resonant Raman spectroscopy [46, 47], providing experimental support for understanding the vibrational and electronic properties of carbon materials.

Raman spectroscopy in graphene still has a wide variety of applications to be discovered. New physical phenomena are constantly being reported, such as electron and phonon properties [49], strain effects [50, 51], doping [52, 53, 54] and magnetic effects [55].

The present work is aimed at gaining a better understanding of electrons, phonons and their interactions in graphene systems by Raman spectroscopy and,

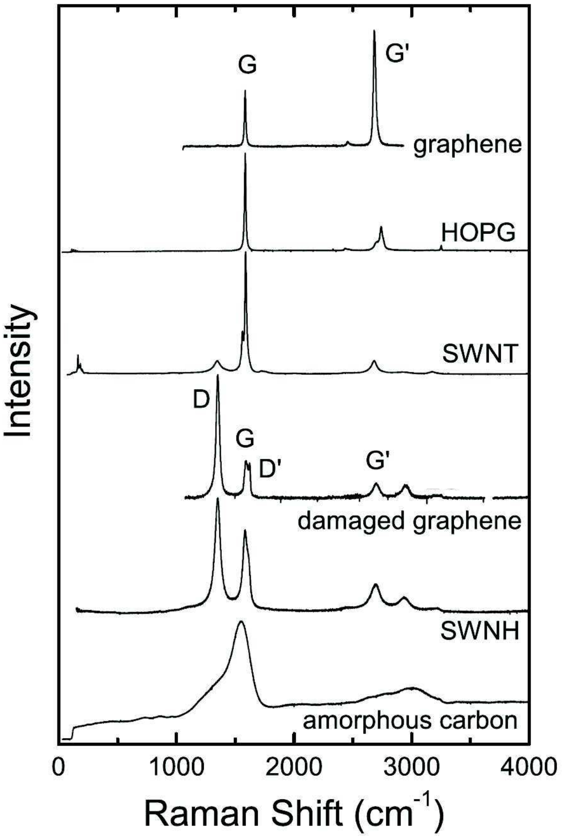

Figure 1.3: Raman spectra for different kinds of carbon systems, from top to bottom: graphene, HOPG, single wall carbon nanotubes (SWNT), damaged graphene, single wall carbon nano horn (SWNH) and amorphous carbon. The name for the main Raman bands are named in the figure, and are discussed along the thesis.

in particular, by resonant Raman spectroscopy.

1.3 Outline

In chapter 2 we review the electronic and vibrational structure of graphene and the interaction between electrons and phonons in this material. In Chapter 3 we first present the basic theory of light interaction in matter and Raman scattering, and then we explain the origin of the main Raman bands in graphene and their selection rules. The determination of the number of layers in few-layer graphene is also discussed in Chapter 3, giving special emphasis to the possibility of using

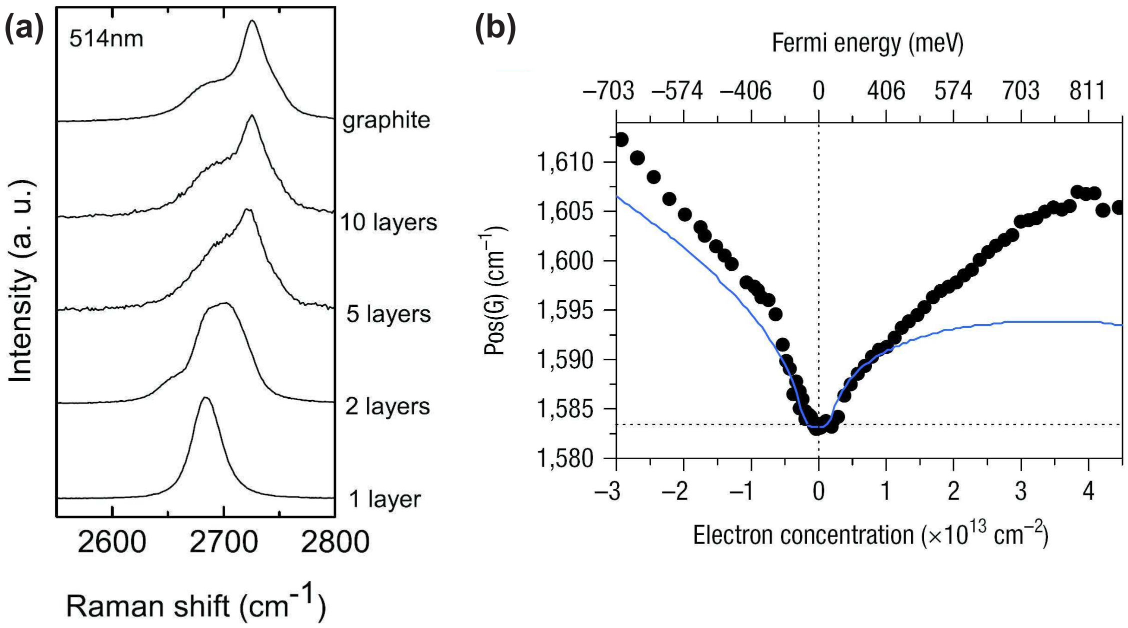

Figure 1.4: (a) Raman spectrum of graphene layers, where it is possible to distinguish the shape of the Raman spectrum as a function of the number of layers [38]. (b) Raman frequency of a monolayer graphene G band as a function of charge concentration in the sample, showing that is possible to correlate the amount of doping with the frequency of the G band of graphene [45]. From Ref. [48]

Raman spectroscopy to distinguish a monolayer from few-layer graphene stacked in the Bernal (AB) configuration. In Chapter 4 we give the experimental details on sample preparation and the Raman instrument used in this work.

In Chapter 5 we derive the symmetry properties for N-layer graphene, where N is an integer, and give the selection rules for optical absorption and for first- and second-order Raman scattering processes. In Chapter 6 we show how the resonant Raman spectroscopy can be used in graphene systems to gather information about its electronic and vibrational properties. In Chapter 7 we make use of Raman spectroscopy to study electron-phonon interactions in bilayer graphene by applying a variable gate voltage between the graphene and the substrate. Finally, in Chapter 8 we draw the conclusions about this PhD thesis.

In Appendix A we discuss the Hamiltonian used to describe the electron-phonon coupling interactions in graphene. Appendix B is devoted to discuss the interaction between light and matter in the electric-dipole approximation. In Appendix C we give the character tables for all points inside the first Brillouin zone of monolayer, N-even and N-odd layers of graphene, which will be helpful in Chapter 5. In Appendix D we show two other experimental results of Raman scattering in graphene obtained during the PhD, which are not yet concluded. In Appendix E we present a resonant Raman study of linear carbon chains inside of single wall carbon nanotubes. We decided to present this work in one appendix, because it deals with a different kind of carbon system.

Chapter 2

Basic concepts of graphene

2.1 The N-layer graphene crystal

Graphene consists of an sp^2 carbon hexagonal network, in which strong covalent bonds are formed between two adjacent carbon atoms. The unit cell for monolayer graphene (1-LG) contains two carbon atoms, A and B, each forming a triangular 2D network, but displaced from each other as shown in Fig. 2.1(a).

The primitive vectors $\mathbf{a_1}$ and $\mathbf{a_2}$ in Fig. 2.1 (a) can be written in terms of the lattice parameter a as [33]:

$$\mathbf{a}_1 = \frac{a}{2}(\sqrt{3}\hat{x} + \hat{y}), \mathbf{a}_2 = \frac{a}{2}(-\sqrt{3}\hat{x} + \hat{y}). \tag{2.1}$$

The value of the lattice parameter is $a = 2.46$ Å, which is considered to be the same as in graphite and is derived from the carbon-carbon distance of 1.42 Å [33]. The direction $\hat{x}$ and $\hat{y}$ are along the vertical and horizontal directions of Fig. 2.1 (a), respectively. The first Brillouin zone in graphene, shown in Fig.2.1(e), is hexagonal and its reciprocal vectors $\mathbf{b_1}$ and $\mathbf{b_2}$ [33] are given by:

$$\mathbf{b}_1 = \frac{2\pi}{a}(\frac{\sqrt{3}}{3}\hat{k}_x + \hat{k}_y), \mathbf{b}_2 = \frac{2\pi}{a}(\frac{-\sqrt{3}}{3}\hat{k}_x + \hat{k}_y). \tag{2.2}$$

The direction $\hat{k}_x$ and $\hat{k}_y$ are shown in Fig. 2.1 (e). The high symmetry points and lines are also shown in Fig.2.1(e). The relative positions of the high symmetry points with respect to the zone center Γ point are given in Table 2.1.

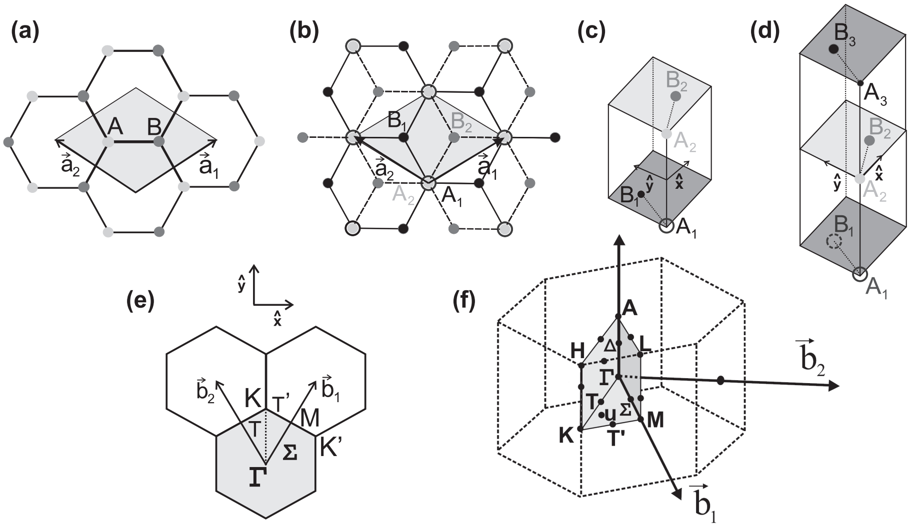

Figure 2.1: (a) The top view of the real space unit cell of monolayer graphene showing the inequivalent atoms A and B and unit vectors $\mathbf{a_1}$ and $\mathbf{a_2}$. (b) The top view of the real space of bilayer graphene. The light/dark gray dots and black circles/dots represent the carbon atoms in the upper and lower layers, respectively, of 2-LG. (c) The unit cell and the $\hat{x}$ and $\hat{y}$ unit vectors of the bilayer and (d) trilayer graphene. (e) The reciprocal space unit cell showing the 1*st* Brillouin zone with its high symmetry points and lines, such as T connecting Γ to K; Σ connecting Γ to M; and T' connecting K to M. The two primitive vectors on the top of the three hexagons shows the real space coordinate axes. (f) The Brillouin zone for 3D graphite, showing the high symmetry points and axes.

The 3D graphite structure corresponds to a stacking of graphene layers in the direction perpendicular to the basal plane (c-axis) in an AB (or Bernal) stacking arrangement, in which the vacant centers of the hexagons in one layer have carbon atoms in hexagonal corner sites of the two adjacent graphene layers, as shown in Fig. 2.1(b). In graphite with AB stacking, the unit cell consists of four carbon atoms A_1, A_2, B_1, and B_2. Normally, the bilayer graphene samples obtained from the mechanical exfoliation of graphite exhibit an AB stacking arrangement, and therefore the unit cell of bilayer graphene (2-LG) has the same number of atoms as that for graphite, with four atoms per unit cell, as shown in Figs. 2.1(b) and 2.1(c). Trilayer graphene (3-LG) in turn contains three layers, two of which are like bilayer graphene and the third layer has atom A_3 over A_1 and atom B_3 over B_1 as shown in Fig. 2.1(d). Four layer graphene (4-LG) consists of the stacking of two unit cells of the type shown in Fig. 2.1(c), one stacked on top of the other.

Table 2.1: The coordinates of the high symmetry points for the first Brillouin zone of graphene

Point	Coordinate
Γ	(0,0,0)
K	$(0,\frac{4\pi}{3a},0)$
K$'$	$(0,-\frac{4\pi}{3a},0)$
M	$(\frac{2\pi}{\sqrt{3}a},0,0)$

The first Brillouin zone of these two-dimensional structures is shown in Fig. 2.1(e). On the other hand, the graphite which has a third direction along the z axis has a three-dimensional Brillouin zone which is shown in Fig. 2.1(f) along with its high symmetry points and lines.

2.2 Band structure of N-layer graphene

2.2.1 Monolayer graphene

In graphene or graphite, the atomic orbitals are in a sp^2 hybridization, in which the carbon atoms are bounded covalently to each other forming a 120° angle. In this kind of hybridization, the π electrons along the z (out of plane) direction are related to many interesting physical phenomena, since they have lower energy compared to the σ orbitals.

The electronic structure of monolayer graphene (1-LG) can be calculated from a variety of ways, from tight binding based approach [33, 56] to ab-initio methods. We can construct the tight binding Hamiltonian following Ref.[56] as:

$$\mathcal{H}_{monolayer} = \begin{pmatrix} 0 & \gamma_0 f(k) \\ \gamma_0 f^*(k) & 0 \end{pmatrix}. \tag{2.3}$$

where $f(k)$ =$\mathrm{e}^{(ik_x \frac{a}{\sqrt{3}})} + 2\mathrm{e}^{(-ik_x \frac{a}{2\sqrt{3}})}\cos(k_y \frac{a}{2})$. The eigen energies are found by diagonalizing this Hamiltonian, and it is important to note that here we ignore the overlap integral matrix S as given in Ref. [33]. The γ_0 parameter is the nearest neighbor transfer integral between the atomic orbitals of the carbon atoms A and B of the graphene sheet.

Figure 2.2 (a) shows the electronic structure of monolayer graphene calculated considering only the first neighbor tight binding parameter γ_0. Monolayer graphene is a zero gap semiconductor, where the valence and conduction bands touch each other at the K (or Dirac) point [56]. For points around the K point, the electronic structure can be described as a linear dispersion (see the right side of Fig. 2.2 (a)), or $E(\mathbf{k}) = \frac{\sqrt{3}}{2}\gamma_0 a\mathbf{k} = \hbar\mathbf{v_F}\mathbf{k}$ [33]. This expression relates directly the electron wave vector $\mathbf{k}$ with the energy by a Fermi velocity v_F, which is found to be close to 10^6 m/s [10] (or γ_0 $\approx$3.0 eV). Fig. 2.2 shows the energy contours around the K point where is possible to clearly observe that, as the energy increases, the circular form tends to be trigonal due to the symmetry of the lattice, and this is called trigonal warping effect. Beyond the tight binding approach, the monolayer band structure can also be evaluated by ab-initio methods which do not depend on the number of neighbors included. Fig.2.2(c) shows the electronic structure of monolayer graphene along the high symmetry lines calculated via density functional theory (DFT) [53].

2.2.2 Bilayer graphene

The bilayer graphene is also a zero gap semiconductor but the electronic dispersion is no longer linear around the K point, but it has a parabolic dependence with $\mathbf{k}$ [56]. Now, the first neighbor tight binding 4x4 Hamiltonian can be written as [33, 56]:

$$\mathcal{H}_{bilayer} = \begin{pmatrix} 0 & \gamma_0 f(k) & \gamma_1 & \gamma_4 f^*(k) \\ \gamma_0 f^*(k) & 0 & \gamma_4 f^*(k) & \gamma_3 f(k) \\ \gamma_1 & \gamma_4 f(k) & 0 & \gamma_0 f^*(k) \\ \gamma_4 f(k) & \gamma_3 f^*(k) & \gamma_0 f(k) & 0 \end{pmatrix}. \tag{2.4}$$

Instead of only one tight binding parameter γ_0, the bilayer has also the γ_1, γ_3 and γ_4 parameters which are interlayer interactions between the nearest neighbors atomic orbitals. Figure 2.3 shows the atomic structure of bilayer graphene, and the nearest neighbors in plane and out-of-plane tight binding parameters.

The calculated band structure of bilayer graphene obtained by diagonalizing $\mathcal{H}_{bilayer}$ is shown Fig. 2.4 (a). Instead of one valence and one conduction bands as in monolayer graphene, the bilayer graphene has two valence and two conduction bands, where two of them touch each other at the K point and the other two are separated by $2\gamma_1$. Also the linear dispersion of monolayer graphene near the K point gives place to a parabolic shape as shown in the right side of Fig.2.4(a). In

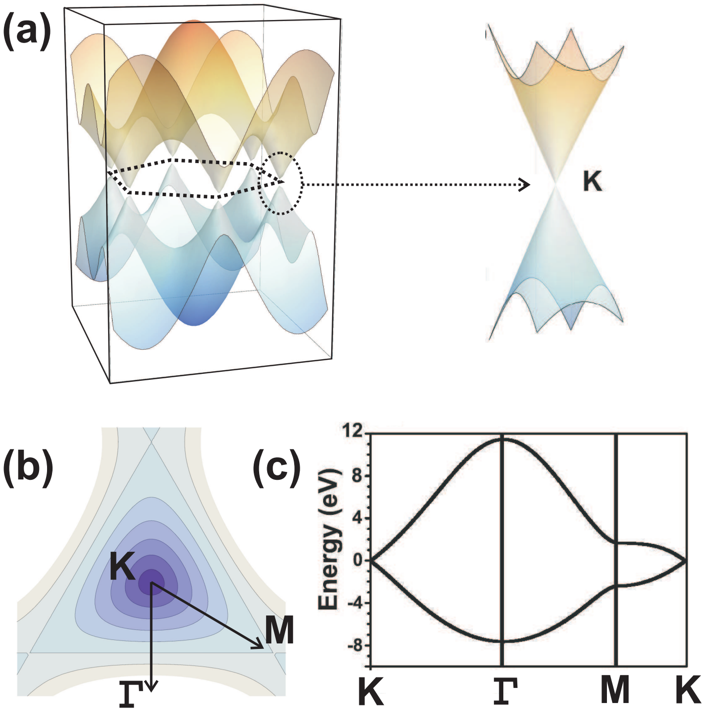

Figure 2.2: (a) The electronic structure of monolayer graphene within the first Brillouin zone and, on the right, a zoom near the K point showing the linear dispersion. (b) Contour plot of the band structure near the K point. (c) Electronic structure of monolayer graphene along the high symmetry lines calculated via DFT [57].

Fig. 2.4(b) the DFT calculation along the high symmetry lines is also shown.

It is important to discriminate the influence of the γ_3 and γ_4 parameters on the band structure of bilayer graphene. The γ_3 parameter gives rise a trigonal warping effect in the low energy spectrum as shown in Fig. 2.5 (a) [21]. This figure shows the contour plot near the K point for energies between 0 and 0.01 eV. It is clear in Fig. 2.5(a) that the equienergies curves are indeed triangles with opposite directions if compared to the crystal symmetry trigonal warping as show in Fig. 2.2(b). The γ_4 parameter is related to the electron-hole asymmetry in bilayer graphene [56]. In Fig. 2.5(b) the blue curve is calculated by setting $\gamma_4 = 0$ and the red curve by $\gamma_4 \neq 0$, and we can see that now the conduction band of the red curve is no longer a mirror image of the valence band.

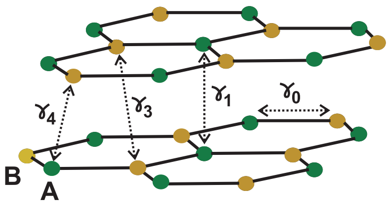

Figure 2.3: Atomic structure of bilayer graphene, where the overlap γ parameters are shown with the respective pair of atoms for each γ_i interaction.

2.2.3 Band structure evolution to graphite

By stacking N graphene layers in the AB stacking arrangement the band structure continues to evolve with increasing number of atoms in the unit cell. Then the electronic bands starts to split into $2N$ components, i.e. trilayer graphene has three conduction and three valence bands and so on. Also the number of tight binding parameters between the neighbor atoms starts to increase with interactions between the first and third layer for example.

For graphite, the electronic structure can be described by the phenomenological Slonczewski-Weiss-McClure (SWM) model [1, 2]. In this model there are the same tight binding parameters as in bilayer graphene with the addition of two terms γ_2 and γ_5 which are the interactions between second-neighbor layers. This model generates the electronic structure of graphite, which happens to be parabolic near the K point along the ΓK plane and linear near H point along the AH plane.

The SWM model can be also used to calculate the electronic spectrum of bilayer graphene, since it has the same number of atoms as in the unit cell and graphite [46]. However, for bilayer the interlayer interaction between the second-neighbor layers is ignored as we will show in Chapter 6.

2.3 Phonon structure of graphene

2.3.1 Phonons including the electron-phonon coupling

An understanding of the phonon dispersion of graphene is essential to interpret their Raman spectra. In this section we show the basic phonon dispersion without including renormalization of some special phonons due to the electron-phonon coupling, which will be discussed after.

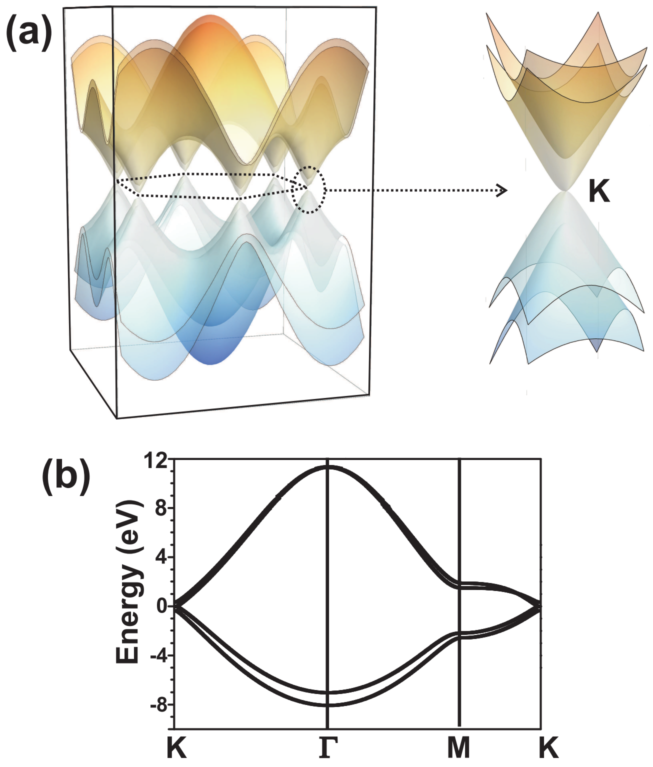

Figure 2.4: (a) The electronic structure of bilayer graphene within the first Brillouin zone and, on the right, a zoom near the K point showing parabolic dispersion. (b) Electronic structure of bilayer graphene along the high symmetry lines calculated via DFT [57].

Since the unit cell of monolayer graphene contains two carbon atoms, A and B, there are six phonon dispersion bands (see Fig. 2.6) [33], in which three are acoustic (A) and the other three are optic (O) phonon modes. For one acoustic (A) and one optic (O) phonon branches, the atomic vibrations are perpendicular to the graphene plane, and they correspond to the out-of-plane (o) phonon modes. For two acoustic and two optic phonon branches, the vibrations are in-plane (i). Traditionally the directions of the vibrations are considered with respect to the direction of the nearest carbon-carbon atoms and, therefore, the phonon modes are classified as longitudinal (L) or transverse (T) according to vibrations parallel or perpendicular, respectively, to the A-B carbon-carbon directions. Therefore, along the high symmetry ΓM and ΓK directions, the six phonon dispersion curves are assigned to LO, iTO, oTO, LA, iTA, and oTA phonon modes (see Fig. 2.6). The density of states (DOS) of the phonon modes is also shown on the right of Fig. 2.6, where it is possible to observe a high DOS near 1370 cm^{-1} [33].

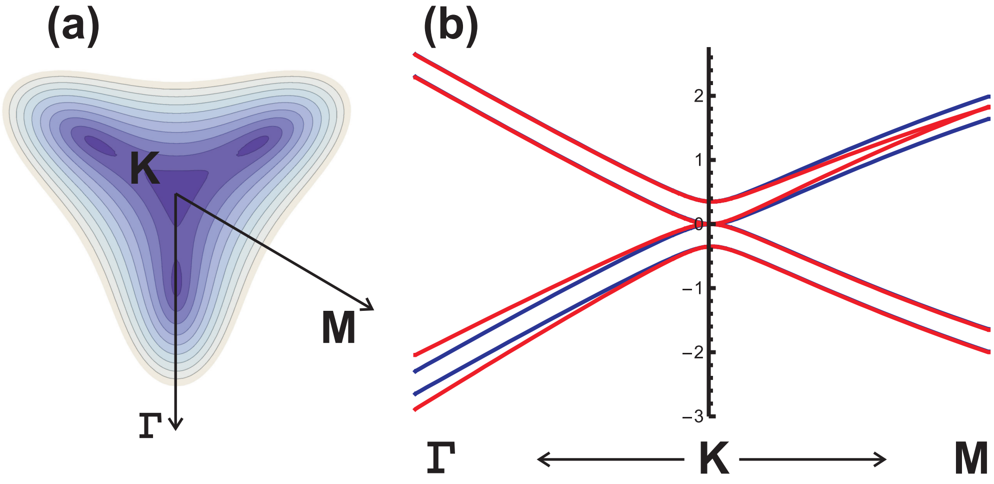

Figure 2.5: (a) Contour plot of the band structure near the K point. (b) Electronic structure of bilayer graphene along the high symmetry lines for $\gamma_4 = 0$ (blue lines) and $\gamma_4 = 0.15$ eV (red lines).

Near the zone center (Γ point), the in-plane iTO and iLO optic modes correspond to the vibrations of the sublattice A against the sublattice B as shown in Fig. 2.7, and these modes are degenerate at the Γ point. According to group theory, the degenerate zone-center iLO and iTO phonon modes belong to the two-dimensional E_{2g} representation and, therefore, they are Raman active modes.[60, 33] The degeneracy of the iLO and iTO phonons disappears for general points inside the first Brillouin zone (BZ) of graphene. The phonon modes around the K point are especially important, since the D-band and G'-band are related to phonon modes in the vicinity of the K point as will be discussed later. Exactly at the K-point, the phonon which comes from the iTO branch is non degenerate and belongs to the A_1' irreducible representation of the point group D_{3h}, and the eigenvector of this mode is represented in Fig. 2.7. The iLO and iLA phonon branches meet each other at the K point giving rise to a double degenerate phonon, with E' symmetry [61, 59]. The phonon modes for N-layer graphene derived by group theory will be discussed in more detail in Chapter 5.

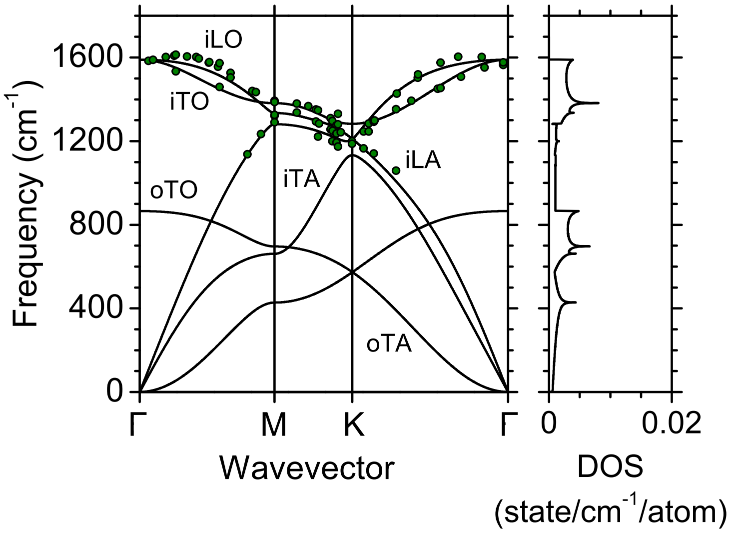

Figure 2.6: Calculated phonon dispersion relation of graphene. [58] LO, iTO, oTO, LA, iTA and oTO are phonon modes at the Γ point. The green circles are X-ray scattering measurements from Ref. [59]. On the right the DOS of the phonons.

2.4 Phonons corrected by the electron-phonon coupling

2.4.1 The electron-phonon interaction and Kohn anomaly

In a first approximation the lattice vibrations are determined by the vibration of the ions with respect to its equilibrium position. In the particular case of graphene, one should include the electronic cloud which should also affect the movement of the ions. When the local density of electrons is increased, an extra kinetic energy should appear due to exclusion principle, and thus the electronic cloud screens the atomic vibrations [62]. The effect of mutual interaction between the electronic cloud and the atomic motion is called electron-phonon interaction.

The electron-phonon interaction affects the phonon spectrum and, to calculate this change we shall use pertubation theory for the electron-phonon Hamiltonian $\mathcal{H}_{e-p}$ (see Appendix A) [62]. Then we have:

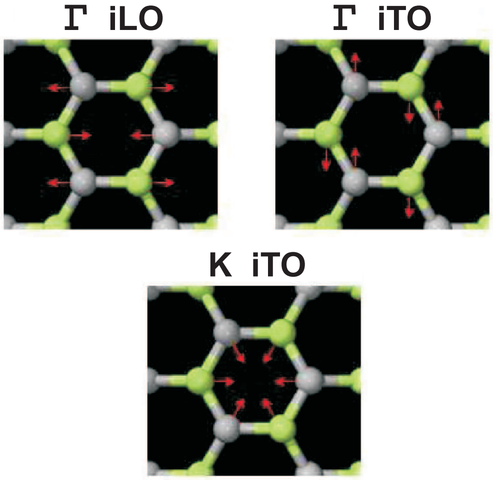

Figure 2.7: Eigenvectors for three phonon modes at Γ and K point in graphene.

$$\varepsilon = \varepsilon_0 + \langle \Phi_{\mathbf{k}} | \mathcal{H}_{e-p} | \Phi_{\mathbf{k}} \rangle + \langle \Phi_{\mathbf{k}'} | \frac{\mathcal{H}_{e-p}\mathcal{H}_{e-p}}{\varepsilon_0 - \varepsilon_1} | \Phi_{\mathbf{k}} \rangle + \mathcal{O}^3, \tag{2.5}$$

where ε_0 and ε_1 are the unperturbed and perturbed energies of the state $\Phi_{\mathbf{k}}$ which has $n_{\mathbf{q}}$ phonons in the mode $\mathbf{q}$ and $n_{\mathbf{k}}$ electrons in the state $\mathbf{k}$. Then the state is written as $\Phi_{\mathbf{k}} = |n_{\mathbf{q}}, n_{\mathbf{k}}\rangle$. The first-order therm vanishes because $\mathcal{H}_{e-p}$ either creates or destroys a phonon and the resulting wavefunction is orthogonal to $\Phi_{\mathbf{k}}$. The second-order contribution can be written as (see Appendix A):

$$\varepsilon_2 = \langle \Phi_{\mathbf{k}'} | \sum_{k,k'} |M_{kk'}|^2 \left[\frac{a^\dagger_{-\mathbf{q}} c^\dagger_{\mathbf{k}} c_{\mathbf{k}'} a_{-\mathbf{q}} c^\dagger_{\mathbf{k}'} c_{\mathbf{k}}}{\varepsilon_0 - \varepsilon_1} + \frac{a_{\mathbf{q}} c^\dagger_{\mathbf{k}} c_{\mathbf{k}'} a^\dagger_{\mathbf{q}} c^\dagger_{\mathbf{k}'} c_{\mathbf{k}}}{\varepsilon_0 - \varepsilon_1} \right] | \Phi_{\mathbf{k}} \rangle, \tag{2.6}$$

where $a^\dagger_{\mathbf{q}}$ ($a_{\mathbf{q}}$) creates (destroys) a phonon at the state $\mathbf{q}$, $c^\dagger_{\mathbf{q}}$ ($c_{\mathbf{q}}$) creates (destroys) an electron in the state $\mathbf{k}$, and $M_{kk'}$ are the electron-phonon matrix elements. The first therm in the brackets represents an electron being scattered from $\mathbf{k}$ to $\mathbf{k}'$ by absorbing a phonon with wavenumber $\mathbf{q} = \mathbf{k} - \mathbf{k}'$. The first denominator $(\varepsilon_0 - \varepsilon_1)$ can be written as the energy difference between the initial and intermediated states, thus it can written as $(\varepsilon_{\mathbf{k}} + \hbar\omega_{-\mathbf{q}} - \varepsilon_{\mathbf{k}'})$. In the final state the electron is scattered back with the emission of a phonon. Similarly the denominator of the second term in the brackets can be written as $(\varepsilon_{\mathbf{k}} - \hbar\omega_{-\mathbf{q}} - \varepsilon_{\mathbf{k}'})$. Equation 2.6 can be written

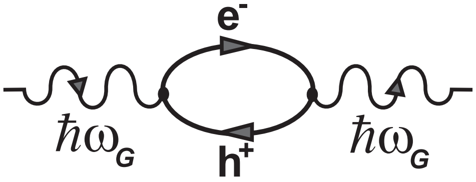

Figure 2.8: Feynman diagram for the second-order process that re-normalizes the phonon energy. The first node shows the decay of a phonon into an electron-hole pair, and the second node shows the recombination of the electron hole and the emission of a phonon.

(see Appendix A) in terms of occupation numbers for electrons ($\langle n_{\mathbf{k}} \rangle$) and phonons ($\langle n_{\mathbf{q}} \rangle$), and we find that the corrected phonon energy $\hbar\omega_{\mathbf{q}}^{(p)}$ is [62]:

$$\hbar\omega_{\mathbf{q}}^{(p)} = \hbar\omega_{\mathbf{q}} + \sum_{\mathbf{k}} |M_{\mathbf{k}\mathbf{k}'}|^2 \frac{2\langle n_{\mathbf{k}} \rangle (\varepsilon_{\mathbf{k}} - \varepsilon_{\mathbf{k}'})}{(\varepsilon_{\mathbf{k}} - \varepsilon_{\mathbf{k}'})^2 - (\hbar\omega_{\mathbf{q}})^2}. \tag{2.7}$$

This equation relates the phonon frequency change due to electron-phonon interaction. Fig. 2.8 shows the diagram related to Eq. 2.7 in which an electron in the valence band is first excited to the conduction band by absorbing a phonon, thus creating an electron-hole pair. The diagram shown in Fig. 2.8 is valid for the first term of Eq. 2.6. The electron and hole then recombine, thus emitting a phonon. Both the frequency and lifetime of the phonon are significantly affected by this second-order process [42, 63, 64].

Now let's assume that the electronic energy is much larger than the phonon frequency then we have that:

$$\hbar\omega_{\mathbf{q}}^{(p)} = \hbar\omega_{\mathbf{q}} - \sum_{\mathbf{k}} |M_{\mathbf{k}\mathbf{k}'}|^2 \frac{2\langle n_{\mathbf{k}} \rangle}{(\varepsilon_{\mathbf{k}'} - \varepsilon_{\mathbf{k}})}. \tag{2.8}$$

This less generic equation is useful to see the consequence when we take its derivative with respect to $\mathbf{q}$ (assuming a one-direction derivative for clarity) [62]:

$$\frac{\hbar\partial\omega_{\mathbf{q}}^{(p)}}{\partial q_x} = \hbar\frac{\partial\omega_{\mathbf{q}}}{\partial q_x} - \sum_{\mathbf{k}} |M_{\mathbf{k}\mathbf{k}'}|^2 \frac{2\langle n_{\mathbf{k}} \rangle}{(\varepsilon_{\mathbf{k}-\mathbf{q_x}} - \varepsilon_{\mathbf{k}})^2} \frac{\partial\varepsilon(k - q_x)}{\partial q_x}. \tag{2.9}$$

An interesting behavior occurs when $q = 2k_F$, where k_F is the radius of the Fermi surface. The states $k' = k - q$ and k are connected by q in the same Fermi surface. Then, the summation in Eq. 2.9 contain divergent factors because $\varepsilon_{\mathbf{k}-\mathbf{q_x}}$ will be equal to $\varepsilon_{\mathbf{k}}$ when q connects states in the same Fermi surface. This divergency is the so-called Kohn anomaly [65] which appears as a kink in the phonon spectrum whenever $q = 2k_F$. Or, more generally, the Kohn anomaly occurs when $\mathbf{q} = \mathbf{k_1} - \mathbf{k_2} + \mathbf{b}$ where $\mathbf{k_1}$ and $\mathbf{k_2}$ are electron state at the Fermi surface and $\mathbf{b}$ is a reciprocal lattice vector, necessary to bring the phonon wavevector $\mathbf{q}$ back into the 1st Brillouin zone [65].

In the case of graphene the Fermi surface corresponds to the K and K′ points, and then the Fermi wavevectors $\mathbf{k_1}$ and $\mathbf{k_2}$ are at the corners of the 1st Brillouin zone (namely the $\mathbf{K}$ and $\mathbf{K}'$ vectors) and, as first reported by Piscanec *et al.* [66], the Kohn anomaly occurs for special phonons at the Γ and K points of graphene. In particular, it was shown in this work [66] that the slopes of the phonon dispersion at these special points are proportional to the electron-phonon coupling parameter λ_{e-p}.

Figure 2.9 shows the calculation performed by Piscanec *et al.* [66] where its is possible to observe the divergent characteristic of the Kohn anommaly near the Γ point for the iLO mode and at K point for the iTO mode.

2.4.2 Non-adiabatic effects of the phonon frequency

2.4.2.1 Monolayer graphene

The adiabatic approximation is one of the most useful methods to facilitate quantum mechanical calculations of solids or molecules. One of the most important features of this approximation (first introduced by Born and Oppenheimer), is the separation of variables between the electronic and nuclear variables [67]. With this approximation we are led to the adiabatic criterion [67]:

$$\hbar\omega_q \ll |\varepsilon_k - \varepsilon_{k'}|, \tag{2.10}$$

and this condition is well satisfied for some semiconductors and insulators. However, for metallic systems the adiabatic criterion is broken as we have $\hbar\omega_q \sim |\varepsilon_k - \varepsilon_{k'}|$ [67]. In the previous section, from equation 2.7 to 2.8 we assumed that the phonon energy is much smaller than the electronic energy, which is not valid

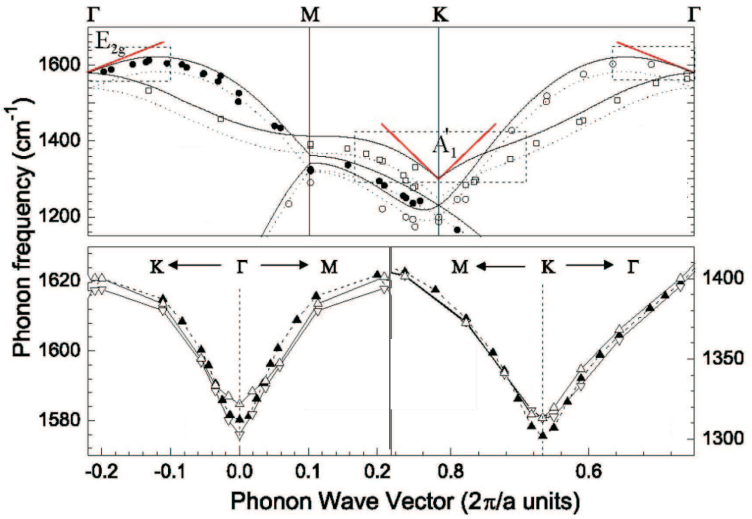

Figure 2.9: Phonon dispersion of graphene from Ref. [66] showing the Kohn anomaly at the Γ and K points. The lines of the top part of the figure is the theoretical calculated curve and the symbols are experimental data. The both bottom figures are a closeup of the phonon dispersion near the Γ and K points. The different lines shows different parameters for the theoretical calculation done in Ref [66].

for metals and graphene. Now we should study the dependence of the phonon frequency as a function of the Fermi energy in the framework of non-adiabatic second order pertubation theory of the Fröhlich Hamiltonian. We can rewrite Eq. 2.7 in terms of the Fermi-Dirac distribution instead of the electron occupation number, i.e.,

$$\hbar\omega_{\mathbf{q}}^{(p)} = \hbar\omega_{\mathbf{q}} + \int kdk|M_{\mathbf{k}\mathbf{k}'}|^2 \frac{2(\varepsilon_{\mathbf{k}} - \varepsilon_{\mathbf{k}'})}{(\varepsilon_{\mathbf{k}} - \varepsilon_{\mathbf{k}'})^2 - (\hbar\omega_{\mathbf{q}} + i\delta)^2} \times \left(\frac{1}{e^{\frac{\varepsilon_{\mathbf{k}'} - E_F}{K_B T}} + 1} - \frac{1}{e^{\frac{\varepsilon_{\mathbf{k}} - E_F}{K_B T}} + 1} \right), \tag{2.11}$$

where we have substituted the discrete sum for the integral sum in k, which should be evaluated from zero to a cutoff value. We have also included a small imaginary part (δ) in the denominator in order to avoid the singular behavior of the function. The energy of the phonon can be evaluated as Re[$\hbar\omega_{\mathbf{q}}^{(p)}$] and its lifetime by -Im[$\hbar\omega_{\mathbf{q}}^{(p)}$] [63]. The results of our calculation are shown in Fig. 2.11.

For monolayer graphene we assume the linear electronic dispersion ($E(k) = v_F k$), and than we calculate the frequency shift for the phonon at $q = 0$ in units of the electron-phonon coupling as a function of the Fermi energy (E_F)(See Fig. 2.11 (a)). The phonon frequency has a logaritimic divergence at $\omega_q/2$. The renormalization of the phonon energy is strongly dependent on the Fermi level position, which can be tuned by doping graphene with electrons or holes. In fact, if one changes the Fermi energy of the system, there is a reduction in the interaction between phonons and interband electron-hole pairs, thus changing the effective force constant of the lattice vibrations. This renormalization, which is very effective when $|E_F| < \hbar\omega_0/2$, is inhibited when the change in the Fermi level is larger than half of the phonon energy, as shown in Fig. 2.11. This is explained by the fact that the Pauli exclusion principle in this case suppresses the process depicted in Fig 2.8 (creation of an electron-hole pair by exciting a phonon). The suppression of the renormalization due to the electron-phonon interaction can be seen also in the lifetime of the phonon which is large when $|E_F| < \hbar\omega_0/2$ (see Fig. 2.11 (b)). The temperature also strongly affects the anomaly in $\hbar\omega_0/2$, which is smoothed as can be seen in the frequency and lifetime calculation shown Fig. 2.11 for three different temperatures.

Theoretical models for the phonon self-energy [42, 63, 64] and time dependent second order pertubation theory have predicted the same logarithmic dependence for the phonon softening on the chemical potential (or Fermi level change) for graphene. This anomalous phonon behavior has been experimentally observed by Raman spectroscopy of doped graphene [43, 44, 45], as shown in Fig. 1.4 (b).

2.4.2.2 Bilayer graphene

In the case of bilayer graphene, the phonon mode at $q = 0$ splits into two components, associated with the symmetric (S) and anti-symmetric (AS) displacements of the atoms in the two layers. Moreover, due to the splitting of the π and π^* bands in this material, phonons can couple with electron-hole pairs produced by interband or intraband transitions. Interbands transitions are those were the hole is in the valence band and the electron in the conduction band. The intraband transitions occur when both the electron and the hole are in the conduction or in the valence band. T. Ando [68] recently calculated the dependence of the self-energy of the S and AS phonons as a function of Fermi energy and predicted the hardening and softening of the S and AS phonons, respectively, induced by electron or hole doping.

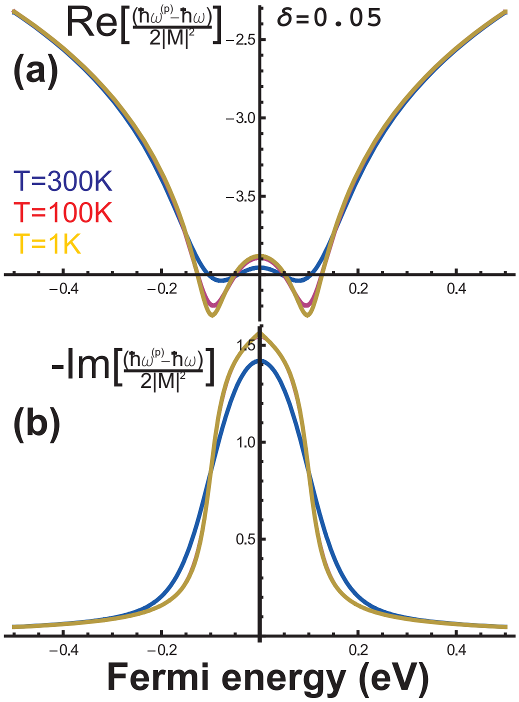

Figure 2.10: (a) Frequency and (b) lifetime of the phonon as a function of the Fermi energy for three different temperatures calculated from Eq. 2.11.

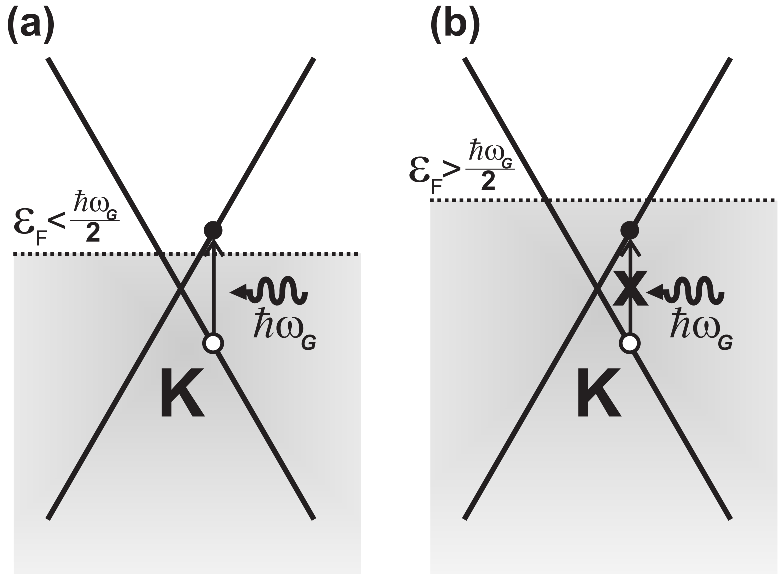

Figure 2.11: The renormalization of the phonon energy associated with the mechanism shown in Fig. 2.8 is allowed when the change in the Fermi energy $\Delta\varepsilon_F$ is smaller than half of the phonon energy $\hbar\omega_G/2$ (upper figure) and it is suppressed for $\Delta\varepsilon_F > \hbar\omega_G/2$ (lower figure).

In order to discuss the phonon renormalization effect in bilayer graphene, we must consider the selection rules for the interaction of the symmetric and antisymmetric phonons with the interband or intraband electron-hole pairs. The band structure of bilayer graphene near the K point shown in Figure 2.12 consists of four parabolic bands, two of them touching each other at the K point, while the other two bands are separated by $2\gamma_1$, where $\gamma_1 \sim 0.35$ eV.

The electron-phonon interaction in bilayer graphene is described by a 2x2 matrix for each phonon symmetry, where each matrix element gives the contribution of electron-hole pairs involving different electronic sub-bands [68]. For the symmetric phonon mode, all matrix elements are different from zero, and this phonon can interact with both interband or intraband electron-hole pairs, as shown in Figure 2.12(a), giving rise to the phonon energy renormalization. However, for the antisymmetric phonon mode, the diagonal terms of the matrix are null, showing that there is no coupling between the AS phonons and interband electron-hole pairs. Therefore, no Kohn anomaly is expected for the antisymmetric phonon mode when the Fermi level is at the Dirac point.

However, if the Fermi energy is moved either up or down with respect to the

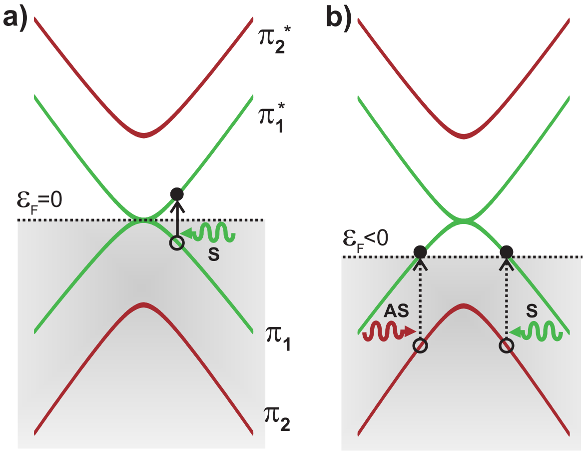

Figure 2.12: Parabolic band structure of bilayer graphene near the K point. The vertical arrows illustrate the possible transitions induced by symmetric (green) and antisymmetric (red) $\mathbf{q}$=0 phonons for (a) interband electron-hole pairs creation at (ε_F=0) and (b) intraband electron-hole pairs creation (ε_F <0). The opening of an energy gap around the Dirac point is not considered in this diagram.

Dirac point, [for instance, $\varepsilon_F < 0$ as shown in Fig. 2.12(b)], the intraband electron-hole pairs can be produced by phonons. In this case, the anti-symmetric phonons also have their energies renormalized, giving rise to the Kohn anomaly. Notice that, since the energy separation between the π_1 and π_2 bands ($\gamma_1 \sim 0.35$ eV) is larger than the G band energy (~ 0.2 eV), the electron-hole pair creation process by those phonons is a virtual process. Therefore, we expect the dependence of the shift of the anti-symmetric mode with Fermi energy to be smoother than that of the symmetric mode. A similar result has been recently observed in gated semiconducting carbon nanotubes [69] which had a band gap larger than the phonon energy.

Figure 2.13 shows the calculation performed by T. Ando [68] for the frequency (solid lines) and broadening (dashed lines) of the S and AS modes as a function of the Fermi energy. The behavior of the S mode is almost the same as that of monolayer graphene, where we have logarithmic singularity when $\varepsilon_F = \hbar\omega/2$, and a hardening for this phonon mode for higher ε_F changes. For the AS mode we have a frequency softening by changing the Fermi energy, and there is no logarithmic singularity. It is also possible to observe that the logarithmic singularity and the broadening is affected by the value of δ of Eq. 2.11, which is related to charge inhomogeneity present in the sample.

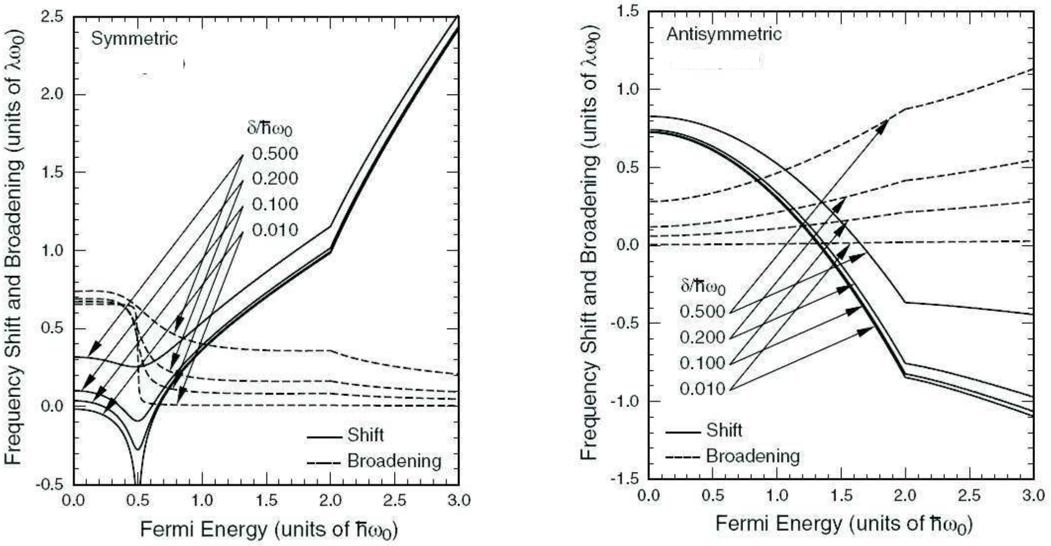

Figure 2.13: Calculated frequency shift (closed lines) and broadening (dashed lines) for the symmetric mode (left panel) and anti-symmetric mode (right panel) of bilayer graphene as a function of the Fermi energy for different values of δ. Adapted from Ref. [68]

In Chapter 7 we will present our experimental results which confirm the calculations done by T. Ando [68].

Chapter 3

Basic concepts of Raman scattering

3.1 Theory of Raman scattering

3.1.1 Light-matter interaction

The interaction of light and matter is of great interest due its contribution to many physical phenomena, such as light scattering (Raman and Rayleigh), absorption and luminescence. We begin the calculation of light absorption of an electron (with charge $-e$) on a generic crystal with the Shrödinger equation given by [70]:

$$[(\frac{(\hat{\mathbf{p}}+e\mathbf{A})^2}{2m})+V_{crystal}]\Phi(\mathbf{r},t)=i\hbar\frac{\partial\Phi(\mathbf{r},t)}{\partial t}, \tag{3.1}$$

where $\mathbf{A}$ is the vector potential and $V_{crystal}$ is the potential of the crystal under study. By expanding the quadratic term we have:

$$[\frac{\hat{\mathbf{p}}^2}{2m}+V_{crystal}]\Phi(\mathbf{r},t)+\frac{[e\hat{\mathbf{p}}\cdot\mathbf{A}+e\mathbf{A}\cdot\hat{\mathbf{p}}+e\mathbf{A}^2]}{2m}\Phi(\mathbf{r},t)=i\hbar\frac{\partial\Phi(\mathbf{r},t)}{\partial t}. \tag{3.2}$$

The second term of the above equation can be treated as a time dependent perturbation (H_I) on the electronic levels described by the first term. In a first approximation, we can neglect the quadratic term $\mathbf{A^2}$ when we are using ordinary light sources [70, 71]. The operator $\hat{\mathbf{p}} \cdot \mathbf{A}$ acting on a wavefunction Φ in Eq. 3.2 can be written as [70]:

$$\hat{\mathbf{p}} \cdot \mathbf{A}\Phi = -i\hbar\nabla \cdot (\mathbf{A}\Phi) = -i\hbar[(\nabla \cdot \mathbf{A})\Phi + \mathbf{A} \cdot (\nabla\Phi)]. \tag{3.3}$$

By using the Coulomb gauge we have that $\nabla \cdot \mathbf{A} = \mathbf{0}$, then we are left with $H_I = (e/m)\mathbf{A} \cdot \hat{\mathbf{p}}$. The second approximation is to note that the magnetic field contribution for the interaction of electrons with the electromagnetic wave is much smaller than that for the electric field [70]. With this simplification we can write the vector potential $\mathbf{A}$ in terms of the electric field by noting that in the Coulomb gauge we have the relation $\mathbf{E} = -\frac{\partial \mathbf{A}}{\partial \mathbf{t}}$. Then by writing the electric field as $\mathbf{E}(\mathbf{r}, \mathbf{t}) = \mathbf{2E_0} \cos(\mathbf{k_L} \cdot \mathbf{r} - \omega \mathbf{t})\hat{\mathbf{e}}$, where $\mathbf{k_L}$ is the wavevector of the electromagnetic wave and $\hat{\mathbf{e}}$ is the polarization vector of the light, we are left with the light-matter perturbation written as [70]:

$$H_I = \frac{eE_0}{im\omega}[e^{i(\mathbf{k_L}\cdot\mathbf{r}-\omega t)} - e^{-i(\mathbf{k_L}\cdot\mathbf{r}-\omega t)}](\hat{\mathbf{e}} \cdot \hat{\mathbf{p}}). \tag{3.4}$$

The first term of the above equation gives rise to the electron absorption of a photon with energy $\hbar\omega$ and momentum $\hbar\mathbf{k_L}$, and the other term, to the emission of a photon due to the electron decay [70].

The Hamiltonian described by Eq. 3.4 when bracketed with initial and final electronic states with $\mathbf{k_{i,e}}$ and $\mathbf{k_{f,e}}$ wavevectors, lead to the momentum selection rule:

$$\mathbf{k_{i,e}} + \mathbf{k_L} = \mathbf{k_{f,e}}. \tag{3.5}$$

By quantifying the values of $\mathbf{k_L}$ in terms of $\mathbf{k_{i,e}}$ and $\mathbf{k_{f,e}}$ in the first Brillouin zone, we can make the approximation that $\mathbf{k_L} \ll \mathbf{k_{i,e}}; \mathbf{k_{f,e}}$. Therefore the selection rule for light absorption with wavevectors much smaller than the Brillouin zone of a crystal is: $\mathbf{k_{i,e}} \simeq \mathbf{k_{f,e}}$ (Appendix B).

With this last approximation, we are led to the electric-dipole approximation, where we expand the exponential terms in Eq. 3.4 ($e^{(i\mathbf{k_L}\cdot\mathbf{r})} = 1 + i\mathbf{k_L} \cdot \mathbf{r} + ...$)

and keep only the first term. Now by using time-dependent perturbation theory [71, 72] for H_I we are left with absorption transition rate from the state i to j (Fermi golden rule)[70, 72]:

$$W_{ji} = \frac{2\pi}{\hbar}(\frac{eE_0}{m\omega})^2 \left| \frac{\langle i|\hat{\mathbf{e}} \cdot \hat{\mathbf{p}}|j\rangle}{E_j - E_i - \hbar\omega} \right|^2 . \tag{3.6}$$

This equation gives the probability of an electron with initial state i with energy E_i to absorb a photon with energy $\hbar\omega$ going to a final state j with energy E_j. We should note that when we are in the case of resonant exitation ($E_j - E_i = \hbar\omega$), we rewrite Eq. 3.6 as [72]:

$$W_{ji} = \frac{2\pi}{\hbar}(\frac{eE_0}{m\omega})^2 |\langle i|\hat{\mathbf{e}} \cdot \hat{\mathbf{p}}|j\rangle|^2 \delta(E_j - E_i - \hbar\omega). \tag{3.7}$$

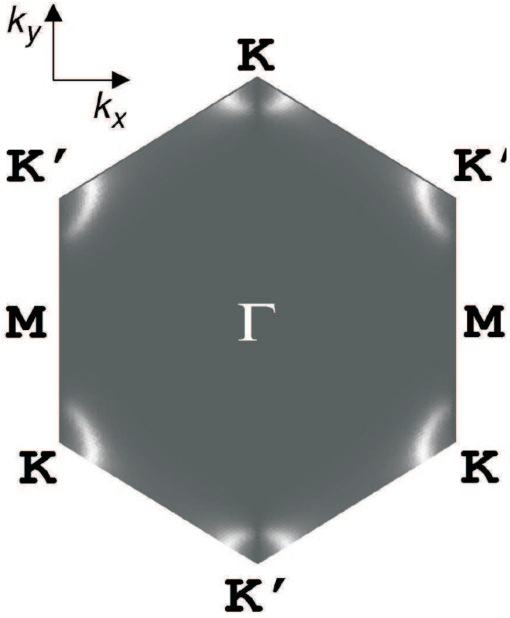

Figure 3.1: The calculated optical absorption intensity of graphene with light polarization along k_y direction, where it is possible to observe that the absorption is zero for the vertical lines connecting K and K′ points. From Ref. [73]

The calculation of the optical absorption can be done following Eq. 3.7, noting that the initial ($|i\rangle$) and final ($|j\rangle$) states involve the electronic wavefunctions for graphene. This calculation was done by Grüneis *et al.* [73], and it has been show that, due to the special linear dispersion of graphene, there is a node along the ΓK line when the incident light has polarization along the y direction. Figure 3.1 shows a plot of the optical absorption intensity in the first Brillouin zone where the the light polarization is along the k_y direction in this figure. It is possible to observe an absorption node along the ΓK line in the k_y direction. This effect has been experimentally observed by Cançado *et al.* in graphite edges [74] and graphene nanoribbons [75]. We will discuss later in Chapter 5 the application of Eq. 3.7 together with group theory in graphene, which gives the same result obtained by Grüneis *et al.*. Also, this optical absorption node will be used in Chapter 5 to describe second-order Raman bands within a group theory approach.

3.1.2 Macroscopical approach to the Raman scattering and selection rules

The macroscopical approach to explain the Raman scattering is based on the action of an incident light on a extended medium creating a macroscopic polarization vector [76]. To begin, consider an infinite medium with dielectric susceptibility χ, which is a tensor. The induced electric dipole can be written in terms of electric field $\mathbf{E}$ of the incident light on the medium as:

$$\mathbf{P} = \chi \cdot \mathbf{E}, \tag{3.8}$$

where the electric field is written as a plane wave:

$$\mathbf{E} = \mathbf{E_0} cos(\mathbf{k} \cdot \mathbf{r} - \omega t). \tag{3.9}$$

Here $\mathbf{k}$ and ω are the wavevector and the frequency of the incident light.

The polarizability tensor χ should also depend on the atomic vibrations of the medium, because the atomic positions are changing in time. To describe the changes in χ due to the atomic motion we consider that the amplitudes of the atomic vibrations in room temperature are much smaller than the lattice constant of the medium, and then the matrix elements of χ can be expanded as a function of the generalized coordinate of a given vibrational mode Q_l in Taylor series as [76]:

$$\chi_{ij} = (\chi_{ij})_0 + \sum_l \left(\frac{\partial \chi_{ij}}{\partial Q_l}\right)_0 Q_l + \mathcal{O}^{(2)}, \tag{3.10}$$

where $(\chi_{ij})_0$ is the value of χ_{ij} in the equilibrium configuration. To first order, we can rewrite Eq. 3.8 as:

$$\mathbf{P} = \mathbf{P_{rayleigh}} + \mathbf{P_{raman}}, \tag{3.11}$$

where the $\mathbf{P_{rayleigh}}$ is the polarization vector oscillating with same frequency as that of the incident radiation, and $\mathbf{P_{raman}}$ is the modified polarization due to the vibration of the atoms. Combining Eqs. 3.8, 3.9 and 3.10, we have the Raman contribution to the induced polarization given by:

$$P_{raman,i} = \sum_{i,j} \left(\frac{\partial \chi_{ij}}{\partial Q_l}\right)_0 Q_l E_{0,j} \cos(\mathbf{k} \cdot \mathbf{r} - \omega t). \tag{3.12}$$

In order to determine the frequency and wavevector of $\mathbf{P_{raman}}$ we describe Q_l as a plane wave with wavevector $\mathbf{q}$ and frequency ω_0 as:

$$Q_l = Q_l^0 cos(\mathbf{q} \cdot \mathbf{r} - \omega_0 t) \cdot \hat{e}. \tag{3.13}$$

Inserting the above equation into Eq. 6.2, and using the trigonometrical relation of cosines, we find [76]:

$$P_{raman,i} = \frac{1}{2} \sum_{i,j} \left(\frac{\partial \chi_{ij}}{\partial Q_l}\right)_0 Q_l^0 E_{0,j} \times \{\cos[(\mathbf{k}+\mathbf{q})\cdot\mathbf{r}-(\omega+\omega_0)t] + \cos[(\mathbf{k}-\mathbf{q})\cdot\mathbf{r}-(\omega-\omega_0)t]\}. \tag{3.14}$$

This final result shows that the modified polarization has two components, the first (second) with higher (lower) frequency with respect to the incident light. We call the Stokes component of the Raman scattering the scattered wave with wavevector $\mathbf{k_S} = (\mathbf{k} - \mathbf{q})$ and frequency $\omega_S = \omega - \omega_0$, and the Anti-Stokes component which has the wavevector described by $\mathbf{k_{AS}} = (\mathbf{k} + \mathbf{q})$ and frequency $\omega_{AS} = \omega + \omega_0$.

Figure 3.2 illustrates a Raman spectrum in which an incident light with frequency ω creates Stokes and anti-Stokes components with frequency given by $\omega - \omega_0$ and $\omega_i + \omega_0$ respectively. Inserting Eq. 3.14 into Eq. 3.11, it is possible to observe that an incident light with frequency ω will generate scattered light with frequencies ω (Rayleigh) and $\omega \pm \omega_0$ (Raman), which is illustrated in Fig. 3.3.

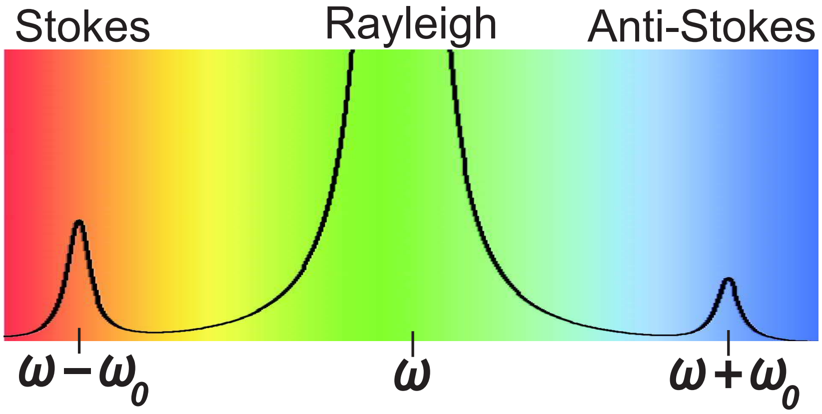

Figure 3.2: Schematics of the Raman spectrum where an incident light with frequency ω generates an elastically scattered light (Rayleigh) and two inelastically scattered components with frequency $\omega_i - \omega_0$ (Stokes) and $\omega_i + \omega_0$ (anti-Stokes).

Notice that due to the conservation of momentum for Stokes or anti-Stokes scattering we should analyze the magnitude for both incident and phonon wavevectors that contributes to the Raman scattering. Typically, light with wavelength in the visible range (500 nm) has a wavevector in the order of 10^7 m^{-1}, which will create a maximum phonon wavevector with this order of magnitude. If we compare the magnitude of q with the dimensions of the first Brillouin zone which, typically, is in the order of 10^{10} m^{-1}, we can see that visible light only probes phonons with small wavevectors, and first order Raman is limited to analyze zone-center phonons ($q \sim 0$) [76].

To find the Raman selection rule, we note that polarizability derivative $\frac{\partial \chi_{ij}}{\partial Q_k}$ in Eq. 3.14 is a second rank symmetric tensor [76, 77]. Then a phonon belonging to an specific irreducible representation is Raman active if it transforms as quadratic basis functions (e.g. x^2, y^2, z^2, xy, xz and yz), which are found in character tables in group theory text books [77].

We can also write down second order terms in the expansion of Eq. 3.10, to see that it is possible to observe phonons not only in the center of the first

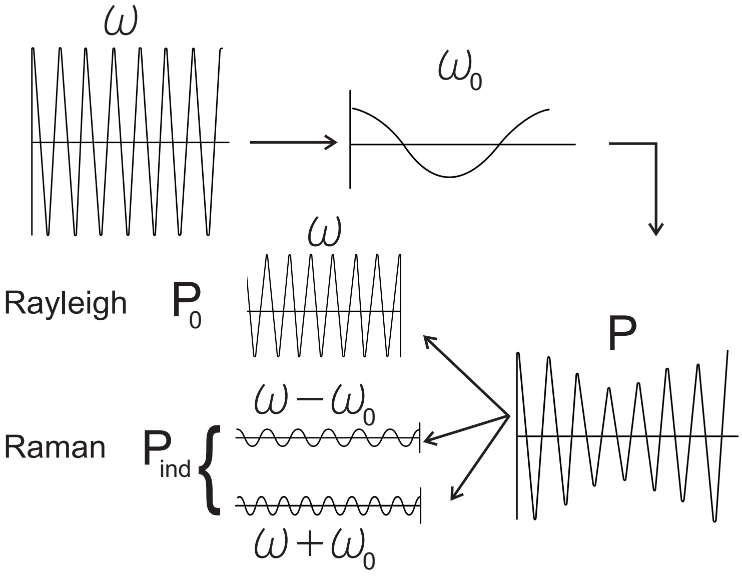

Figure 3.3: Schematics of an incident electromagnetic wave interacting with a material with a phonon frequency ω_0, creating thus an scattered electromagnetic wave with three frequency components, one associated with the Rayleigh scattering and two with the Raman scattering.

Brillouin zone as in first order Raman. Expanding Eq. 3.10 to second order and then following the same steps as before we are led to :

$$\begin{aligned}
\mathbf{P^2_{raman}} \quad & \propto \cos[(\mathbf{k}+\mathbf{q_a}+\mathbf{q_b})\cdot\mathbf{r}-(\omega+\omega_a+\omega_b)t] \\
& +\cos[(\mathbf{k}+\mathbf{q_a}-\mathbf{q_b})\cdot\mathbf{r}-(\omega+\omega_a-\omega_b)t] \qquad (3.15) \\
& +\cos[(\mathbf{k}-\mathbf{q_a}+\mathbf{q_b})\cdot\mathbf{r}-(\omega-\omega_a+\omega_b)t] \\
& +\cos[(\mathbf{k}-\mathbf{q_a}-\mathbf{q_b})\cdot\mathbf{r}-(\omega-\omega_a-\omega_b)t], \qquad (3.16) \\
& \qquad (3.17)
\end{aligned}$$

where we have supposed that two different phonons now contributes to the Raman scattering with wavevectors $\mathbf{q_a}$ and $\mathbf{q_b}$ and frequencies ω_a and ω_b. This two-phonon Raman scattering has the selection rule $\mathbf{q_a} \pm \mathbf{q_b} \sim \mathbf{0}$, showing that each phonon wavevector can be different from zero but the sum of the wavevectors has to be close to zero [76]. A Raman band is called as an overtone when $\omega_a = \omega_b$ and the two frequencies are summed $(\omega_a + \omega_a)$. Another special case of Raman scattering can occur with the presence of a defect with wavevector $\mathbf{d}$, and in this case the Raman selection rule is $\mathbf{q_a} \pm \mathbf{d} \sim \mathbf{0}$. We are going to describe two-phonon and defect-induced Raman scattering in graphene in more details in Sec. 3.2.

3.1.3 Microscopical approach to the Raman scattering, selection rules and the resonant Raman scattering

We begin the quantum mechanical treatment of Raman scattering by illustrating the Feynman diagram for a Stokes process in Fig. 3.4 (a) [76]. This diagram has three vertices, each one representing first-order time dependent pertubation in the system. The first vertex represents a initial state $|i\rangle$ of the system going to an excited state $|n\rangle$ due to electron-radiation interaction. In the second vertex, the state $|n\rangle$ of the system goes to the state $|n'\rangle$ due to an electron-phonon interaction. In the third and last vertex, there is a recombination of the electron-hole pair and the system goes to the final state $|f\rangle$ of the system. In the first vertex there is an absorption of a photon with energy $\hbar\omega_i$, in the second vertex there is an emission of a phonon with energy $\hbar\omega_{ph}$ and in the last vertex there is emission of a photon with energy $\hbar\omega_S$. We can define these four states of the system as:

$$\begin{aligned}
|i\rangle = &\quad |p_i, 0, p_{ph}, \psi_0\rangle, \\
|n\rangle = &\quad |p_i - 1, 0, p_{ph}, \psi_e^n\rangle, && (3.18) \\
|n'\rangle = &\quad |p_i - 1, 0, p_{ph} - 1, \psi_e^{n'}\rangle, && (3.19) \\
|f\rangle = &\quad |p_i - 1, 1, p_{ph} - 1, \psi_0\rangle, && (3.20)
\end{aligned}$$

where the four terms inside de brackets are the number of incident photons, number of scattered photons, number of phonons and the electronic state, respectively. The energies associated with these states are:

$$\begin{aligned}
E_i = &\quad p_i\hbar\omega_i + p_{ph}\hbar\omega_{ph} + E_v, \\
E_n = &\quad (p_i - 1)\hbar\omega_i + p_{ph}\hbar\omega_{ph} + E_c^n, && (3.21) \\
E_{n'} = &\quad (p_i - 1)\hbar\omega_i + (p_{ph} - 1)\hbar\omega_{ph} + E_c^{n'}, && (3.22) \\
E_f = &\quad (p_i - 1)\hbar\omega_i + \hbar\omega_S + (p_{ph} - 1)\hbar\omega_{ph} + E_v, && (3.23)
\end{aligned}$$

where E_v and E_c is the energy of the valence and condution for example. The overall of the Raman process can be alternately viewed following the three steps in Fig. 3.4 (b). However the horizontal lines in this picture does not represent the electronic energy levels of the system.

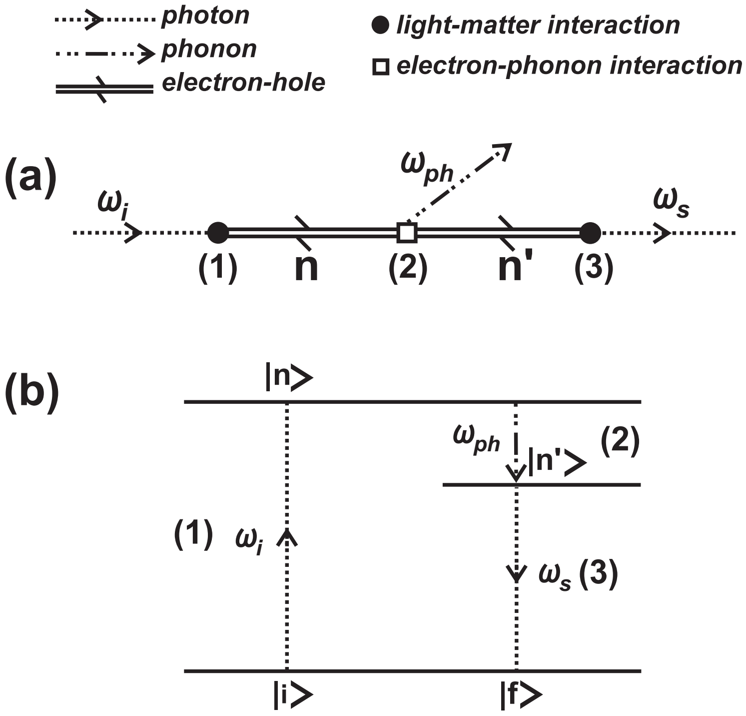

Figure 3.4: (a) Feynman diagram of the one-phonon Raman process. (b) Scheme of the Raman scattering depicted by the Feynman diagram. (The horizontal lines of part (b) do not correspond to the electronic levels, as discussed in the text).

To compute the Raman scattering probability of the process depicted in Fig. 3.4 (a) we start with the first vertex which contributes with a first order pertubation term (term inside the absorption probability in Eq. 3.6) in the form of [76]:

$$\sum_n \frac{\langle n|\mathcal{H}_{light}|i\rangle}{[\hbar\omega_i - (E_c^n - E_v)]}. \tag{3.24}$$

Multiplying the first vertex by the second, one related to the electron-phonon interaction, we are led to a second order term given by[76]:

$$\sum_{n,n'} \frac{\langle n'|\mathcal{H}_{el-ph}|n\rangle\langle n|\mathcal{H}_{light}|i\rangle}{[\hbar\omega_i - (E_c^n - E_v)][\hbar\omega_i - \hbar\omega_{ph} - (E_c^{n'} - E_v)]}. \tag{3.25}$$

Finally we multiply this last equation to the third vertex, which contributes with the emission of a photon, then we have [76]:

$$\sum_{n,n'} \frac{\langle f|\mathcal{H}_{light}|n'\rangle\langle n'|\mathcal{H}_{el-ph}|n\rangle\langle n|\mathcal{H}_{light}|i\rangle}{[\hbar\omega_i - (E_c^n - E_v)][\hbar\omega_i - \hbar\omega_{ph} - (E_c^{n'} - E_v)][\hbar\omega_i - \hbar\omega_{ph} - \hbar\omega_S]}. \tag{3.26}$$

The term $[\hbar\omega_i - \hbar\omega_{ph} - \hbar\omega_S]$ in the denominator gives the energy conservation rule of the Raman process and it should vanish. Then the Raman scattering probability can be written as [76]:

$$P_{raman} = \left(\frac{2\pi}{\hbar}\right)\left|\sum_{n,n'} \frac{\langle i|\mathcal{H}_{light}|n'\rangle\langle n'|\mathcal{H}_{el-ph}|n\rangle\langle n|\mathcal{H}_{light}|i\rangle}{[\hbar\omega_i - (E_c^n - E_v)][\hbar\omega_i - \hbar\omega_{ph} - (E_c^{n'} - E_v)]}\right|^2 \delta(\hbar\omega_i - \hbar\omega_{ph} - \hbar\omega_S). \tag{3.27}$$

In fact Eq. 3.27 is not the complete scattering probability of the Raman process, because there are five more possible permutations of time order for each event in the diagram depicted in Fig. 3.4 (a). The complete calculation can be found in Ref. [76], but the most important contribution indeed comes from the above equation [76].

The evaluation of Eq. 3.27 involves a number of different variables like the electron-phonon matrix elements. But if we only want to know if the probability of a Raman process is different from zero, we can make use of group theory [77]. First we should determine what is the irreducible representations that each one of the matrix elements transforms in the numerator of Eq. 3.27. Then the Raman process will occur if the direct product of these three irreducible representations contains the totally symmetric representation [77]. The Hamiltonian of the light-matter interaction in the electric dipole approximation transforms as the irreducible representation with basis function being x, y or z [77] which corresponds to the polarization of the light. The direct product of this representation with the irreducible representations of the states $|i\rangle$ (or $|n'\rangle$) and $\langle n|$ (or $\langle f|$) gives a final irreducible representation $\Gamma_{absorption}$ ($\Gamma_{emission}$) [77]. For the Hamiltonian of the electron-phonon coupling, the irreducible representation is the same as the phonon irreducible representation [78, 64]. Then the direct product of the electron-phonon irreducible representation and representation of the states $|n\rangle$ and $\langle n|$ will creates a representation Γ_{el-ph}. Then the Raman probability will be different from zero if [77]:

$$\Gamma_{absorption} \otimes \Gamma_{el-ph} \otimes \Gamma_{emission} \subset \Gamma_1, \tag{3.28}$$

where Γ_1 is the totally symmetric representation. The use of group theory is very useful to determine only the Raman activity. However a active Raman mode can only be observed depending on the strength of the electron-phonon coupling and resonance conditions [76].

The resonance condition for the Raman scattering is given by the denominator of Eq. 3.27. The Raman probability is strongly enhanced when the energy difference between incident photon ($\hbar\omega_i$) and the electron-hole energy ($E_c^n - E_v$) or between the scattered photon ($\hbar\omega_S = \hbar\omega_i - \hbar\omega_{ph}$) and electron-hole energy ($E_c^{n'} - E_v$) is zero [76]. We call resonant Raman scattering (RRS) when Raman probability is enhanced due to a vanishing denominator of Eq. 3.27. RSS has been largely applied to study not only the phonon structure of materials but its electronic properties as well. In resonance conditions, we can replace the sum of the n states in Eq. 3.27 by only one term that connects directly one state $|a\rangle$ with a photon energy $\hbar\omega_a$. In this case to avoid a unphysical situation where the denominator vanishes, we include an imaginary term $i\Gamma_a$ which is a damping constant due to the finite lifetime of the excitation. Then in resonance conditions Eq. 3.27 can be written as [76]:

$$P_{raman} \approx \left(\frac{2\pi}{\hbar}\right) \left| \frac{\langle i|\mathcal{H}_{light}|a\rangle\langle a|\mathcal{H}_{el-ph}|a\rangle\langle a|\mathcal{H}_{light}|i\rangle}{[E_c^a - \hbar\omega_a - i\Gamma_a][E_c^a - \hbar\omega_S - i\Gamma_a]} \right|^2 . \tag{3.29}$$

3.2 First- and second-order Raman scattering in graphene

3.2.1 The Raman spectra of monolayer graphene

The most prominent features in the Raman spectra of monolayer graphene are the so-called G band appearing at $1582\,\mathrm{cm}^{-1}$ and the G' band (also called 2D band in the literature [38]) at about $2700\,\mathrm{cm}^{-1}$ using laser excitation at 2.41 eV (Fig. 3.5 (a)). There is also a low intensity peak near $\sim$2400 cm^{-1} which we call here by G* band. In the case of a disordered or defective sample (Fig. 3.5 (b)), we can also see the so-called disorder-induced D-band, at about half of the frequency of the G' band (around $1350\,\mathrm{cm}^{-1}$ using laser excitation at 2.41 eV). Additionally to the D-band there is another weak disorder-induced feature which appears at $\sim 1620\,\mathrm{cm}^{-1}$ (D' band).

The G band is associated with the doubly degenerate (iTO and LO) phonon mode (E_{2g} symmetry) at the BZ center. In fact, the G-band is the only band coming from a normal first order Raman scattering process in graphene systems. The process giving rise to the G-band can be viewed in Fig. 3.6 (a). On the other hand, the G' and D-bands originate from a second-order process, involving two iTO phonons near the K point for the G' band or one iTO phonon and one defect in the case of the D-band [79]. To further elucidate that the presence of defects is necessary for the observation of the D-band in the Raman spectra of graphene, we show in Fig. 3.7 a Raman mapping of the G and D bands in monolayer graphene sample in which defects had been created by focusing an ion beam (FIB) at six different positions. It is possible to observe on the right panel of Fig. 3.7 that the D band intensity is strong only where the FIB has created defects in the graphene.

Both the D and G' bands exhibit a dispersive behavior, i.e. their frequencies in the Raman spectra changes as a function of the energy of the incident laser, E_{laser}. The D-band frequency ω_D upshifts with increasing E_{laser} in a linear way over a wide laser energy range (including the visible range), the slope ($\partial\omega_D/\partial E_{\mathrm{laser}}$) being about 50 cm^{-1}/eV. The slope of ($\partial\omega_{G'}/\partial E_{\mathrm{laser}}$) is about twice that of the D-band, i.e., around 100 cm^{-1}/eV [80, 81, 82].

The origin and the dispersive behavior in the frequency of the D and G' bands originate from a double resonance (DR) Raman process [83, 84, 85]. The double-resonance process shown in Fig. 3.6(b) and (c) begins with an electron of

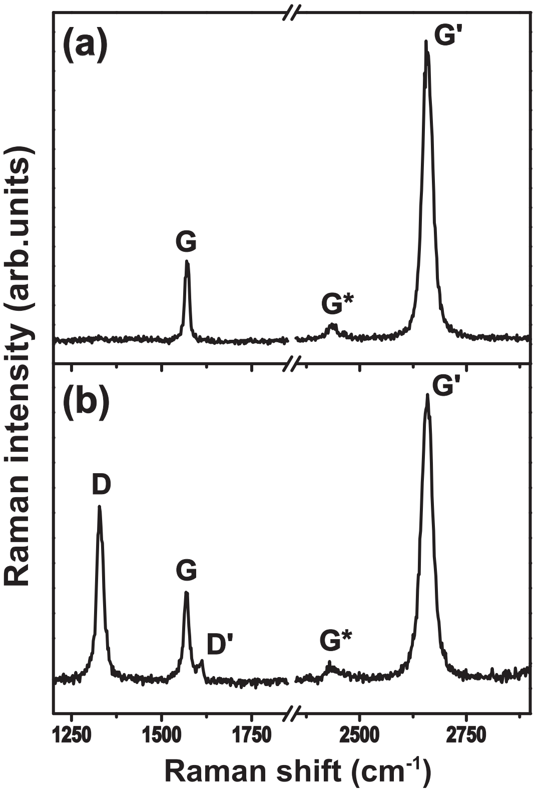

Figure 3.5: (a) Raman spectrum of a *defect free* monolayer graphene showing the main Raman features, the G, G^* and G' bands taken with a laser excitation energy of 2.41 eV. (b) Raman spectrum of a defective monolayer graphene sample, in which two disorder-induced D and D' Raman bands also appear.

wavevector $\mathbf{k}$ measured from the K point absorbing a photon of energy E_{laser}. The electron is inelastically scattered by a phonon of wavevector $\mathbf{Q}$ and energy E_{phonon} to a point belonging to a circle around the K' point, with momentum $\mathbf{k}'$. The electron scatters then back to the $\mathbf{k}$ state, and emits a photon by recombining with a hole. In the case of the D band, the two scattering processes consist of one *elastic* scattering event by defects of the crystal and one *inelastic* scattering event by emitting or absorbing a phonon, as shown in Fig. 3.6. In the case of the G'-band, both processes are *inelastic* scattering events involving two phonons. This double resonance mechanism is called an *inter-valley* process because it connects points in circles around inequivalent K and K' points in the first Brillouin zone of graphene. On the other hand, the double resonance process responsible for the originates responsible for the D' band (Fig. 3.6 (e)) is an *intra-valley* process, since it connects two points belonging to the same circle around the K point (or the K'

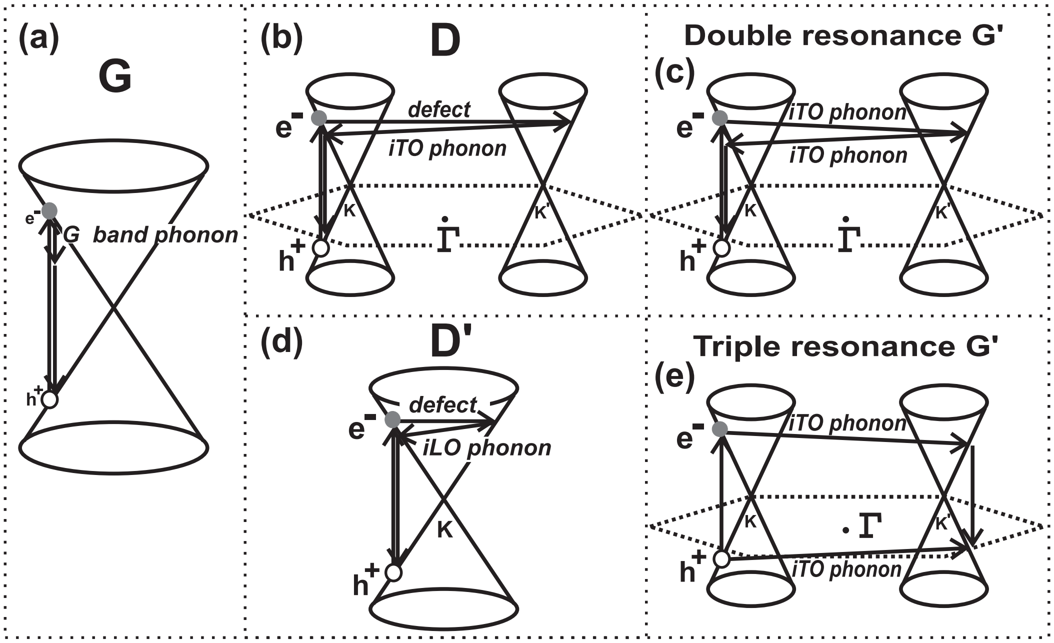

Figure 3.6: (a) First-order Raman process which gives rise to the G band. One-phonon second-order Raman process giving rise to the (b)intervalley D band and (d) intravalley D′ band. (c) two-phonon second-order Raman spectral processes giving rise to the G′ band. (e) Schematic view of a possible triple resonance giving rise to the G′ Raman band in graphene.

point) [85].

The intervalley process depicted in Fig. 3.6 (b,c) can be alternatively viewed in Fig. 3.8, which shows an electron initially around the K point represented by the vector **k** measured from the K point being scattered by a phonon with wavevector **Q**, going to an intermediate state around the K′ point represented by **k**′. The vectors **u** and **u**′ are the initial and intermediate electronic wavevectors, measured from the Γ point, and given by:

$$\begin{aligned} \mathbf{u} &= \mathbf{K} + \mathbf{k} \\ \mathbf{u}' &= \mathbf{K}' + \mathbf{k}' \end{aligned} \tag{3.30}$$

where **K** and **K**′ are the wavevectors of the K and K′ points respectively. The phonon wavevector **Q** measured from the Γ point is $\mathbf{Q} = \mathbf{u}' - \mathbf{u}$. Substituting

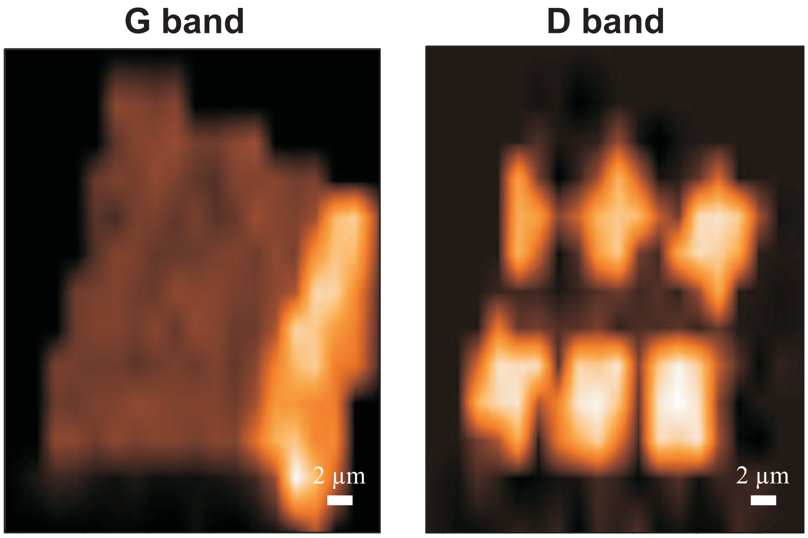

Figure 3.7: Raman mapping of a graphene sample in which defects have been created in six localized positions. The brightness in the color of the figure represents how intense is the Raman band over the sample. The left panel shows the mapping of the G band of monolayer graphene and a small part on the right due to fewlayer graphene. The right panel shows the D band mapping where it is possible to observe that the intensity is much greater at the six position in which defects were created. This Raman image was done by L. M. Malard with collaboration of B. Archanjo (Inmetro) and A. Jorio (UFMG).

Eq. 3.30 into the previous expression for $\mathbf{Q}$, we have the phonon wavevector $\mathbf{Q}$ measured from the Γ point given by:

$$\mathbf{Q} = \mathbf{K} + \mathbf{k}' - \mathbf{k}, \tag{3.31}$$

where we have used the fact that $\mathbf{K}' - \mathbf{K} = \mathbf{K}$.

For convenience, we will work with the phonon vector $\mathbf{q}$ measured from the K point, which is related to the phonon wavevector $\mathbf{Q}$ measured from the Γ point by $\mathbf{q} = \mathbf{Q} - \mathbf{K}$ (red shaded area in Fig. 3.8). The phonon vector $\mathbf{q}$ meaured from the K point can be written only on terms of the initial and intermediate electronic wavevectors as:

$$\mathbf{q} = \mathbf{k}' - \mathbf{k}. \tag{3.32}$$

From now on, we will use this notation for the phonon wavevector **q** written in terms of the initial **k** and intermediate **k**′ electron wavevectors, all of them measured from the K point.

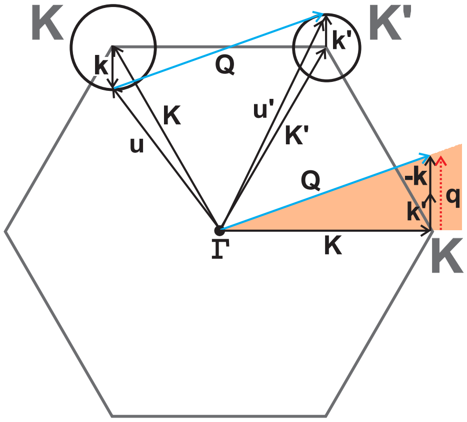

Figure 3.8: The vectors **u**, **u**′ and **Q** represent the wavevectors of the initial electronic state, the intermediate electronic state and of the associated phonon, respectively, measured from the Γ point. The vectors **k**, **k**′ and **q** represent the same states measured from the K point.

In principle, many different initial electronic states around the Dirac point and phonons with different symmetries and wavevectors can satisfy the double resonance (DR) condition. However, due to (1) the existence of singularities in the density of phonon states which satisfy the DR condition, (2) the angular dependence of the electron-phonon scattering matrix elements, and (3) destructive interference effects when the Raman transition probability is calculated, only a few specific DR processes contribute to the Raman G' and D bands [79, 47]. For example, only iTO and iLO branches are observed in the intervalley and intravalley DR processes, respectively, because the corresponding phonons are strongly coupled to electrons along the high-symmetry directions associated with the singularities in the DR phonon density of states [86].

When E_{laser} is increased relative to the Dirac point, the resonance k vector for the electron moves away from the K point. In the DR process, the corresponding q vector for the phonon increases with increasing k. Thus by changing the laser energy, we can probe the phonon dispersion relation (ω versus q). This effect is obtained experimentally from the dispersion of the phonon energy as a function of E_{laser}.[87] A tunable laser system can directly show this dispersive behavior for the D-band and G'-band in the Raman spectrum.

In a DR Raman process, two resonance conditions for three scattering events must be satisfied, in which the intermediate k' state is always a real electronic state and either the initial or the final k state is a real electronic state[88, 89]. However, the Raman process can also occur by scattering of holes. In the special case of graphene, where the valence and conduction bands are almost mirror bands, this can lead to an important effect, that is the triple resonance (TR) Raman process. For example, we can see in Fig. 3.6(e) that, instead of the electron being scattered back by a phonon with $-q$, the hole will be scattered instead. In this case, the electron-hole generation is a resonant process, both electron and hole scattering will be resonant, and finally the electron-hole recombination at the opposite side with respect to the K point will also be resonance. Therefore, for the triple resonance process all steps in the usual double resonance process now become resonant. This triple-resonance condition might explain why the G'-band is more intense than the G-band in monolayer graphene.

3.2.2 Selection rules for the double resonance Raman scattering in graphene

In this section we describe in more details why the double resonance Raman mechanism giving rise to the D and G′ bands is stronger for certain directions in first Brillouin zone of graphene. Next we also show which phonon components in the double resonance model gives rise to the G* band.

3.2.2.1 The quasi-1D character of the double Resonance Raman scattering in graphene

In principle the double resonance Raman scattering that gives rise to the D, G′ and G* bands can involve many different initial (around the K point) and intermediate states (around the K′ point) represented in Fig. 3.6. To show this effect in more details we illustrate three different possible intervalley scattering process in the first Brillouin zone of graphene in Fig. 3.9. An electron with initial state given by the vector **k** is scattered to an state near the K′ point with vector **k**′ by a phonon with wavevector **Q**. In Fig. 3.9 it is possible to see that the vector **q** always fall inside of the solid circle plotted around the K point for any possible intervalley scattering. The radius of the outer circle of the various possible phonons wavevectors in Fig. 3.9 corresponds to the sum of the moduli of the initial and final electron vectors ($q = k + k'$) and can be approximated by $q \approx 2k$, while the inner circle represents the difference ($q = k - k'$) between them and can be approximated by $q \approx 0$.

By considering the sum of all possible phonon vectors shown in Fig. 3.9, and also considering the electronic trigonal warping effect [Fig. 3.10 (a)], Samsonidze *et al.* [86] calculated the DR phonon density of states for a incident laser energy of 2.41 eV as shown in Fig. 3.10 (b). The two first red vertical lines of Fig. 3.10 (b) (the two inner circles of Fig. 3.10 (a)) corresponds to phonon vectors with $q \approx 0$. The third and fourth vertical red lines of Fig. 3.10 (b) (the two outer circles of Fig. 3.10 (a)) corresponds to phonon vectors with $q \approx 2k$. These for vertical lines show that the double Resonance intensity comes from phonon wavevectors close to zero or $2k$.

In order to see the phonon wavevectors ($q \approx 0$ or $q \approx 2k$) that contributes to the Raman intensity we have to calculate the full Raman cross section for the double resonance given by [90]:

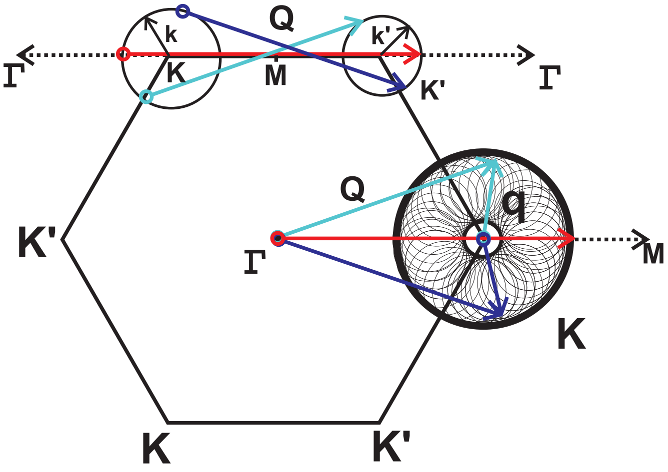

Figure 3.9: On top of the figure we illustrate different K-K′ intervalley scattering by a phonon **q** that can contributes to the double resonance Raman scattering. In the middle the same process are depicted with the phonon wavevector **q** translated to the Γ point. With this translation it is possible to observe that all possible scattering falls within the circle around the right K point.

$$\sigma_{raman} \propto \sum_f \left| \sum_{n,n',n''} \frac{\langle f|\mathcal{H}_{light}|n''\rangle\langle n''|\mathcal{H}_{el-ph}|n'\rangle\langle n'|\mathcal{H}_{el-ph}|n\rangle\langle n|\mathcal{H}_{light}|i\rangle}{[(E_i - E_n)(E_i - E_{n'})(E_i - E_{n''})]} \right|^2 \delta(E_i - E_f), \tag{3.33}$$

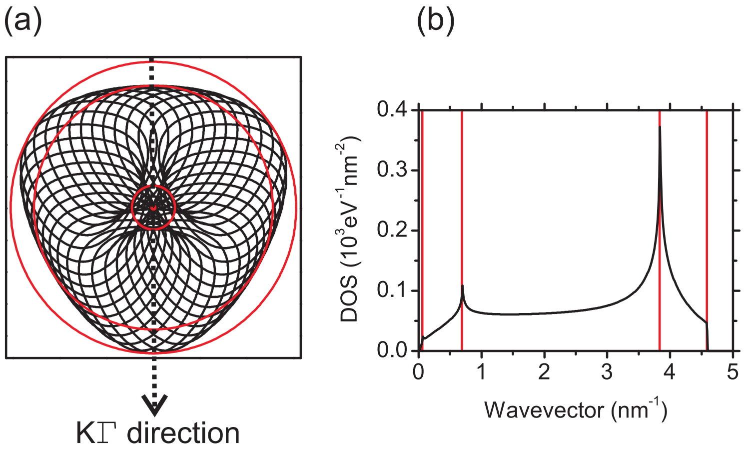

Figure 3.10: (a) The collection of all possible phonon wavevectors for the double resonance Raman model including the trigonal warping effect. The two inner red circles refers to the $q \approx 0$ phonons, and the two outer ones for $q \approx 2k$. (b) The phonon density of states that satisfy the double resonance Raman model as a function of q measured from the K point. The four red vertical lines refers to discontinuity of the derivative in the phonon DOS, where the first two refers to the two inner circles and the two last lines to the outer circles.

where the electron initially at the valence band in the state $|i\rangle$ (i) absorbs a photon and goes to the state $|n\rangle$, (ii) is scattered to the state $|n'\rangle$ by emitting a phonon, (iii) is scattered back to the state $|n''\rangle$ by emitting another phonon, and (iv) it recombines emitting a scattered photon going to the final state $|f\rangle$ [90]. The full calculation of Eq. 3.33 has been done by Maultzsch *et al.* [79], and they found that there is a destructive intereference for phonon wavevectors satisfying the $q \approx 0$ condition [79]. Then, the main contribution to the double resonance Raman scattering comes from phonons near $q \approx 2k$.

Another important result from the phonon density of states depicted in Fig. 3.10 (a,b) is that due to the trigonal warping effect, there is a large density of states for phonons vectors near the KM direction for the third red circle in Fig. 3.10 (a) and third red line in Fig. 3.10 (b). For this reason, we can consider that the phonon wavevector direction that mainly contributes to the double resonance Raman process comes from the KM direction (electrons with initial and final states along the KΓ direction). This result shows that the electron initial and intermediate states are mainly along the high symmetry line Γ-K-M-K′-Γ.

3.2.2.2 The D and G′ bands

Let us discuss now the symmetry of the phonons that participate in the DR Raman process. In Figure 3.11 (a) we show four different processes along the Γ-K-M-K′-Γ which contributes to the D and G′ bands. Processes (1) and (2) have initial and intermediate wavevectors $\mathbf{k}$ and $\mathbf{k}'$ pointing in the same direction, and then the phonon magnitude given by Eq. 3.32 is $q = k' - k \approx 0$, which has been shown by Maultzsch *et al.* to be negligible due to interference effects [79]. On the other hand, the vectors $\mathbf{k}$ and $\mathbf{k}'$ point in opposite directions for process (3) and (4) and, therefore, the associated phonon wavevector $\mathbf{q}$ has the maximum magnitude given by $q = k' + k \approx 2k$.

Process (3) has initial and intermediate electronic states along the ΓK direction, and then the final phonon wavevector is along the KM direction, as shown in Fig. 3.11 (b) when $\mathbf{Q}$ is translated to the Γ point. However in principle, different phonon branches along this direction can contribute to the double resonance Raman scattering and it is necessary to calculate the electron-phonon matrix elements for these processes [47, 91]. Figure 3.12 shows a calculation performed by Samsonidze *et al.* [86] considering extend tight binding model. The calculation of the matrix elements for four different phonon branches (iTO, iLO, iLA and iTA) is perfomed by fixing the initial electronic wavevector along the KΓ direction [Fig. 3.12(a)] as a function of the angle ϕ between intermediate k' state direction and the KM direction. It is possible in Fig. 3.12(a) to observe that when k' is along the opposite KΓ direction ($\phi = 270°$), the larger contribution is from the iTO phonon mode [86, 47, 91].

We have shown that the D and G′ DR Raman bands exhibit a quasi-1D behavior along the Γ-K-M-K′-Γ line and that the phonon mode that mainly contributes for these bands is the iTO phonon along the KM direction [47].

3.2.2.3 The G band*

Process (4) depicted in Fig. 3.11 (a) has initial and intermediate electronic states along the KM direction, and then the phonon wave vector is along the ΓK line (Fig. 3.11 (c)). In the calculation of the electron-phonon matrix elements shown in Fig. 3.12 (b) the intermediate electronic state k' along the KM direction refers to $\phi = 90°$ [86, 47, 91]. The two phonon modes that contributes to process (4) are the iLA and iTO modes. Then, the G^* Raman band can be described by the double resonance Raman model with one phonon belonging to the iTO branch

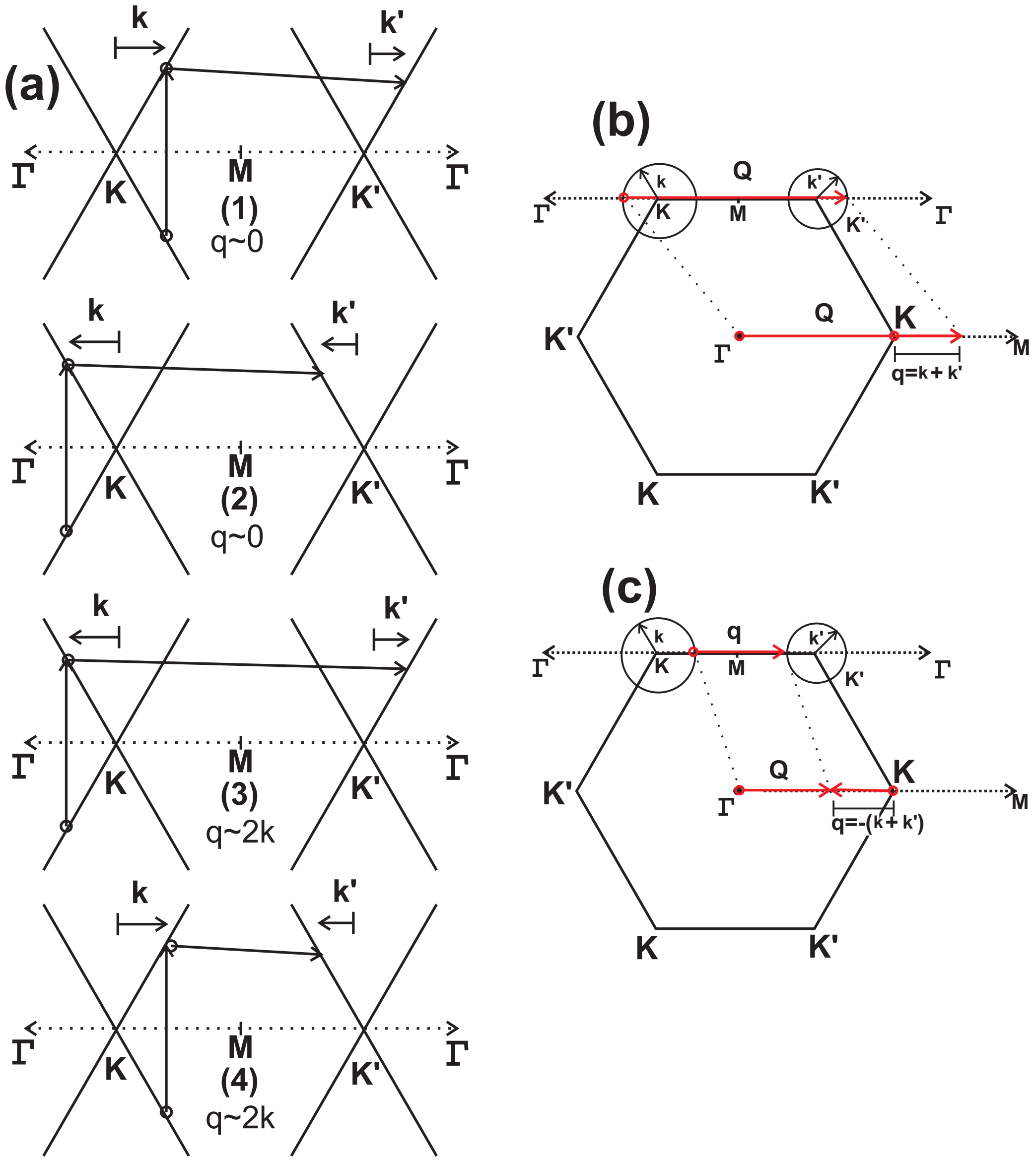

Figure 3.11: (a) The four process along the Γ-K-M-K′-Γ line which can generates the double resonance Raman bands. (b) Top view of the process (3) in first Brillouin zone, where it is possible to observe that *q* is along the KM direction. (c) Same as (b) but for process (4) but with *q* along the ΓK direction.

and the other to the iLA branch along the ΓK direction [47].

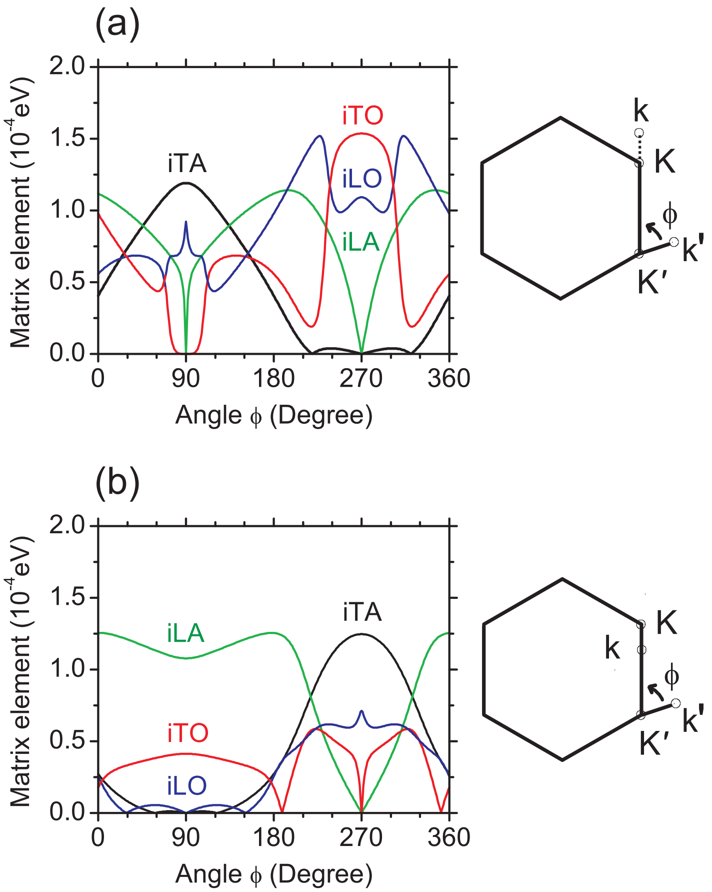

Figure 3.12: Electron-phonon matrix elements for four different phonons branches as a function of the angle ϕ of the intermediate k_1 state given that the initial state k_0 is: (a) along the ΓK direction; (b) along the KM direction.

3.3 Raman spectroscopy to determine the number of graphene layers

In the case of Bernal AB stacking of graphene (see §3.2), Ferrari *et al.* [38] showed that it is possible to use the second order G' (or 2D) feature in the Raman spectra of graphene to learn about the number of layers in a graphene sample. As in other sp^2 carbons, the G' feature in the Raman spectrum originates from the double resonance Raman process [84, 85], and selectively links electrons and phonons in the graphene dispersion relations. [38, 39, 40, 46, 47] Starting from monolayer graphene, we first consider the DR Raman process (see §3.2) which is depicted in Fig. 3.6(c). Here we see that the selection rules discussed in §3.2 for electron-phonon scattering occurring along the $K\Gamma K'$ direction has to satisfy the scattering process shown in Fig. 3.6(c) as discussed before [88, 47]. Fig. 3.5(a) shows a Raman spectrum measured with a laser energy of 2.41 eV, where it is possible to see that the G' band for monolayer graphene (1-LG) exhibits a single Lorentzian feature with a full width at half maximum (FWHM) of ~ 24 cm^{-1}. What is remarkable about this spectrum is the large intensity of the G' band relative to the G-band, and this large relative intensity of the G' band can be understood in terms of a triple resonance process shown in Fig. 3.6(e). This is a unique spectrum for all sp^2 carbons where all three steps in the double resonance process (see Fig. 3.6(e) are resonant because of the linear $E(k)$ dispersion.

In the case of bilayer graphene (2-LG) with Bernal AB layer stacking, both the electronic and phonon bands split into two components with special symmetries. The electrons in 2-LG have a parabolic $E(k)$ dispersion relation showing a k^2 dependence near $k = 0$ and have two conduction and two valence bands [1, 2, 92] as shown in Fig. 3.13 and in Chapter 2. The phonons are also affected by the interlayer interaction and they also split into components with symmetric and anti-symmetric vibrations. For these two components the motion of the carbon atoms in the upper and lower layers correspond to different irreducible representations, such that the motion in the two layers are in phase with respect to each other for one component and out of phase for the other component. For the case of 2-LG, the DR Raman conditions involve more combinations than in the case of 1-LG where there is only one main contribution to the G' band.

Figure 3.13(a) shows a schematic view of the bilayer graphene electronic structure where the upper (lower) and lower (upper) branches in the valence (conduction) band are labeled as π_1 (π_1^*) and π_2 (π_2^*), respectively. The major steps of the DR Raman process occur along the T axis (ΓK) along which the π_2 and π_1^* bands belong to the T_1 totally symmetric irreducible representation, while the π_1 and π_2^* bands have odd T_2 symmetry relative to the inversion symmetry [57]. Now, for computing the number of resonant conditions involved in the DR Raman process, we are left with electrons in only two excited electronic states with $\mathbf{k}$ vectors near the K point which will be scattered by a phonon to an electron state with wave vectors near the K' point. This electron-phonon scattering can now occur involving phonon with two symmetries T_1 and T_2. For the case of a T_1 phonon and the electron initial state at π_1^* (T_2 symmetry) or π_2^* (T_1 symmetry), the scattering can occur between the $\pi_1^* \rightarrow \pi_1^*$ or $\pi_2^* \rightarrow \pi_2^*$ bands, respectively. The corresponding symmetry-allowed scattering processes by a T_2 phonon will connect bands of dif-

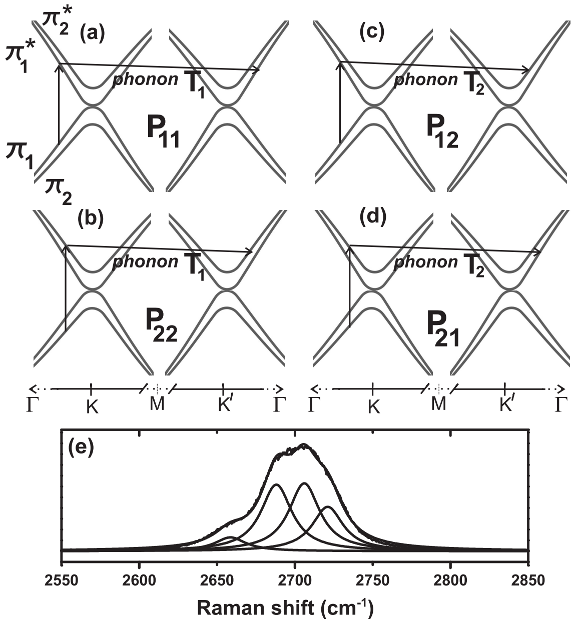

Figure 3.13: Schematic view of the electron dispersion of bilayer graphene near the K and K' points showing both π_1 and π_2 bands. The four DR Raman processes are indicated: (a) process P_{11}, (b) process P_{22}, (c) process P_{12}, and (d) process P_{21}. The phonon symmetries are also indicated in each process. (e) Measured G' Raman band of bilayer graphene for 2.41 eV laser energy. The four fitted Lorentzians are also shown with peak frequencies at 2658, 2688, 2706, and 2721 cm^{-1}, respectively, and FWHM of $\sim$ 24 cm^{-1} [46].

ferent symmetries, i.e., $\pi_1^* \rightleftarrows \pi_2^*$, where the product of the matrix elements are invariant for a symmetry-allowed process. At this point is worth to mention that the complete analysis of these Raman processes will be fully discussed in Chapter 5.

These four different P_{ij} processes are depicted in Fig. 3.13(a-d), where i (j) denote an electron scattered from (to) each conduction band $\pi_{i(j)}^*$. Processes P_{11} and P_{22} come from an iTO phonon with T_1 symmetry, while processes P_{12} and P_{21} come from an iTO phonon with T_2 symmetry. These four different scattering processes give rise to four Raman peaks in the G' spectrum. Figure 3.13 (e) shows the Raman spectra of a bilayer graphene sample fitted with four Lorentzians [46] with a FWHM of $\sim$ 24 cm^{-1} for each peak. If the valence and conduction bands were mirror images of one another, then processes P_{12} and P_{21} would be degenerate. Experimentally the fitting with four peaks gives a better fit, showing that asymmetries between the valence and conduction band are present in 2-LG [46].

For trilayer graphene (3-LG), we can show that the number of allowed Raman peaks in the G' band is fifteen [57]. The 3-LG electronic structure has three valence and three conduction bands. The absorption selection rules gives rise to five possible initial states near the K point that can participate in the DR Raman process [57]. Also, trilayer graphene has three phonon branches that will scatter this 5 possible states from K to K′ points, giving rise to 15 possible Raman peaks in the G′ band. To correctly identify the G′ Raman band lineshape for 3-LG, one should model the DR Raman process, by considering this 15 different transitions, but the energy separations of many of these fifteen different processes turn out to be very close to each other from an experimental standpoint. Figure 3.14 (a-c) shows Raman spectra of a 3-LG sample, with each spectrum fitted with a different number of peaks or laser excitation energy values. Experimentally it is found that the minimum number of peaks with a FWHM of ~ 24 cm^{-1} necessary to correctly fit the G′ in this case is six as shown in Figs. 3.13(c) and (d) for $E_{laser} = 2.41$ and 2.18 eV, respectively.

The G′ band continues to evolve with the number of graphene layers until the final material that we must consider is bulk graphite. For crystalline 3D graphite (see §2) we can describe the G′ band with two peaks (see Fig. 3.15(e)). Figure 3.15 compares the Raman spectra in the G′ band region for (a) monolayer, (b) bilayer, (c) trilayer, (d) four layer and (e) HOPG, showing the evolution of the Raman spectra with the number of layers. Cançado *et al.* [93] attributed the two peaks of the G′ band for HOPG to be a convolution of process from $k_z = 0$ to $k_z = \pi/c$. The turning point of the Raman spectra, distinguishing the G' band for HOPG from that for few layer graphene, starts to happen at 4-LG. From Fig. 3.15 (d) it is possible to see that now the high frequency side of the G' band has a larger intensity than that for fewer layers, indicating the passage to HOPG, which has its higher intensity peak at higher frequencies.

It is important to notice that the identification of the number of layers by Raman spectroscopy is well established only for graphene samples with AB Bernal stacking. Graphene samples made by the mechanical exfoliation of natural or HOPG graphite leads to graphene flakes that have predominantly AB stacking, but this is not necessarily the case for graphene samples made by other growth

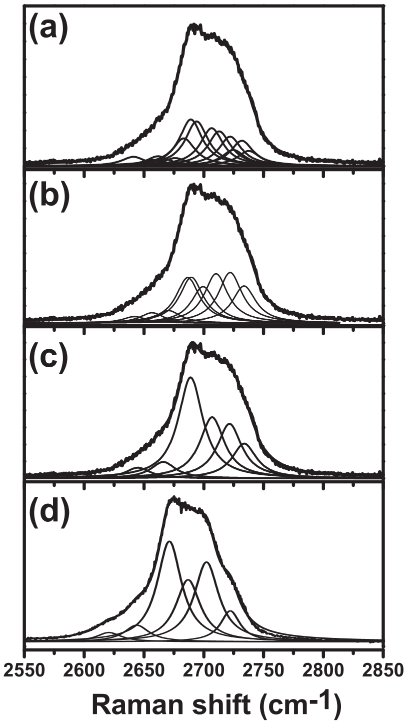

Figure 3.14: Measured 3-LG with 2.41 eV laser energy and fitted with (a) 15 Lorentzians, (b) 9 Lorentzians and (c) 6 Lorentzians. (d) Measured trilayer graphene with 2.18 eV laser energy, showing that 6 Lorentzians with FWHM of $\sim$ 24 cm^{-1} are needed to fit the G′ feature for 3-LG.

methods [94].

For example, turbostratic graphite, in which the stacking of the graphene layers is disordered with respect to one another along the *c* axis, shows a Raman G' band that is similar to that of monolayer graphene but with a larger linewidth. The absence of an interlayer interaction between the graphene planes makes the Raman spectra of turbostratic graphite look much like that for monolayer graphene. The reason for this is that the electronic structure for turbostratic graphite can be described in the same way as graphene, but now with a broadening of the G' feature due to the relaxation of the DR Raman selection rules associated with the random orientation of the graphene layers with respect to each other. This is reflected in the Raman spectra of the G' band as a single Lorentzian, just as in monolayer graphene, but now for turbostratic multilayer graphene with a FWHM of $\sim$ 40-60 cm^{-1} [95] instead of $\sim$ 24 cm^{-1}, as is found for monolayer graphene. Also the relative intensity of the G' feature to the G-band $I_{G'}/I_G$ is much smaller

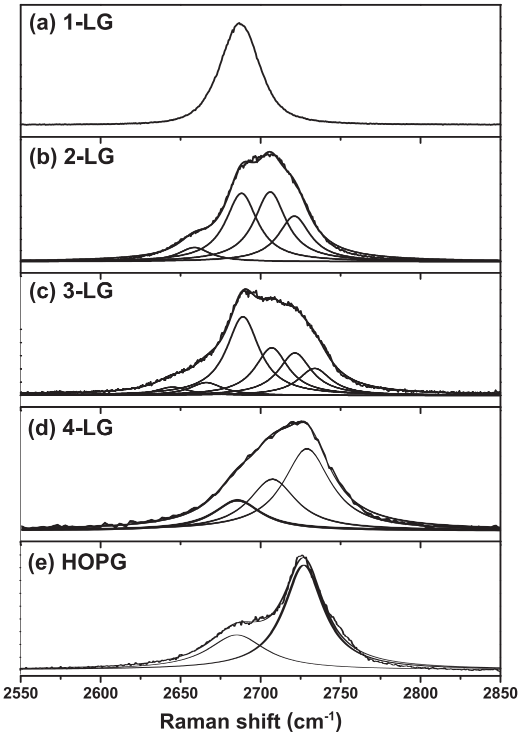

Figure 3.15: The measured G' Raman band with 2.41 eV laser energy for (a) 1-LG, (b) 2-LG , (c) 3-LG, (d) 4-LG and (e) HOPG.

for turbostratic graphite and the frequency is shifted from that of 1-LG.

We have shown in this section how the G'-band can be used to determine the number of layers of a graphene sample with AB stacking. Raman spectroscopy thus provides a useful and fast method to quantify the number of graphene layers [38] and also provides some information on the stacking order. Also we explained the origin of the number of peaks in the G' band that is associated with differences in the electronic and phonon dispersion relations, and that depend on the number of layers in n-LG.

Chapter 4

Experimental Methods

In this chapter we discuss the experimental methods which were used in this work. In section 4.1 we discuss how the graphene sample were prepared and how it is possible to identify them by optical microscopy. In section 4.2 we describe graphene samples subjected to an electric field, and the calculation of the induced charge in graphene as a function of the applied gate voltage. In section 4.3 we describe the Raman instrument used in the experiments.

4.1 Sample preparation

In 2004, Novoselov *et al.* [8, 9] showed an easy method to prepare and to find graphene samples on top of a silicon wafer covered with a silicon oxide layer. Although being only one atom thick, a monolayer graphene turns out to be visible in a optical microscope with the correct choice of the thickness of the silicon oxide layer substrate [8, 96]. The micro-mechanical cleavege of graphite is possible due to the weak van der Waals interlayer coupling in layered materials like graphite [9]. By using a scotch tape it is possible to separate the graphite layers until you reach only one layer of graphene. This technique is exemplified in Fig. 4.1 where a thick piece of natural graphite is successively cleaved and then deposited in a silicon oxide substrate. Then, by searching the sample with an optical microscope, it is possible to identify a single layer from few-layers of graphene.

We have used in our experiments a p-doped silicon substrate covered with a 300 nm silicon oxide layer. This silicon oxide thickness ensure us the best optical contrast between the monolayer graphene and the bare substrate as we will discuss later. There are two important points for the sample preparation: the starting graphite material and the substrate cleaning. The starting graphite material should have large crystal sizes to ensure both in-plane and out-plane correlations. Usually, we used natural graphite flakes from Nacional de Grafite, which has large domain sizes as compared to HOPG. The sample cleaning has to be done prior to the graphite deposition and has two steps, the first is to clean the bare substrate by acetone followed by iso-propanol in ultrasound. The second step is wash the samples in pirana solution (2/3 of sulphuric acid and 1/3 of hydrogen peroxide) for 10 minutes in a hot plate at 70° C. This second step can be done by other technics such as oxygen plasma. The cleaning of the substrate is a crucial step to ensure that graphene will be attached to the substrate surface, yielding larger graphene flakes. After the substrate is cleaned, a graphite flake is deposited on a scotch tape (Nitto Tape SWT-10+ from Semiconductor Equipment Corporation, USA) and cleaved for about 4 times, making sure the the graphite is homogeneous around the scotch tape. Then finally the final scotch tape containing thinner graphite tape is deposited on the silicon substrate, then, it is carefully removed. Now the substrate is ready for inspection on a optical microscope to find graphene flakes. On the optical microscope thick graphite flakes has a yellow color, thinner graphite flake has blue colors. The color of monolayer graphene is almost a shadow compared to the substrate color.

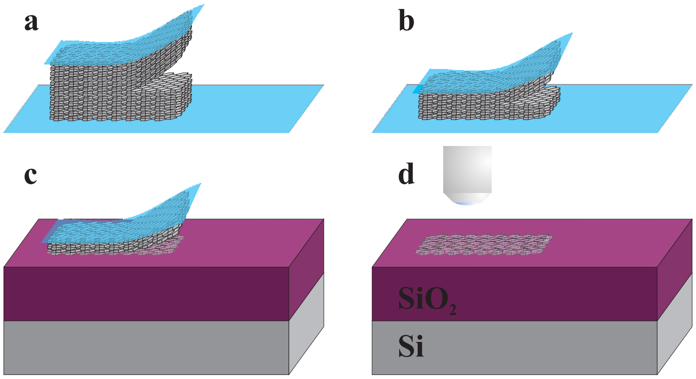

Figure 4.1: Micro mechanical cleavage of graphite with a scotch tape from (a) to (b), then the tape is deposited on the silicon substrate on (c) followed by the search of graphene flakes with a optical microscope.

Monolayer graphene only absorbs about 2.3% of the incident light [97], but the optical contrast of graphene can be greatly improved by the correct choice of substrate [96]. By shining white light on a silicon substrate covered with a silicon oxide layer with thickness l, the multiple-beam interference between the different layers (silicon-silicon oxide-graphene) can lead to a good contrast between graphene and the silicon oxide substrate [96]. The problem of thin film interference can be understood by calculating the reflectance and transmitance using the transfer matrix method [98][1]. Consider the case of Fig. 4.2, where we have a slice of a dielectric medium with index of refraction n_1 and thickness l between two media with index of refraction n_0 e n_T. The incident light is normal to the surface with an electric field amplitude E_0, and the reflected and transmitted light have amplitudes $E_0^{'}$ and E_T, respectively. Inside the dielectric medium the fields are given by E_1 e $E_1^{'}$ for the incident and reflected light, respectively, as shown in Fig. 4.2.

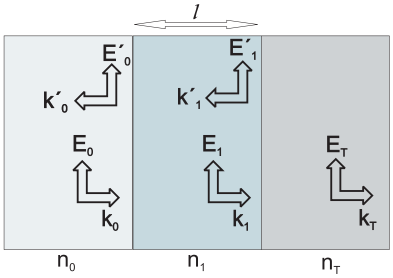

Figure 4.2: Scheme for a electromagnetic wave passing trough a medium with different indices of refraction.

The boundary conditions require that the electric and magnetic field must be continues at each interface, which are given in table 4.1 [98].

	First interface	Second interface
Electric field	$E_0 + E_0^{'} = E_1 + E_1^{'}$	$E_1 e^{ikl} + E_1^{'} e^{-ikl} = E_T$
Magnetic field	$H_0 - H_0^{'} = H_1 - H_1^{'}$	$H_1 e^{ikl} - H_1^{'} e^{-ikl} = H_T$
or	$n_0 E_0 - n_0 E_0^{'} = n1 E_1 - n_1 E_1^{'}$	$n_1 E_1 e^{ikl} - n_1 E_1^{'} e^{-ikl} = n_T E_T$

Table 4.1: Boundary conditions for the electric and magnetic fields.

Eliminating the amplitudes E_1 e $E_1^{'}$, we have:

$$1 + \frac{E_0^{'}}{E_0} = (\cos kl - i\frac{n_T}{n_1}\sin kl)(\frac{E_T}{E_0}), \tag{4.1}$$

---

[1] We will present here the calculation of the optical contrast considering the optical properties of a macroscopic media. In principle, this approximation is not valid for a one atom thick layer. However, it has been shown that the prediction using this kind of calculation to graphene systems give good results when compared with experiments.

$$n_0 - n_0 \frac{E_0'}{E_0} = (-in_1 \sin kl + n_T \cos kl)(\frac{E_T}{E_0}). \tag{4.2}$$

Or in the matrix form:

$$\begin{pmatrix} 1 \\ n_0 \end{pmatrix} + \begin{pmatrix} 1 \\ -n_0 \end{pmatrix} \frac{E_0'}{E_0} = \begin{pmatrix} \cos kl & \frac{-i}{n_1} \sin kl \\ -in_1 \sin kl & \cos kl \end{pmatrix} \begin{pmatrix} 1 \\ n_T \end{pmatrix} \frac{E_T}{E_0}. \tag{4.3}$$

Introducing the reflection coefficient [98]:

$$r = \frac{E_0'}{E_0}, \tag{4.4}$$

and the transmission coefficient [98]:

$$t = \frac{E_T}{E_0}, \tag{4.5}$$

then Eq. 4.3 can be rewritten as:

$$\begin{pmatrix} 1 \\ n_0 \end{pmatrix} + \begin{pmatrix} 1 \\ -n_0 \end{pmatrix} r = \mathbf{M} \begin{pmatrix} 1 \\ n_T \end{pmatrix} t, \tag{4.6}$$

where **M** is the transfer matrix [98]:

$$\mathbf{M} = \begin{pmatrix} \cos kl & \frac{-i}{n_1} \sin kl \\ -in_1 \sin kl & \cos kl \end{pmatrix}, \tag{4.7}$$

where $k = \frac{2\pi}{\lambda}$ or $k = \frac{2\pi n_1}{\lambda_0}$, where λ_0 is wavelength of the light in the vacuum. This method can be generalized for N layers with refraction indexes $n_1, n_2, n_3, ..., n_N$ and thickness $l_1, l_2, l_3, ..., l_N$. Eq. 4.6 will be given by [98]:

$$\begin{pmatrix} 1 \\ n_0 \end{pmatrix} + \begin{pmatrix} 1 \\ -n_0 \end{pmatrix} r = M_1 M_2 M_3 ... M_N \begin{pmatrix} 1 \\ n_T \end{pmatrix} t = \mathbf{M} \begin{pmatrix} 1 \\ n_T \end{pmatrix} t, \tag{4.8}$$

where each matrix $M_1, M_2, M_3, ..., M_N$ has the same form as Eq. 4.7, with appropriate values of k, l and n. The overall matrix $\mathbf{M}$ given by the product of the individual matrices can be written as [98]:

$$\mathbf{M} = \begin{pmatrix} A & B \\ C & D \end{pmatrix}. \tag{4.9}$$

Solving Eq. 4.8, the reflection coefficient can be written as:

$$r = \frac{An_0 + Bn_T n_0 - C - Dn_T}{An_0 + Bn_T n_0 + C + Dn_T}, \tag{4.10}$$

and the reflectance R (the ratio of reflected and incident intesities) is given by:

$$R = |r^2|. \tag{4.11}$$

To calculate the optical contrast of graphene we consider the scheme given in Fig. 4.3, where the incident light comes from the air passing trough the graphene layer, then to the silicon oxide layer and to the silicon substrate. The contrast is calculated as [96]:

$$contrast = \frac{R_{graphene} - R_{oxide}}{R_{graphene} + R_{oxide}}, \tag{4.12}$$

where $R_{graphene}$ is the reflectance with the graphene and R_{oxide} is reflectance without the graphene. In Fig. 4.4 (a,b) we show the constrast of the system shown in Fig. 4.3 as a function of the wavelength of the light, for a 100 nm and 300 nm thickness oxide. It is possible to observe that the contrast is enhanced for wavelengths in the visible range, being possible to observe graphene flakes by optical microscopy. Fig. 4.4 (c) shows the contrast changes (color scale) as a function of the light wavelength and the silicon oxide thickness, showing that the best choice

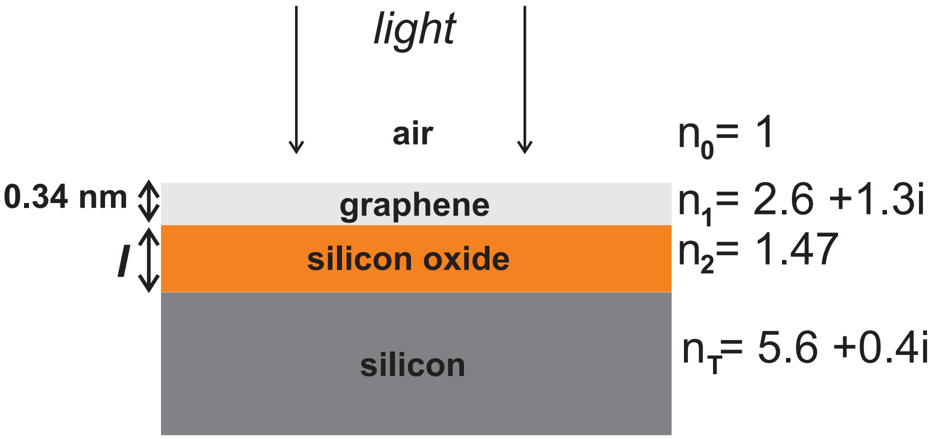

Figure 4.3: Scheme for calculating the optical contrast for graphene on top of silicon oxide layer, and the refractive indices at $\lambda = 500$ nm.

for the silicon oxide thickness are $l = 100$ nm and 300 nm. Fig. 4.5 shows a optical image of a monolayer graphene on top of a 300 nm silicon oxide layer, showing that the single layer of atoms is visible by eye.

Although the scotch tape technique is useful for fundamental studies of graphene, the transfer of graphene from the laboratory to the industry depends on the development of large scale production of graphene [12]. For this, many approaches have been developed for large scale growth, using chemical vapor deposition methods, thermal decomposition of silicon carbide and chemical exfoliation of graphene (for a review see reference [12]). Although the large scale growth is promising, much has to be done to produce samples with the same quality as the mechanical exfoliated one.

All the samples used in our experiments were obtained by mechanical exfoliation of graphite using the method described above.

4.2 Gated graphene devices

It is possible to induce charges in graphene by applying a potential difference V_g between the graphene and the silicon substrate [8, 10, 11]. In this case, we have a parallel plate capacitor, where one plate is the graphene itself, the other one is the conducting p-doped silicon substrate, and the dielectric medium between them is the silicon oxide layer. We can model the amount of charge induced in graphene

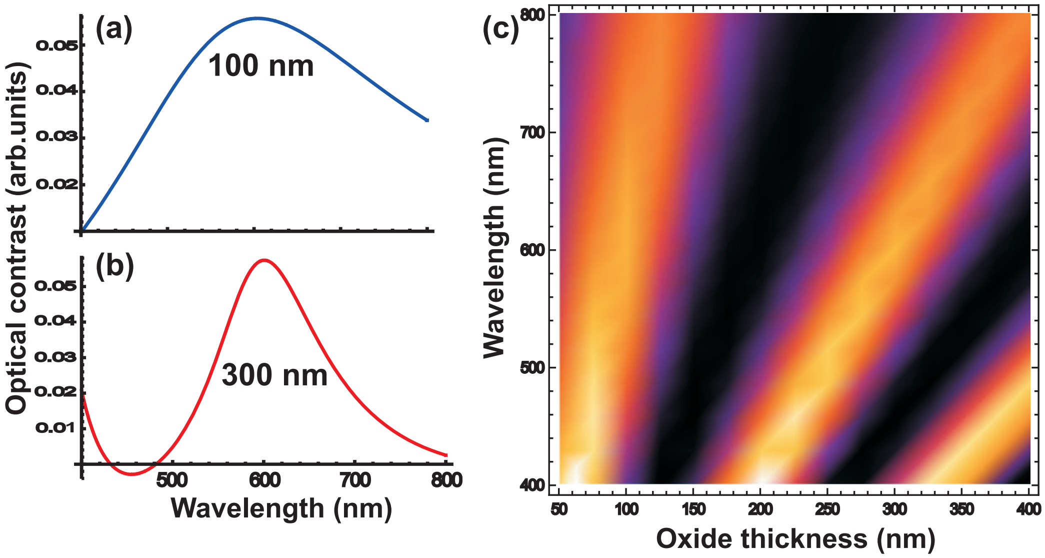

Figure 4.4: Calculated contrast of graphene on top of silicon oxide substrate using the parameters show in the Figure 4.3 [96] for (a) 100 nm and (b) 300 nm silicon oxide thicknesses. (c) Color map of the contrast (brighter the color, larger the contrast), as a function of the light wavelength and the silicon oxide thickness.

by noticing that the capacitance C of this system is [99]:

$$C = \frac{A\varepsilon_0\varepsilon}{d}, \tag{4.13}$$

where A is the area of the capacitor, ε_0 and ε is the permittivity of free space and the silicon oxide, respectively, and d is the silicon oxide thickness. Then, the number of electrons of charge e per unit of area n transferred to the graphene by applying a potential difference of V_g, using the electrical permittivity ε and the thickness $d = 300nm$ for the silicon oxide, is given by [10]:

$$n = \frac{A\varepsilon_0\varepsilon(V_g - V_D)}{Aed} = 7.2 \times 10^{10} cm^{-2} V^{-1} (V_g - V_D), \tag{4.14}$$

where V_D is the gate voltage needed to move the Fermi level to the Dirac point due to intrinsic doping of the sample. Usually, for as-prepared (pristine) graphene samples, V_D is different from zero, mostly due to induced charge from the water of the ambient atmosphere [8, 10, 11].

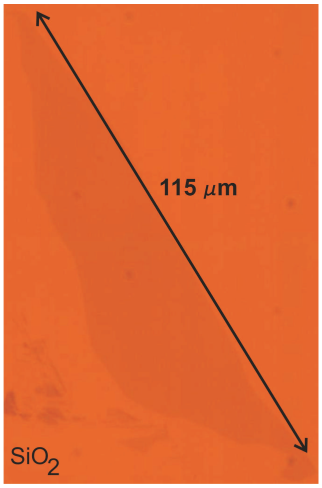

Figure 4.5: Graphene on top of a silicon substrate with a silicon oxide layer of 300 nm thickness. The picture was taken in a optical microscope with a red filter to enhance even more the contrast.

Figure 4.6 (a) shows the schematic view of a graphene device, where an applied gate voltage V_g can induce the potential difference between the the silicon substrate and the graphene with a gold contact. Several different litography technics can be applied to put contacts on the graphene surface, like optical and electron litography. However, other approaches can be used, like direct soldering of indium contact in graphene [100]. Fig.4.6 (b) shows two bilayer graphene devices contacted by this method.

From Eq. 4.14 it is possible to relate the induced charge density as a function of gate voltage V_g. In order to obtain the expression relating the Fermi energy as a function of induce charge change, we first note that number of states per unit of area in a two-dimensional system is given by [101]:

$$n = \frac{N}{A} = \frac{g k_F^2}{4\pi}, \tag{4.15}$$

where N is the total number of states, A is the area of the unit cell of the reciprocal space, g is the spin and valley degenerency and k_F is the wavevector at the Fermi level. Eq. 4.15 relates how the density of available states in a two dimensional system changes with k_F. Then it is possible to correlate how the induced charge density from Eq. 4.14 in a two dimensional system modifies k_F as given in Eq.

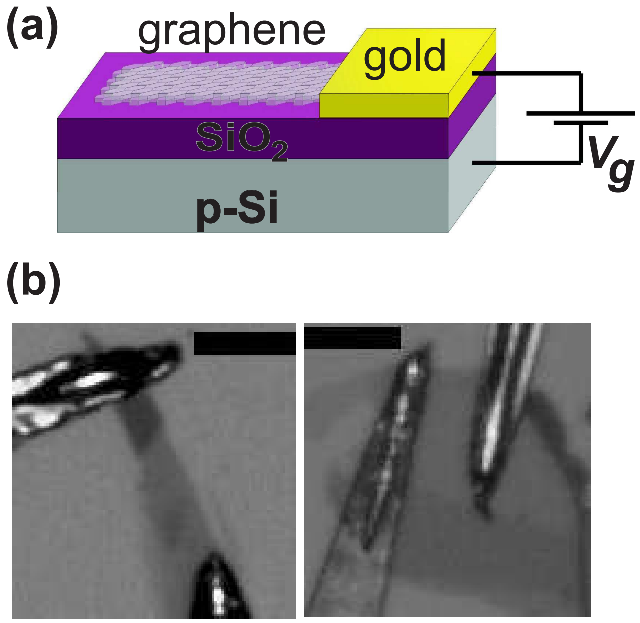

Figure 4.6: (a)Schematic view of graphene devices. A gold contact is made on the graphene, a variable voltage V_g applied between the contact and the p type silicon substrate. The device is a parallel plate capacitor where the silicon oxide layer is the dielectric medium. (b) Two bilayer graphene samples contacted with indium wire directly onto the surface of the graphene.

4.15.

For monolayer graphene, assuming the linear dispersion is given as $E_F = \hbar v_F k_F$. Substituting k_F into Eq. 4.15 and also using Eq. 4.14, the Fermi energy E_F can be written in terms of V_g as [8]:

$$E_F = \hbar v_F \sqrt{\pi 7.2 \times 10^{10} cm^{-2} V^{-1} |V_g - V_D|}. \tag{4.16}$$

For bilayer graphene, considering only the first electronic band (near the neutrality point), the parabolic electronic dispersion is given by:

$$E_F = -\frac{\gamma_1}{2} + \sqrt{\gamma^2 k_F^2 + \frac{\gamma_2^2}{4}}, \qquad (4.17)$$

where $\gamma = \frac{\sqrt{3}\gamma_0 a}{2}$, and a is the lattice constant. Making the same procedure done for monolayer graphene, we have [68]:

$$E_F = \frac{1}{2}\left(-\gamma_1 + \sqrt{4\pi\gamma^2 7.2 \times 10^{10} cm^{-2} V^{-1} |V_g - V_D| + \gamma_1}\right). \qquad (4.18)$$

which gives the Fermi level change as a function of the applied gate voltage.

Since usually the amount of induced charge in the system does not move the Fermi energy very far away from the neutrality point, we assume that the Fermi level for electron or hole doping are the same but with different signs.

4.3 Raman instrumentation

Raman spectroscopy experiments can be made in a variety of spectrometers and light sources. The spectrometer is mainly composed by diffraction gratings, a detector, mirrors and slits. Figure 4.7 (a) shows a simplified scheme of a single monocromator which is composed by one diffraction grating G_1, one slit S_1 and the detector D. The scattered light from a sample, for example, is focused on S_1, dispersed on G_1 and is detected by D. The resolution of the spectrometer is given by the number of groves/mm of the diffraction grating, the size of the slit S_1 and the distance between the grating and the detector. Higher the number of groves/mm, smaller the slit size and longer the light path, higher the resolution of the spectrometer. For Raman scattering experiments, where the Raman bands are much less intense than to the Rayleigh component, we have to use filters before S_1 to reject the Rayleigh light. Usually we use notch filters for this purpose, but we need to use different filters for each different laser light sources.

Another kind o spectrometer commonly used for Raman experiments consists of a triple monocromator system, shown in Fig. 4.7 (b). This spectrometer uses three gratings G_1, G_2 and G_3, three slits S_1, S_2 and S_3 and a detector. Now, the two first gratings can be used to reject the Rayleigh light of the laser source, and this configuration is called the subtractive mode. In this case, G_1 disperses the light passing though S_2, and by adjusting the size of S_2 it is possible to reject almost completely the Rayleigh light. Then the light is focused by G_2 into slit S_3, going through G_3 and being dispersed again to the detector. The triple monocromator system has some advantages compared to the monocromator, because you can continuously change the energy (or wavelength) of the laser sources instead using only those for which you have the specific notch filter. Also, it is possible to measure Raman bands much closer to the Rayleigh light. However the biggest problem of triple monocromator is that the light intensity is reduced by a factor of 5-10 when compared to the single monochromator due to the additional gratings.

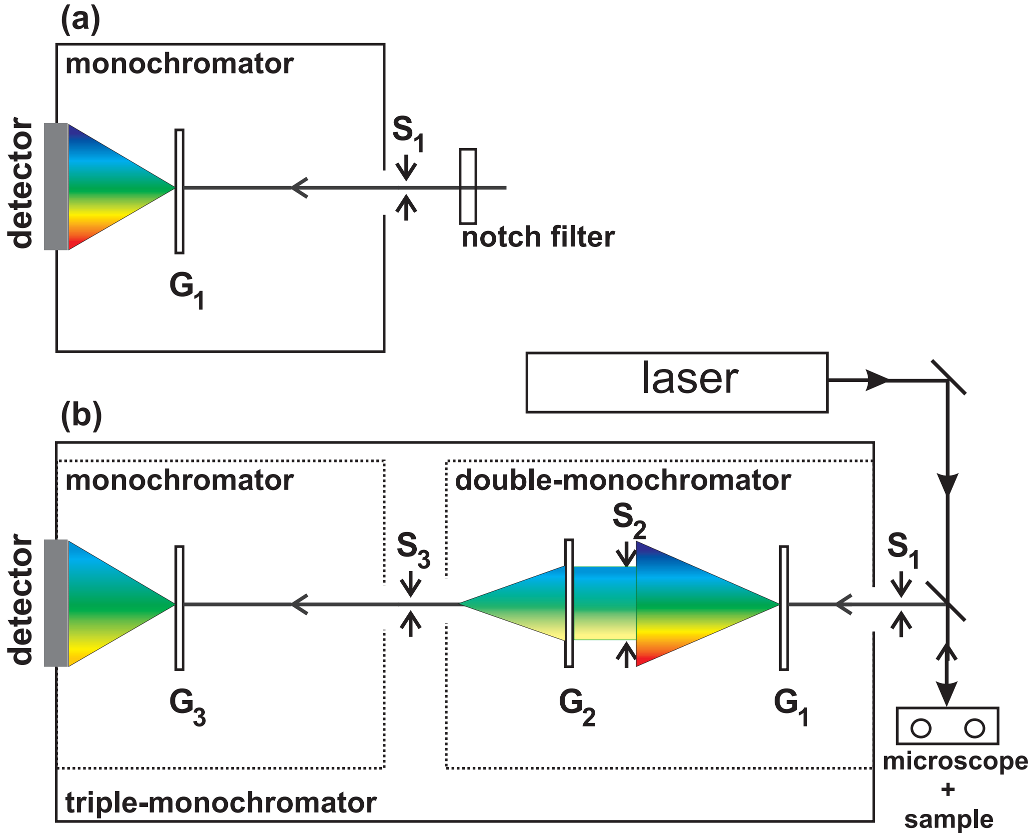

Figure 4.7: (a)Schematic view of a monochromator. (b)Schematic view of a triple monochromator, and also our expermental setup showing the laser source and the microscope used to focus the incident laser on the sample.

The Raman spectrometer used in this work was a Dilor XY triple spectrometer, using an Olympus microscope to focus the incident light on the sample and to collect the backscattered light to the spectrometer [shown in Fig. 4.7 (b)]. With the use of the microscope it is possible to focus the laser light in a spot size of ~ 1 μm, which is an advantage for studying exfoliated graphene samples whose size usually is about 10x10 μm.

The Raman signal is usually weak if compared to other optical process like luminescence. Also, the light source frequency width has to be smaller than typical Raman widths. These two requirements is fulfilled by using laser sources to study the Raman scattering process. In this work we have used several laser lines to study the Raman scattering in graphene. Three laser sources has been used in our experiments: an Argon-Kripton laser, dye lasers and titanium- sapphire laser.

The Ar-Kr laser has the following discrete laser energies: 457.9 nm, 465.8 nm, 472.7 nm, 476.5 nm, 488.0 nm, 496.5 nm, 501.7 nm, 514.5 nm, 520 nm, 528.7 nm, 568.2 nm and 647.1 nm. The dye laser is a tuneable laser with continuous laser lines from 530 to 660 nm, depending on the dye. The Ti-Sa laser is also a continuous laser source ranging from 730 to 900 nm. These last two continuous laser systems require a high power laser to pump them, and for that we have used an Argon laser with 6 W power.

Chapter 5

Group theory in *N*-layer graphene systems

This chapter presents a group theory analysis for electrons and phonons in monolayer, bilayer and trilayer graphene, extending for N-layers depending if N is even or odd, all with Bernal (AB) stacking. The selection rules for electron-radiation interaction within the dipole approximation and for electron scattering by phonons are derived. With these selection rules, we discuss the double-resonance Raman (DRR) scattering process, which has been widely used to characterize the number of layers [38, 39, 40] and to probe their electronic and vibrational properties [46, 47]. Finally, we also discuss the differences when mono and bilayer graphene are exposed to external electrical fields, giving insight on the gap opening in the biased bilayer graphene [21, 102, 103, 20, 22] and different selection rules for the electron-phonon scattering (EPS) process.

Section 5.1 gives the symmetry properties for monolayer and N-layer graphene depending if N is even or odd. The monolayer and bilayer graphene are also considered in the presence of an electric field perpendicular to the graphene plane. Section 5.2 presents the selection rules for the electron-radiation interaction. Section 5.3 shows the Γ point Raman and infrared active modes. We extend the electron-phonon selection rules to points in the interior of the Brillouin zone and address the DRR process for monolayer, bilayer and trilayer graphene in section 5.4. We give in Appendix C the character tables, the equivalence character and representation for monolayer, N-even and N-odd graphenes for each point of the Brillouin zone. These tables will be useful as a guide thought this Chapter.

5.1 Symmetry Properties

5.1.1 Group of the wave vector

Figure 5.1(a,d) shows the hexagonal real space for the monolayer graphene with two inequivalent atoms in the unit cell. The origin is set at the highest symmetry point, i.e. at the center of an hexagon. The reciprocal space is shown in Fig. E.1(g) highlighting the high symmetry points Γ, K, K′, M and lines T, T′, Σ. Any other generic point outside the high symmetry lines and points is named here *u*. The monolayer graphene on an isotropic medium has the space group P6/*mmm* (D_{6h}^1) in the Hermann-Mauguin (Schoenflies) notation. At the Γ point, the group of wavevector (GWV) is isomorphic to the point group D_{6h} (the Schoenflies character tables for the point groups can be found in Ref. [77] and at the Appendix C).

The real space for bilayer and trilayer graphene with AB Bernal stacking are show in Figs. 5.1(b,e) and (c,f), respectively. The symmetries for N-layer graphene, with N even or odd (from now on, N≠ 1), are the same as for bilayer and trilayer graphene, respectively. The main symmetry operation distinguishing the point groups between even and odd layers are the horizontal mirror plane, which is absent for N even, and the inversion, which is absent for N odd. The point groups isomorphic to the GWV for monolayer, N-layer graphene (N even and odd), and for N infinite (graphite) are listed in table 5.1 for all points and lines in the first Brillouin Zone (BZ). The GWV for N-layers graphene are subgroups of the GWV for single layer graphene. The direct product between the group from N even and N odd gives the graphene GWV, i.e.

$$\{G_{even}|0\} \otimes \{G_{odd}|0\} = \{G_{monolayer}|0\}.$$

On graphite, the wavevector point groups are isomorphic to the wavevector point groups of monolayer graphene, but differ fundamentally for some classes where a translation of $c/2$ is present, graphite belonging to the P6_3/*mmc* (D_{6h}^4) non-symorphic space group.

5.1.2 Lattice vibrations and π electrons

The representations for the lattice vibration ($\Gamma_{lat.vib.}$) and for the π electrons (Γ_π) are given by $\Gamma_{lat.vib.} = \Gamma^{eq} \otimes \Gamma^{vector}$ and $\Gamma_\pi = \Gamma^{eq} \otimes \Gamma^{z}$, respectively, where

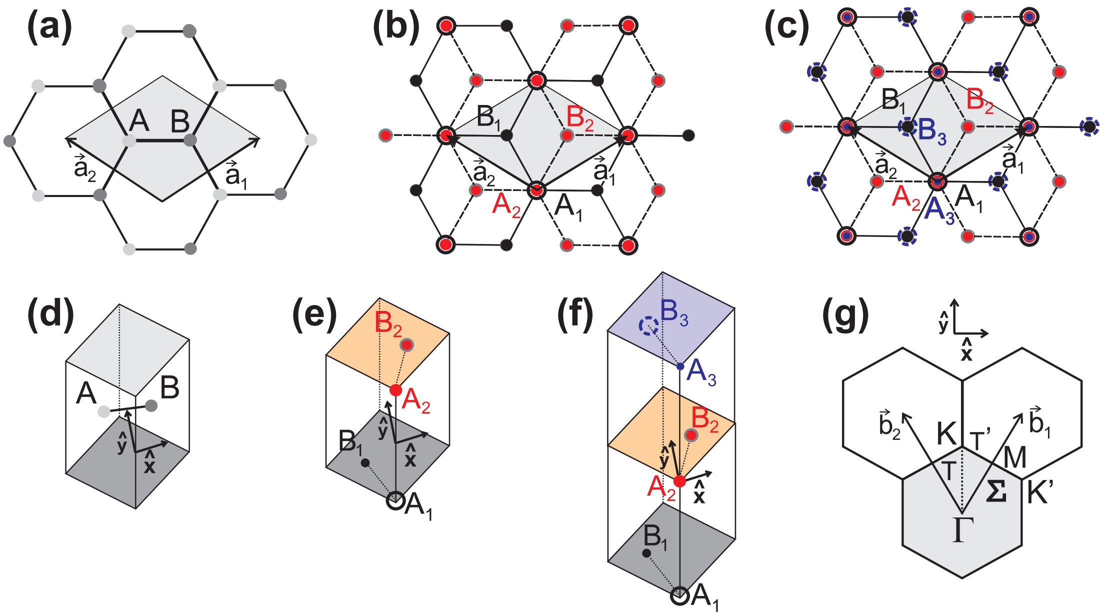

Figure 5.1: (color online)(a) The real space top-view of a monolayer graphene showing the non-equivalent A and B atoms. (b) The real space top-view of bilayer graphene. Black dots plus black open circles, and red dots represent the atoms in the lower and upper layers, respectively. (c) The real top-view trilayer graphene. Black dots plus black open circles, red dots and blue dots plus traced blue circles represent the atoms in the lower, middle and upper layers, respectively. The three dimensional unit cells of (d) monolayer, (e) bilayer and (f) trilayer graphene. (g) The reciprocal space showing the 1^{st} Brillouin zone in light gray, the high symmetry points and lines and the two primitive vectors.

Table 5.1: The space groups and wavevector point groups for monolayer, N-layer graphene and graphite (N infinite) at all points in the BZ.

	Space group	Γ	K (K′)	M	T (T′)	Σ	u
Monolayer	$P6/mmm$	D_{6h}	D_{3h}	D_{2h}	C_{2v}	C_{2v}	C_{1h}
N even	$P\bar{3}m1$	D_{3d}	D_3	C_{2h}	C_2	C_{1v}	C_1
N odd	$P\bar{6}m2$	D_{3h}	C_{3h}	C_{2v}	C_{1h}	C_{2v}	C_{1h}
N infinite	$P6_3/mmc$	D_{6h}	D_{3h}	D_{2h}	C_{2v}	C_{2v}	C_{1h}

Γ^{eq} is the atom equivalence representation and Γ^{vector} is the representation for the vectors x, y and z. For Γ_π we used only Γ^z, which is the irreducible representation for the vector z, since π electrons in graphene are formed by p$_z$ electronic orbitals. The results for all points and lines in the first BZ for the $\Gamma_{lat.vib.}$ are found in Table 5.2 and for the Γ_π in Table 5.3.

Table 5.3 shows that the π electrons in monolayer graphene are degenerated at the K (Dirac) point, as obtained by theory [33]. Figures 5.2(a), (b) and (c) show the electronic structure of a monolayer, bilayer and trilayer graphene, respectively, calculated via density functional theory (DFT) [104, 105, 106]. The symmetry assignments of the different electronic branches shown in Fig. 5.2 were made according to the DFT projected density of states.

Table 5.2: The $\Gamma_{lat.vib.}$ wavevector point-group representations for monolayer and N-layer graphene at all points in the BZ.

	Monolayer	**N even**	**N odd**
Γ	$\Gamma_2^- + \Gamma_5^- + \Gamma_4^+ + \Gamma_6^+$	$N(\Gamma_1^+ + \Gamma_3^+ + \Gamma_2^- + \Gamma_3^-)$	$(N-1)\Gamma_1^+ + (N+1)\Gamma_2^- +$ $(N+1)\Gamma_3^+ + (N-1)\Gamma_3^-$
K[1]	$K_1^+ + K_2^+ + K_3^+ + K_3^-$	$N(K_1 + K_2 + 2K_3)$	$NK_1^+ + NK_1^- + [f(N)+2]K_2^+ +$ $[f(N-2)]K_2^{+*} + NK_2^- + (N-1)K_2^{-*}$[2]
M	$M_1^+ + M_2^+ + M_3^+ + M_2^- +$ $M_3^- + M_4^-$	$N(2M_1^+ + M_2^+ + M_1^- + 2M_2^-)$	$2NM_1 + (N-1)M_2 + (N+1)M_3 + 2NM_4$
T(T′)	$2T_1 + T_2 + 2T_3 + T_4$	$3N(T_1 + T_2)$	$(3N+1)10T^+ + (3N-1)T^-$
Σ	$2\Sigma_1 + 2\Sigma_3 + 2\Sigma_4$	$N(4\Sigma_1 + 2\Sigma_2)$	$2N\Sigma_1 + (N-1)\Sigma_2 + (N+1)\Sigma_3 + 2N\Sigma_4$
u	$4u^+ + 2u^-$	$6Nu$	$(3N+1)u^+ + (3N-1)u^-$

Table 5.3: The Γ_π wavevector point-group representations for monolayer and N-layer graphene at all points in the BZ.

	Monolayer	**N even**	**N odd**
Γ	$\Gamma_2^- + \Gamma_4^+$	$N(\Gamma_1^+ + \Gamma_2^-)$	$(N-1)\Gamma_1^+ + (N+1)\Gamma_2^-$
K[1]	K_3^-	$\frac{N}{2}(K_1 + K_2 + K_3)$	$(\frac{N-1}{2})K_1^+ + (\frac{N+1}{2})K_1^- + g(N)K_2^{+*} + g(N-2)K_2^+ +$ $g(N)K_2^- + g(N+2)K_2^{-*}$ [3]
M	$M_3^+ + M_2^-$	$N(M_1^+ + M_2^-)$	$(N-1)M_1 + (N+1)M_4$
T(T′)	$T_2 + T_4$	$N(T_1 + T_2)$	$(N-1)T^+ + (N+1)T^-$
Σ	$2\Sigma_4$	$2N\Sigma_1$	$(N-1)\Sigma_1 + (N+1)\Sigma_4$
u	$2u^-$	$2Nu$	$(N-1)u^+ + (N+1)u^-$

The bilayer graphene with AB Bernal stacking [see Fig. 5.1(b,e)] is also a zero gap semiconductor composed by two conduction and two valence π bands, and the electrons exhibit a parabolic dispersion near the K point. Two bands are

---

[1] The K′ point irreducible representations are given by the complex conjugate of the K point.

[2] Where $f(N) = \sum_{m=0}^{\infty}[\Theta(N-4m-2) + 3\Theta(N-4m-4)]$, where $\Theta(x)$ is equal to 0 if $x < 0$ and equal 1 otherwise.

[3] Where $g(N) = \sum_{m=0}^{\infty}\Theta(N-4m-2)$, where $\Theta(x)$ is equal to 0 if $x < 0$ and equal 1 otherwise.

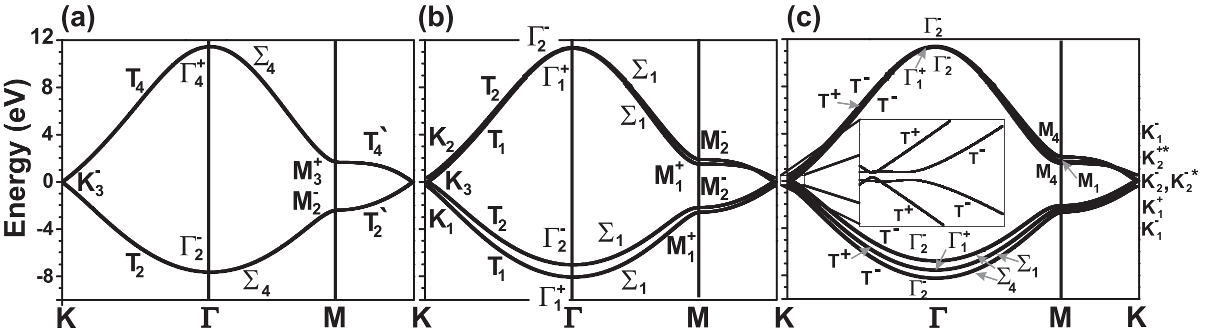

Figure 5.2: The electronic dispersion for the π electrons and the irreducible representations (Γ_π) for (a) monolayer, (b) bilayer and (c) trilayer graphene along the KΓMK directions. The calculation was done by M. H. D. Guimarães via pseudopotencial DFT [104] as implemented in the SIESTA program [105, 106].

degenerated at the K point (see Table 5.3 and Fig. 5.2(b)) and the other two have a gap of $2\gamma_1$, where γ_1 is the Slonczewski-Weiss-McClure parameter [1, 2] that have an experimental value of ~ 0.3 - 0.4eV [102, 107, 46].

Trilayer graphene in the ABA Bernal stacking (see Fig. 5.1(c,f)), belongs to the D_{3h} point group and Fig. 5.2(c) shows its electronic dispersion. The K point of trilayer is isomorphic to C_{3h}. In Tables 5.2 and 5.3, K_2^+ and K_2^{+*} are the two one-dimensional representations of the K_2^+ representation, where $*$ means the complex conjugate. The same happens for the K_2^- representation. The electron representations will be given by $\Gamma_\pi^K = K_1^+ + 2K_1^- + K_2^{+*} + K_2^- + K_2^{-*}$ for the K point and $\Gamma_\pi^{K'} = K_1^+ + 2K_1^- + K_2^+ + K_2^{-*} + K_2^-$ for K′ point. Although time reversion symmetry can imply degeneracies between complex conjugate representations in cyclic groups, in graphene the complex conjugation also takes K into K′ point and, consequently, there are no degenerated bands at the K (K′) point, in agreement with *tight-binding* calculations when including the γ_2 and γ_5 next-nearest-layer coupling parameters [56, 108]. This energy gap is also obtained from *ab initio* calculations (see the inset to Fig. 5.2 (c) and Ref. [109]).

It is worth to note that this work address the AB stacking. Some theoretical works have shown interesting behavior of the Dirac points for the case of ABC stacking [109, 110], where the inversion symmetry is present [110] and the valence and conduction bands can be degenerated near the K point [109, 110].

5.1.3 Gated mono and bilayer graphene

If the monolayer graphene is in the presence of a perpendicular electric field (gated graphene), the Fermi level changes. The presence of charge inhomogeneity caused by substrate and/or absorbed water can generate the same effect as verified in transport [8, 11] and Raman measurements [111], where the Dirac point is shifted from the neutrality point. In these cases, the π electrons loose the horizontal mirror plane and the inversion symmetry, and the system is isomorphic to the point group C_{6v}. The irreducible representations for the Γ_π for the gated graphene can be found in Table 5.4. The K point electrons still belong to the double-degenerated K_3 irreducible representation, and there is no gap opening at K point for a perfect perpendicular electric field effect.

The biased bilayer graphene have attracted a lot of attention recently because it is the only material known to have a tunable energy gap [21, 102, 20, 103, 22], promising for applications on devices and lasers with tunable energy. The mechanism behind this feature is based on applying an electric field perpendicular to the graphene layers, so that the two layers will be under inequivalent potentials. Then it is possible to open a gap at the K point, breaking the double degenerated K_3 irreducible representation into two one-dimensional irreducible representations. Since the biased bilayer graphene brakes the inversion center symmetry, the group of the wavevector at Γ for perfect perpendicular electric field is isomorphic to C_{3v}. Table 5.4 shows that the biased bilayer contains the two one-dimensional representations K_2 and K_2^* at the K point, and a gap opening is expected on the basis of symmetry arguments considering inequivalent layers.

The electric field does not affect the symmetries of the phonons. The representations for the $\Gamma_{lat.vib.}$ of the gated monolayer (or biased bilayer) are the same as the monolayer (or bilayer) in an isotropic medium, given in table 5.2.

5.2 Selection rules for electron-radiation interaction

The symmetry properties described in the previous section will now be applied to physical processes. In this section we discuss the selection rules for electron-radiation interaction in the dipole approximation, with emphasis on the high symmetry lines T and T′ in the electronic dispersion, where interesting phenomena

Table 5.4: The group of wavevector and its Γ_π representations for gated monolayer and biased bilayer graphene.

	Gated monolayer		**Biased Bilayer**	
	GWV	Γ_π	GWV	Γ_π
Γ	C_{6v}	$\Gamma_1 + \Gamma_4$	C_{3v}	$4\Gamma_1$
$\mathbf{K(K')}$	C_{3v}	K_3	C_3	$2K_1 + K_2 + K_2^*$
$\mathbf{M}$	C_{2v}	$M_1 + M_3$	C_{1v}	$4M_1$
$\mathbf{T(T')}$	C_{1v}	$T_1 + T_2$	C_1	$4T$
Σ	C_{1v}	$2\Sigma_1$	C_{1v}	$4\Sigma_1$
$\mathbf{u}$	C_1	$2u$	C_1	$4u$

occur.

In the dipole approximation, the absorption of light in a material is related to the wave functions of the electron states in the valence ($\psi^v(\mathbf{k})$) and conduction ($\psi^c(\mathbf{k})$) bands and the polarization of the incoming light ($\mathbf{P}$) by $W(\mathbf{k}) \propto |\mathbf{P} \cdot \langle \psi^c(\mathbf{k})|\nabla|\psi^v(\mathbf{k})\rangle|^2$ [76, 73]. Knowing the symmetry of the initial an final states, and the representation that generates the basis function of the light polarization vector (x, y or z), group theory can be used to compute when $W(\mathbf{k})$ is null or not. The results are summarized in Table 5.5 considering graphene layers laying in the (x,y) plane and light propagating along z. We will discuss in more details the results of Table 5.5 for bilayer and trilayer graphene, since these systems will be used in Section 5.4 to address the DRR scattering. In the case of graphene, the light absorption up to 3 eV occurs only at T, T′ and u points.

It is important to highlight some results given in Table 5.5. In the case of monolayer graphene on an isotropic medium, numerical calculations show an anisotropy in the optical absorption [73, 74, 75]. This anisotropy has indeed a symmetry basis, as clearly seen when analyzing the selection rules at the T line. Absorption by visible light has to couple T_2 and T_4 π electron symmetries (see Fig. 5.2(a)). For the T line direction along $\hat{y}$, the only allowed absorption is for light polarized along the $\hat{x}$ direction. For incident light polarization along the $\hat{y}$ direction, no absorption will occur along KΓ direction, giving rise to the optical absorption anisotropy on graphene [73, 74, 75]. Outside the high symmetry T line there is a non-zero probability of absorption and the anisotropy is obtained by defining orthogonal basis, as shown in Ref. [73].

When the monolayer graphene is on top of a substrate, with the influence of the environment changing the Fermi level, there will be no change in the selection rules for electron-radiation interaction. Along the T line, the π electrons are

Table 5.5: Selection rules for electron-radiation interaction with $\hat{x}$ and $\hat{y}$ light polarization in monolayer and N-layer graphene (see Fig. 5.1 (g) for $\hat{x}$ and $\hat{y}$ definition).

	BZ point	**polarization**	**W(k)**
monolayer	T	$x \in T_3$ $y \in T_1$	$T_2 \otimes T_3 \otimes T_4$ non null $T_2 \otimes T_1 \otimes T_4$ null
	u	$x, y \in u^+$	$u^- \otimes u^+ \otimes u^-$ non null
gated monolayer	T	$x \in T_2$ $y \in T_1$	$T_1 \otimes T_2 \otimes T_2$ non null $T_1 \otimes T_1 \otimes T_2$ null
	u	$x, y \in u$	$u \otimes u \otimes u$ non null
N-even	T	$x \in T_2$	$T_1 \otimes T_2 \otimes T_1$ null $T_1 \otimes T_2 \otimes T_2$ non null $T_2 \otimes T_2 \otimes T_2$ null
		$y \in T_1$	$T_1 \otimes T_1 \otimes T_1$ non null $T_1 \otimes T_1 \otimes T_2$ null $T_2 \otimes T_1 \otimes T_2$ non null
	u	$x, y \in u$	$u \otimes u \otimes u$ non null
biased bilayer	T	$x, y \in T$	$T \otimes T \otimes T$ non null
	u	$x, y \in u$	$u \otimes u \otimes u$ non null
N-odd	T	$x, y \in T^+$	$T^+ \otimes T^+ \otimes T^+$ non null $T^+ \otimes T^+ \otimes T^-$ null $T^- \otimes T^+ \otimes T^-$ non null
	u	$x, y \in u^+$	$u^+ \otimes u^+ \otimes u^+$ non null $u^+ \otimes u^+ \otimes u^-$ null $u^- \otimes u^+ \otimes u^-$ non null

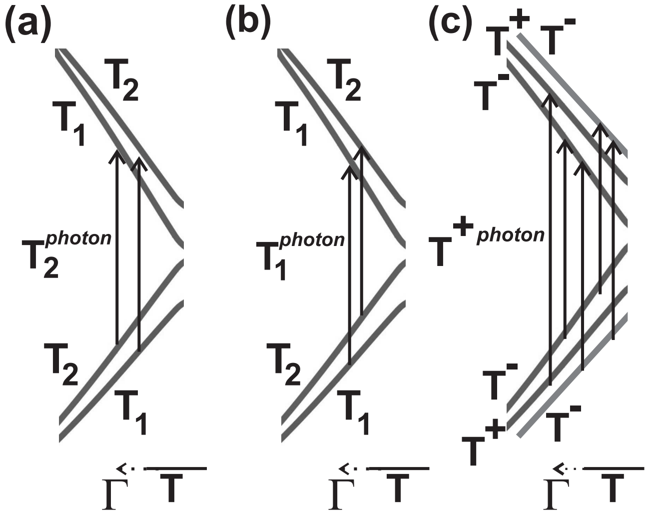

Figure 5.3: (a,b) Schematic electron dispersion of bilayer graphene along the KΓ direction showing the possible transition induced by (a) a photon with T_2 symmetry (x polarization) and (b) a T_1 photon (y polarization). (c) The electronic dispersion of trilayer graphene showing the five possible transitions induced by light absorption.

described by T_1 and T_2 representations, where T_2 and T_1 contain x and y basis function, respectively. Again there will be no absorption for y polarization along KΓ direction.

The bilayer graphene is composed by four electronic bands at the T line, belonging to two T_1 and two T_2 irreducible representations. The four possible transitions are illustrated in Fig. 5.3 (a,b). In this case both x and y polarized light can be absorbed. For the biased bilayer graphene, all electronic representations are the same, and it contains both x, y base functions for light polarizations. Thus, all the four transitions are allowed connecting all the four bands by the same light polarization, differently from the unbiased bilayer case where the light polarization selects the pair of bands that can be connected.

The trilayer graphene will have more possibilities for light induced transitions, since there are more possibilities between the three π and three π^* bands. Along T(T′) direction, there are two T^+ and four T^- bands giving raise to five possible transitions, as shown in Fig. 5.3 (c).

5.3 Selection rules for the first-order Raman scattering and infrared absorption processes

The first-order Raman scattering process is limited to phonons at the center of BZ (Γ point) due to momentum conservation requirement (phonon wavevector $q = 0$). In monolayer graphene the first-order Raman spectra is composed by the G band vibrational mode, which is doubly degenerated at the Γ point with Γ_6^+ symmetry. The Raman active modes depending on N (N>1) (without acoustic modes) are:

$$\Gamma^{\mathrm{Raman}} = N(\Gamma_3^+ + \Gamma_1^+), \text{ for N even}$$
$$\Gamma^{\mathrm{Raman}} = N\Gamma_3^+ + (N-1)(\Gamma_3^- + \Gamma_1^+), \text{ for N odd.}$$

For even number of layers the G band belongs to the Γ_3^+. There is a low frequency Γ_3^+ mode with frequency depending on the number of layers (35-53 cm^{-1})[112]. Two new Raman active modes near ~80 cm^{-1} and ~ 900 cm^{-1} appear with Γ_1^+ irreducible representations [113, 112]. For odd number of layers the G band is assigned as a combination of Γ_3^+ and Γ_3^- representations, also the smaller wavenumber component is active in Raman by a Γ_1^+ representation.

For monolayer graphene there is an infrared (IR) active mode belonging to the Γ_2^- representation, giving rise to an absorption near ~ 870 cm^{-1}. The IR active modes for N>1 are:

$$\Gamma^{\mathrm{IR}} = (N-1)\Gamma_2^- + (N-1)\Gamma_3^-, \text{ for N even}$$
$$\Gamma^{\mathrm{IR}} = N(\Gamma_3^+ + \Gamma_2^-), \text{ for N odd.}$$

For even number of layers the active modes belong to the Γ_2^- and Γ_3^- representations, the later one referring to the ~ 1590 cm^{-1} frequency vibration [113, 112]. The infrared active modes for odd layer number belong to Γ_2^- and Γ_3^+ which are also Raman active.

5.4 Electron scattering by $q \neq 0$ phonons and the Double resonance Raman scattering

The electron-phonon scattering (EPS) is calculated from the initial and final electron wave functions coupled by the phonon eigenvector [78, 64] using the phonon-induced deformation potential. Therefore, the selection rules of the EPS processes are obtained by the direct product of the symmetries of the initial and final electronic states and the symmetry of the phonon involved in the process. The allowed electron-phonon scattering processes for monolayer, gated monolayer, N-even, biased bilayer and N-odd, along the KΓ and KM directions (T and T′ lines, respectively) and at a generic u point are summarized in Table 5.6.

Table 5.6: Allowed processes for electron-phonon scattering for monolayer and N-layer graphene, along the T and T′ lines and at a generic u point, for each phonon symmetry.

	BZ point	**phonon**	**allowed scattering**
monolayer	T(T′)	T_1 T_3	$T_2 \rightarrow T_2$, $T_4 \rightarrow T_4$ $T_2 \rightarrow T_4$
	u	u^+	$u^- \rightarrow u^-$
gated monolayer	T(T′)	T_1 T_2	$T_1 \rightarrow T_1$, $T_2 \rightarrow T_2$ $T_1 \rightarrow T_2$
	u	u	$u \rightarrow u$
N-even	T(T′)	T_1 T_2	$T_1 \rightarrow T_1$, $T_2 \rightarrow T_2$ $T_1 \rightarrow T_2$
	u	u	$u \rightarrow u$
biased bilayer	T(T′)	T	$T \rightarrow T$
	u	u	$u \rightarrow u$
N-odd	T(T′)	T^+ T^-	$T^+ \rightarrow T^+$, $T^- \rightarrow T^-$ $T^+ \rightarrow T^-$
	u	u^+ u^-	$u^+ \rightarrow u^+$, $u^- \rightarrow u^-$ $u^+ \rightarrow u^-$

One example of explicit use of the electron-radiation and EPS selection rules is the double resonance Raman scattering process [84, 85], in which an electron in the conduction band is scattered by a phonon with wavevector outside the Γ point in an intervalley (connecting electronic states near the K and K′ points) or in an intravalley (connecting electronic state near the same K or K′ point) process. The G′ Raman band ($\sim$ 2700 cm^{-1}) comes from an intervalley process in which the electron is scattered by an in-plane transversal optic (iTO) phonon [79]. We will discuss in details the G′ scattering for monolayer, bilayer and trilayer graphene.

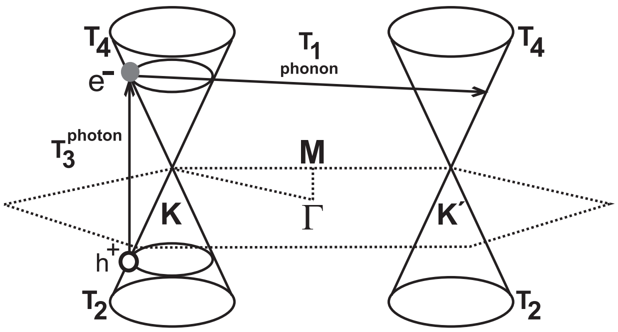

Figure 5.4: The most efficient DRR process in graphene showing the absorption of light with polarization symmetry T_3, followed by electron scattering by a phonon with T_1 symmetry.

For the monolayer graphene, a possible scattering is illustrate in Fig. 5.4. The iTO phonon at the KM (T′) direction presents a T_1 symmetry, which can only connect two electrons with the same symmetry. Many other similar scattering events are allowed by symmetry, involving electrons/holes in the KΓ (T) direction or at any general u point inside the circle defined by the T_3 photon energy. However, the matrix element has a strong angular dependence and the scattering is dominated by the T electrons, as discussed in Ref. [47]. Therefore, the G′ Raman band has only one peak, with full width at half maximum (FWHM) of $\sim$ 24 cm^{-1} (see Fig. 5.5 (a)) [38, 47]. For the graphene on top of a substrate, the same selection rules apply, and the expected number of G′ peaks is the same as for the isolated monolayer graphene in an isotropic medium.

For the bilayer graphene, the number of allowed DRR processes predicted by group theory will be larger, since both electronic and phonon branches are doubled. Along the T line, there is polarization dependence for the absorption linking different electronic bands, as discussed in section 5.2. For wavevectors in the range of visible light energy, the electron dispersion are almost linear, then optical anisotropy can be applied here as for monolayer graphene [93]. Now, for computing the number of resonant conditions involved in the DRR process, we are left with only two excited electronic bands with symmetries T_1 and T_2, which corresponds to Fig. 5.3 (a). The iTO phonons for bilayer graphene have T_1 and T_2 symmetries. For the electron scattering by a T_1 phonon, the allowed process are between K and K′ electronic bands with same symmetry ($T_1 \rightarrow T_1$ or $T_2 \rightarrow T_2$). The same happens with the electron scattering by a T_2 phonon, but it connects

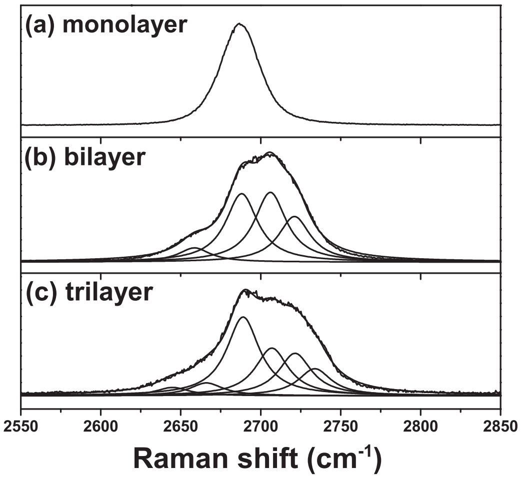

Figure 5.5: The measured Raman spectra of the G′ band of a (a) monolayer (b) bilayer and (c) trilayer graphene. The samples were made by exfoliating graphite on top of a 100 nm silicon oxide substrate using 2.41 eV laser energy. The G′ band for monolayer, bilayer and trilayer graphene were fitted with 1, 4 and 6 Lorentzians, respectively, with a FWHM of 24 cm^{-1}.

conduction bands of different symmetries, i.e. $T_1 \rightleftarrows T_2$. This gives rise to four possible DRR processes, as shown in Fig. 5.6 [38]. The Raman spectra can then be used to differentiate mono and bilayer graphene (see Fig. 5.5)[38, 39, 40].

In the case of biased bilayer graphene, there are no selection rules involving different photon polarizations. The biased bilayer can have photon absorption linking all valence and conduction bands. This leads to eight possible transitions considering EPS selection rules for T_1 and T_2 phonons.

For the trilayer graphene, the DRR process will have again more contributions because each phonon and electron band will be split in three levels. Along the T line, there are five possibilities linking the electronic bands between the K and K′ points with a T^+ phonon, and four possibilities for the T^- phonon. The total number of DRR process predicted by group theory will be fifteen. However, the FWHM is large when compared to the energy splitting between the G′ Raman peaks, and when one makes measurements of the G′ Raman band in trilayer graphene, these fifteen peaks cannot be distinguished, as illustrated in Fig. 5.5 (c). Similar problem should happen for N≥4.

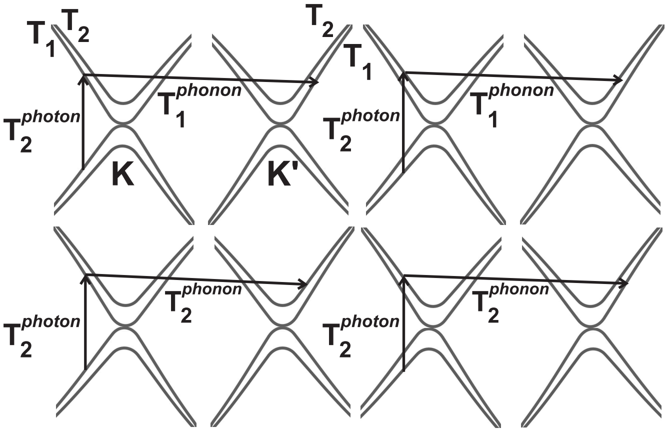

Figure 5.6: The four allowed DRR processes in bilayer graphene, taking into account the optical anisotropy.

5.5 Summary

In this chapter we analyzed the symmetry aspects related to electrons and phonons at each point in the BZ of graphene, depending on the number of layers. The symmetry aspects can be generalized to any value of N, differing for N even or odd. For monolayer and bilayer we consider both an isotropic and an anisotropic medium. We derived the selection rules for electron-radiation and electron-phonon interactions. Some specific findings can be remarked:

• For the monolayer graphene, the predicted optical anisotropy [73] comes out directly from group theory analysis. The electron-phonon scattering process is allowed by symmetry at any generic point (u) in the Dirac cone, and the observation of a single Lorentzian in the G$'$ Raman band comes from a strong anisotropy in the electron-phonon matrix element [47].

• The gated graphene has lower symmetry, but the optical anisotropy is still present, and for the DRR process, the symmetry considerations are the same as graphene on an isotropic medium.

• In the case of bilayer graphene, the optical anisotropy is also present and there are four dominant processes in the DRR. This number increases to eight on biased bilayer.

• In trilayer graphene, the number of possible DRR processes is fifteen. However, the 15 processes are not distinguishable and the G′ Raman band can be nicely fit with 6 Lorentzians. Similar situation is expected for larger number of layers.

Chapter 6

Resonance Raman spectroscopy of graphene

Resonance Raman scattering (RRS) has been widely use to probe the electronic and phonons structure of carbon materials like carbon nanotubes [114], graphite [32], diamond-like carbon [115] and linear carbon chains [116]. Also the double resonance Raman (DRR) model and its second order G' band provide rich information about the energy and momentum of the participating electrons and phonons. In this section we review the combination of RRS and DRR processes to probe information about phonons and electrons in monolayer and bilayer graphene.

From the DRR model (see §3.2) we have a set of two coupled quantities, that is, the electrons and phonons and their dispersion relations. From the knowledge of one of these quantities and information coming from the experimental Raman band originating from a specific double Resonance scattering process (for example, the phonon energies and their dispersion), it is possible to get the other quantity (which, for this example, would be information about the electronic structure). By changing the laser excitation energy, different points in momentum space for the electronic and phonon dispersion are probed, and in this way it is possible to map the phonon or electronic dispersion relations by this method. Some basic fundamental concepts related to this method are discussed in §3.2.

6.1 Probing phonons in monolayer graphene

We begin our discussion here with monolayer graphene, which represents the ideal system for calculating the phonon dispersion relations for a variety of carbon structures, and there are several different phonon dispersion models in the literature for describing $\omega(q)$ for graphite and other sp^2 carbons [117, 118, 119, 120, 121, 59, 66, 122]. In many cases, these models contradict each other in terms of the slopes and positions of the phonon branches near the Dirac point (the K point) and this is in part due to the Kohn anomaly [66]. Also different experimental techniques like neutron scattering [123], electron energy-loss spectroscopy [124, 125, 126], inelastic X-ray scattering [59, 127], and DRR scattering [85, 79], have been applied to characterize the phonon dispersion. Here, we show that by measuring the Raman spectra of two second-order Raman features with different laser energies, it is possible to obtain experimentally the longitudinal acoustic (LA) and the in-plane transverse optical (iTO) phonon dispersions of monolayer graphene near the Dirac point [47]. We also compare the results thus obtained with the corresponding results for turbostratic graphite and for different phonon dispersion models in the literature.

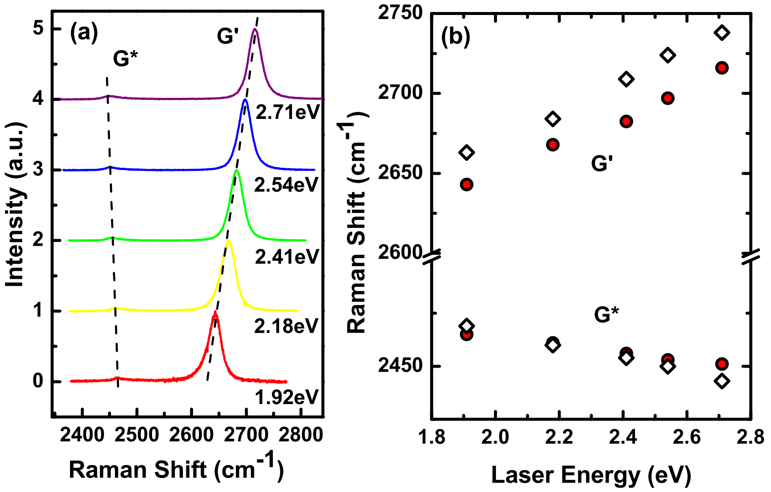

Figure 6.1: (a) Raman spectra of the G' and the G^* bands of monolayer graphene for 1.92, 2.18, 2.41, 2.54 and 2.71 laser excitation energy. (b) Dependence of $\omega_{G'}$ and ω_{G^*} on E_{laser}. The circles correspond to the graphene data and the lozenges correspond to turbostratic graphite.

Figure 6.1(a) shows the Raman spectra in the region of the G^* (~ 2450 cm^{-1}) and G' (~ 2700 cm^{-1}) bands with different laser excitation energies. As shown in §3.2, the G' bands come from an inter-valley DRR process involving an electron with wave vector $\boldsymbol{k}$ in the vicinity of the K or K' point and two iTO phonons with wave vectors $\boldsymbol{q}\approx 2\boldsymbol{k}$, where both $\boldsymbol{k}$ and $\boldsymbol{q}$ are measured from the K point. The G^* band can also be explained by the DRR model with an inter-valley process but involving one iTO and one LA phonon [79] as discussed below.

Figure 6.1(b) shows the G' and G^* frequencies as a function of laser energy for graphene and turbostratic graphite. The G' band exhibits a highly dispersive behavior, with a slope of 88 cm^{-1}/eV for monolayer graphene and 95 cm^{-1}/eV for turbostratic graphite. The G^* band, exhibits a less pronounced dispersion for both materials. In contrast, ω_{G^*} *decreases* with laser energy by about -18 cm^{-1}/eV for monolayer graphene and by about -31 cm^{-1}/eV for turbostratic graphite.[47]

To analyze the experimental data from Fig. 6.1 (b), we first introduce the linear dispersion of a graphene monolayer by noting that the electron energy is given by $E(k) = \hbar v_F k$, where v_F is the Fermi velocity and k is the electron wave vector measured with respect to the K point. Thus the DRR conditions are given by (See Chapter 3) Sec. 3.2:

$$\omega_L = 2v_F k \tag{6.1}$$

$$\omega_{ph} = v_F(k - k') \tag{6.2}$$

$$q = k + k', \tag{6.3}$$

where ω_L and ω_{ph} are the laser and phonon frequencies and k' is the scattered electron wave vector near the K' point.

From the measured frequencies ω_{G^*} and $\omega_{G'}$ shown in Fig. 6.1, we can obtain the experimental values for the LA and iTO phonons near the Dirac point. The iTO frequency can be obtained from $\omega_{G'}/2$, and the LA frequency (ω_{LA}) is obtained from subtracting the iTO frequency from the G^* band frequency:

$$\omega_{iTO}(q) = \omega_{G'}(q)/2 \tag{6.4}$$

$$\omega_{LA}(q) = \omega_{G^*}(q) - \omega_{G'}(q)/2. \tag{6.5}$$

So, using Eqs. (6.1-3) we obtain the phonon wave vector q observed for each laser energy and, with the results of Eqs. (6.4 and 6.5), the dispersion of ω_{LA} and ω_{iTO} phonons can be plotted.

As discussed above, we can only determine the phonon velocities in a double resonance Raman experiment as a function of the Fermi velocity v_F for the electrons near the Dirac point. In order to plot experimental results for the phonon dispersion relation, we need to consider a specific value for the Fermi velocity. Figure 6.2 shows experimental data for ω_{iTO} [Fig. 6.2(a)] and ω_{LA} [Fig. 6.2(b)] for monolayer graphene as a function of the phonon wave vector q considering three different values of v_F: 0.84 $\times 10^6$ m/s (black circles), 1.0 $\times 10^6$ m/s (white circles), and 1.1×10^6 m/s (gray circles), which correspond to the values of the nearest-neighbor tight-binding overlap energy γ_0 of 2.6, 3.1 and 3.4 eV, respectively [86]. Four different phonon dispersion models are also shown in Fig. 6.2 for the iTO and the LA branches. These models correspond to the first-principles calculations by Maultzsch *et al.* [59] (dashed curves) and Dubay *et al.* [120] (dotted curves), the force constant model by Popov and Lambin [122] (continuous curves) and the bond charge model reported by Benedek and Onida [118] (dash dotted curve). The best agreement between the experimental and theoretical data is given when we consider a Fermi velocity of 1.0 $\times 10^6$ m/s and the theoretical model for the iTO phonon dispersion by Popov and Lambin [122], which nicely describes the Kohn anomaly as observed experimentally. Figure 6.2(c) shows the phonon dispersion curve around the K point with v_F=1.0 $\times 10^6$ m/s, comparing the different phonon models, as well as with the measured results for turbostratic graphite and with different experimental X-ray diffraction data for graphite.[47, 59]

Another important quantity that can be extracted using this approach is the phonon velocity for both phonon branches (v_{TO} and v_{LA}). By deriving ω_{ph} with respect to q and considering the DRR conditions shown in Eqs. (1-3), we obtain the following expressions that relate the phonon velocities with the Fermi velocity v_F for electrons:

$$v_{TO} = (d\omega_{G'}/d\omega_l)v_F/2 \tag{6.6}$$

$$v_{LA} = (d\omega_{G^*}/d\omega_l - \tfrac{1}{2}d\omega_{G'}/d\omega_l)v_F \tag{6.7}$$

By using the experimental laser frequency ω_l dependence of ω_{G^*} and $\omega_{G'}$ shown in Fig. 6.1 (b), we obtain the following values for the LA and iTO velocities near the Dirac point of monolayer graphene: $v_{LA} = 7.70\times 10^{-3}v_F$ and $v_{TO} = 5.47\times 10^{-3}v_F$. The corresponding values found for turbostratic graphite are: $v_{LA} = 9.82\times 10^{-3}v_F$

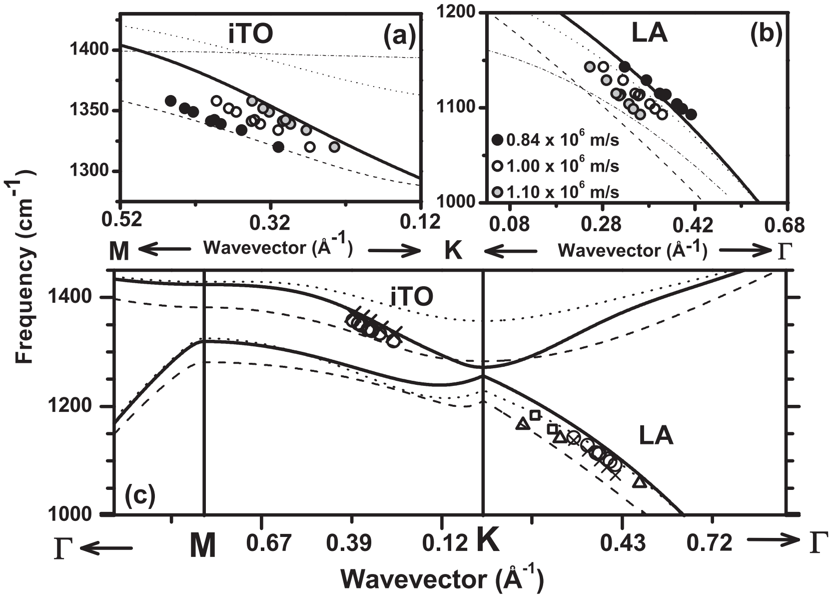

Figure 6.2: (a) Experimental data obtained from the DDR scattering for the (a) iTO phonons and (b) the LA phonons in monolayer graphene, considering three different values for the Fermi velocity v_F, and theoretical phonon dispersion models by Maultzsch *et al.* [59] (dashed curves), Dubay *et al.* [120] (dotted curves), Popov and Lambin [122] (continuous curves) and Benedek and Onida [118] (dash dotted curve). (c) Experimental phonon frequencies obtained from DR Raman scattering for graphene (circles) and turbostratic graphite (*xxx*) and inelastic x-ray diffraction data by Maultzsch *et al.* [59] (triangles) and Mohr *et al.* [127] (squares).

and $v_{TO} = 5.96 \times 10^{-3} v_F$ [47].

6.2 Probing the electronic structure of bilayer graphene

We now turn to the electronic properties of bilayer graphene as probed by RRS. Bilayer graphene has a richer G' band spectrum, because of its special electronic structure consisting of two conduction and two valence bands (see Fig. 3.14). From the DRR process in bilayer graphene, it is possible to distinguish four Lorentzians in the Raman spectra for each laser line [38]. Figure 6.3 (a) and (b) compares a spectra recorded with 2.18 eV laser energy, where the fitting was done with three and four Lorentzians. Although Fig. 6.3(a) shows that the FWHM is increased to

29 cm^{-1} in bilayer graphene, which is larger than that in monolayer graphene, 24 cm^{-1}, it is clear from the fit that four peaks are needed to describe the G' band of bilayer graphene, as shown in Fig. 6.3(b) [46], and discussed in §3.3. The fit with three peaks would be appropriate if the valence and conduction bands were mirror bands. The asymmetry between the valence and conduction bands indicates some difference in the band parameters for the valence and conduction bands.

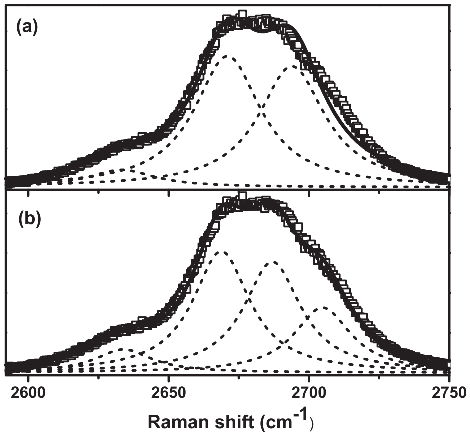

Figure 6.3: Fitting the measured spectra of the G' band at 2.18 eV laser excitation energy with (a) three Lorentzians with an FWHM of 29 cm^{-1} and with (b) four Lorentzians with an FWHM of 24 cm^{-1}.

By fitting each one of the laser energies with four Lorentzians with a FWHM of 24 cm^{-1}, we can plot the position of each peak as a function of laser energy. Figure 6.4(a) shows the dispersion of each one of the four peaks that comprise the G' band as a function of laser energy. Each one of the DRR processes that gives rise to one of the G' peaks is labeled as P_{ij} $(i, j = 1, 2)$, in Fig. 6.4(a) and the related process is depicted from Fig. 6.4(b) to (e). Since the iTO phonon along the KM direction increases its frequency with increasing its wave vector q, the highest frequency of the G' peak for a given E_{laser} energy is associated with the P_{11} process, which has the largest wave vector (q_{11}). The smallest wave vector q_{22} is associated with the process P_{22}, which gives rise to the lowest frequency peak of the G' band. The two intermediate peaks of the G' band are associated with processes P_{12} and P_{21} [46].

Now we apply the DRR model to relate the electronic and phonon dispersion of bilayer graphene with the experimental dependence of the G' band energy as a function of laser energy. According to the DRR process for bilayer graphene (see §3.3) an electron in a P_{ij} process with wave vector k_i is resonantly excited from

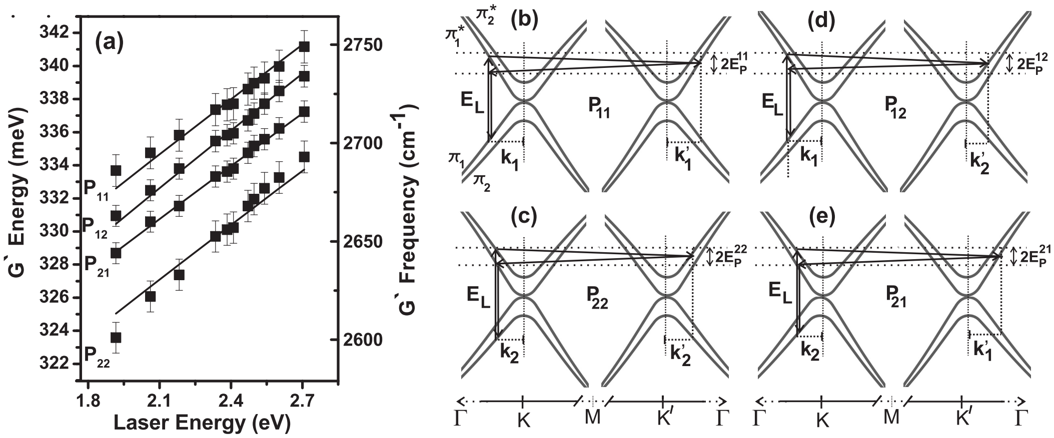

Figure 6.4: (a) The position of the four peaks that comprise the G' band of bilayer graphene as a function of laser energy. The solid lines are the theoretical fitting (see in the text). On the right is the schematic view of the electron dispersion of the bilayer graphene near the K and K' points showing both π_1 and π_2 bands. The four DRR processes are indicated: (b) process P_{11}, (c) process P_{22}, (d) process P_{12}, and (e) process P_{21}. The wave vectors of the electrons (k and k') involved in each of these four DRR processes are indicated by the respective arrows.

the valence band π_i to the conduction band π_i^* by absorbing a photon with energy E_L. This electron is then resonantly scattered to a state with wave vector k_j' by emitting a phonon with momentum q_{ij} and energy E_p^{ij}. Finally, the electron is scattered back to state k_i by emitting a second phonon, and it recombines with a hole producing a scattered photon with an energy $E_S = E_L - 2E_p^{ij}$. The phonon wave vector q_{ij}, measured from the K point and along the KM direction, is given by $q_{ij} = k_i + k_j'$. As discussed in §3.3, the P_{11} and P_{22} processes are related to a phonon with T_1 symmetry and the other two processes to a phonon with T_2 phonon symmetry.

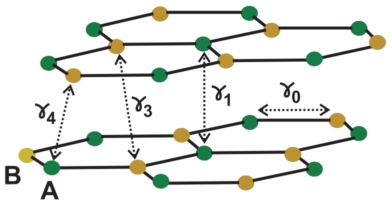

Figure 6.5: Atomic structure of bilayer graphene, where the overlap γ parameters are shown with the respective pair of atoms for each γ_i interaction.

The electronic structure of bilayer graphene can be described by the phenomenological Slonczewski-Weiss-McClure (SWM) model [1, 32, 2]. Since the unit cell of bilayer graphene with the Bernal AB stacking structure is the same as for graphite which has the same stacking structure, we can denote the electronic spectrum of bilayer graphene in terms of a model closely related to the SWM model for graphite, by determining the parameters γ_0, γ_1, γ_3 and γ_4, that are associated with overlap and transfer integrals calculated for nearest neighbors atoms. The pair of atoms associated with these parameters are indicated in the atomic structure of bilayer graphene shown in Fig. 6.5. Along the $K-\Gamma$ direction we can replace σ by $\gamma_0\big[2\cos(2\pi/3-ka\sqrt{3}/2)+1\big]$ in McClure's expressions. Here k is measured from the K point and $a=1.42$ is the in-plane nearest neighbor carbon distance. Since there is no k_z-dependence we may set the following parameters in McClure's expressions at $\Gamma=1$ and $\gamma_2=\gamma_5=0$ (γ_2 and γ_5 correspond to 3^{rd} layer interactions in graphite). With these simplifications to the McClure model, the electronic bands in bilayer graphene can be described as [46, 56]:

$$\begin{aligned}
E_{\pi_2} &= (-\gamma_1 - v_3\sigma - \xi_+)/2, && (6.8)\\
E_{\pi_1} &= (\gamma_1 + v_3\sigma - \xi_-)/2, && (6.9)\\
E_{\pi_1^*} &= (-\gamma_1 - v_3\sigma + \xi_+)/2, && (6.10)\\
E_{\pi_2^*} &= (\gamma_1 + v_3\sigma + \xi_-)/2, && (6.11)
\end{aligned}$$

where

$$\xi_\pm = \sqrt{(\gamma_1 - v_3\sigma)^2 + 4(1\pm v_4)^2\sigma^2}, \tag{6.12}$$

and $v_j \equiv \gamma_j/\gamma_0$.

Applying the DRR conditions we have:

$$\begin{aligned}
E_L &= E_{\pi_i^*}(k_i) - E_{\pi_i}(k_i) && (6.13)\\
E_p^{ij}(k_i + k_j') &= E_{\pi_i^*}(k_i) - E_{\pi_j^*}(k_j'). && (6.14)
\end{aligned}$$

Equation 6.1 determine the initial k_i electron wave vector as a function of the band parameters. Assuming that the iTO phonon dispersion is linear in the measured energy range, we have $E_p^{ij}(k_i+k_j')=[A+B(k_i+k_j')]$. Then Eq. 3.14

uniquely determine the scattered k'_j electron wave vector, and $E_p^{ij}(k_i + k'_j)$ can be computed for each one of the P_{ij} processes for each laser excitation energy. By making a least squares fit of the experimental data to the above equations, it is possible to find the best set of electronic and phonon parameters that fit the experimental data. Figure 6.4(a) shows the experimental data (symbols) with the theoretical model (solid lines) [46]. Figure 6.6 also compares the SWM model including (a) only γ_0 and γ_1, (b) only γ_0, γ_1 and γ_3 and (c) all γ_0, γ_1, γ_3 and γ_4 parameters [46]. When $\gamma_3 = \gamma_4 = 0$, the two inner DRR process become degenerate [Fig. 6.6(a)]. By setting $\gamma_3 \neq 0$ and $\gamma_4 = 0$ [Fig. 6.6(b)], the trigonal warping effect [32] is included and this degeneracy is broken, but the calculated energy separation for the P_{12} and P_{21} is still too small to account for the experimental observations. In Fig. 6.6(c) where $\gamma_3 \neq 0$ and $\gamma_4 \neq 0$, the fit with the experimental data is successful. The γ_4 in the SWM model is responsible for the difference between the electron and hole effective masses [32]. Therefore, the P_{12} and P_{21} processes are associated with phonons with different momenta that participate in these scattering mechanisms revealing an electron-hole asymmetry in bilayer graphene. Table 6.1 summarizes the tight binding γ values for bilayer graphene, as compared with the graphite values in the literature. Also the results for two linear phonon dispersions found in the fitting procedure are shown in Table 6.2.

Table 6.1: Experimental SWM parameters (in eV) for the electronic band structure of bilayer graphene from Fig. 6.4. The parameters for graphite are taken from Refs. [128, 32].

	γ_0	γ_1	γ_2	γ_3	γ_4	γ_5	$\gamma_6 = \Delta$
Bilayer graphene	2.9	0.30	n/a	0.10	0.12	n/a	n/a
Graphite	3.16	0.39	-0.02	0.315	0.044	0.038	0.008

Table 6.2: Values obtained for the G' band phonon dispersion for bilayer graphene from Fig. 6.4(a) for the two iTO phonon branches of bilayer graphene near the K point, where $E_p^{ii}=A_{ii}+B_{ii}$q corresponds to the P_{11} and P_{22} processes and $E_p^{ij}=A_{ij}+B_{ij}$q to the P_{12} and P_{21} processes.

A_{ii}	B_{ii}	A_{ij}	B_{ij}
153.7 (meV)	38.5 (meV Å)	154.0 (meV)	38.8 (meV Å)
1238 (cm^{-1})	310 (cm^{-1} Å)	1241 (cm^{-1})	313 (cm^{-1} Å)

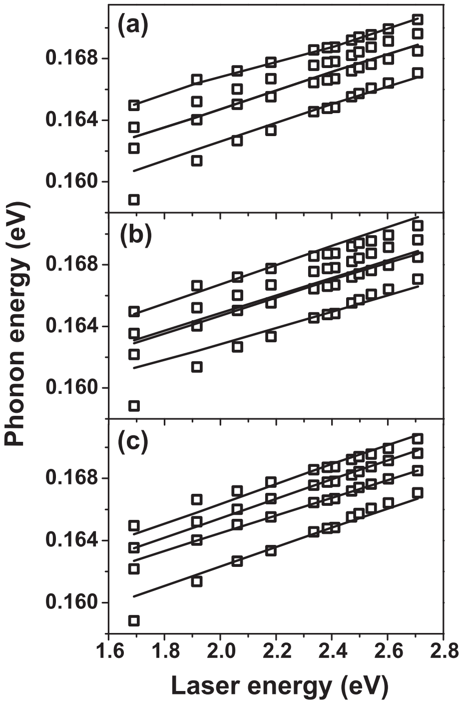

Figure 6.6: Experimental phonon energies (open squares) derived from the G' band as a function of laser excitation energy and the fitted curves (full lines) using (a) $\gamma_3 = \gamma_4 = 0$, (b) $\gamma_3 \neq 0$ and $\gamma_4 = 0$ and (c) $\gamma_3 \neq 0$ and $\gamma_4 \neq 0$. (see Table 6.2).

6.3 Summary

In this chapter we summarized how the combination of the RRS and DRR model can give important knowledge about the electronic and phonon structure in graphene materials. For monolayer graphene [47], the phonon structure of the iTO and LA phonon modes near the Dirac point were probed by the use of the selection rules of DRR and the combination with different laser excitation energies. For bilayer graphene [46], using a tight binding model related to graphite, the corresponding band parameters were obtained and the results reveal electron-hole asymmetry. The comparison of 2-LG to graphite is not expected to yield the same band parameters because the unit cell for bilayer graphene has empty space bounding the exteriors of the upper and lower layers while graphite has similar unit cells, to form a 3D lattice of these unit cells. The graphite structure has a k_z dependence of the dispersion relations, which is absent in bilayer graphene.

CHAPTER 7

Electron-phonon interactions in bilayer graphene

7.1 Introduction

The interaction of electrons and phonons is a fundamental issue for understanding the physics of graphene, resulting in the renormalization of phonon energy and the break-down of the adiabatic (Born-Oppenheimer) approximation [66, 41, 42, 43] as discussed in Chapter 2. Although many new physical insights about the electron-phonon interaction were found in monolayer graphene [41, 42, 43, 44, 45], the bilayer graphene is a unique system to study distinct couplings between electrons and phonons that have different symmetries [68]. Here we show that the application of a gate voltage in bilayer graphene splits the symmetric and anti-symmetric optical phonon components, confirming a recent theoretical prediction for the distinct interactions of these phonons with intraband and interband electron-hole pairs [68]. This result is specially relevant since the development of bilayer graphene devices with tunable gap depends on the detailed understanding of the interaction between electrons and phonons in this material [13, 103, 23].

The zone center E_{2g} phonon mode of monolayer graphene, which gives rise to the Raman G-band around 1580 cm^{-1}, exhibits a very strong coupling with electron-hole pairs. This interaction renormalizes the phonon energy $\hbar\omega_0$, giving rise to the so-called Kohn anomaly [66]. Moreover, theoretical models have predicted an interesting behavior for the phonon energy when the Fermi level ε_F is changed by varying the electron or hole concentration: the phonon energy softens logarithmically for values of the chemical potential smaller than half of the phonon energy, and it hardens otherwise. This hardening is ascribed to the suppression of the interaction between phonons and electron-hole pairs for $|\Delta\varepsilon_F| > \hbar\omega_0/2$. Besides this, an increase in either electron or hole density increases the phonon lifetime [43, 41, 42, 44, 45] due to the inhibition of the process of phonon decay into electron-hole pairs, thus reducing the G-band linewidth. Recent Raman studies of monolayer graphene have confirmed the theoretical prediction concerning the hardening and narrowing of the the G-band, by doping the sample with electrons or holes [43, 45, 44].

In the case of bilayer graphene, the E_{2g} phonon mode splits into two components, associated with the symmetric (S) and anti-symmetric (AS) displacements of the atoms in the two layers. Moreover, due to the splitting of the π and π^* bands in this material, phonons can couple with electron-hole pairs produced in interband or intraband transitions. T. Ando [68] calculated recently the self-energy of the S and AS phonons for varying Fermi energies and predicted the hardening and softening of the S and AS phonons, respectively, induced by electron or hole doping. In this work we present experimental results that confirm the theoretical prediction by T. Ando [68], thus showing that the G-band of bilayer graphene has indeed two components which exhibit opposite dependence as the Fermi level is tuned.

7.2 Results and discussion

Figure 7.1(a) shows an optical microscope image of the bilayer graphene device obtained by exfoliating bulk graphite on a 300 nm thickness SiO_2 layer on the top of a heavily p doped Si substrate. An electrical contact was made by soldering an indium micro wire directly on the top of the flake [129]. Charge carriers were induced in the sample by applying a gate voltage V_g to the Si substrate with respect to the graphene contact. The Raman measurements were carried out at room temperature using a triple Dilor XY spectrometer with a resolution smaller than 1 cm^{-1}, an 80x objective with spot size of ~ 1 μm and the 2.41 eV laser excitation with 1 mW power. The number of layers in our graphene sample was determined by analyzing the shape of the G′ (or 2D) band around ~ 2700 cm^{-1} [Fig. 7.1(b)], which is composed of four peaks and exhibits a typical shape of a bilayer graphene [38, 39, 40, 46].

Figure 7.1(c) shows the Raman spectra taken at different values of V_g. We

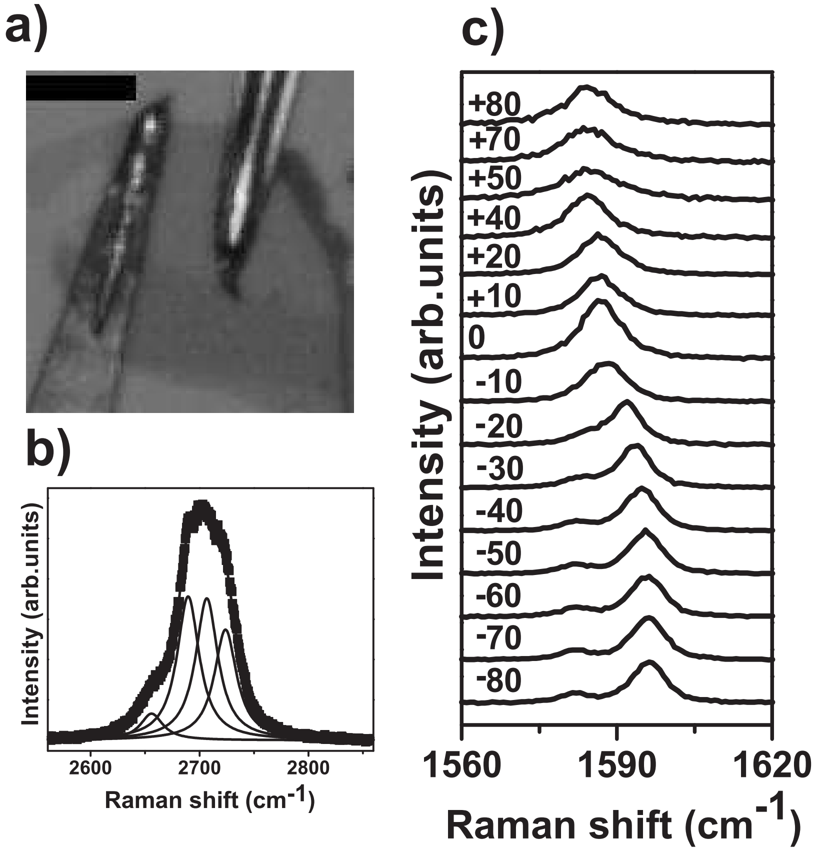

Figure 7.1: (a) Optical microscope image of gated graphene bilayer sample (the scale bar is 15 μm). (b) Raman spectrum of the G′ band of bilayer graphene. (c) Raman spectrum of the G band for different values of V$_g$.

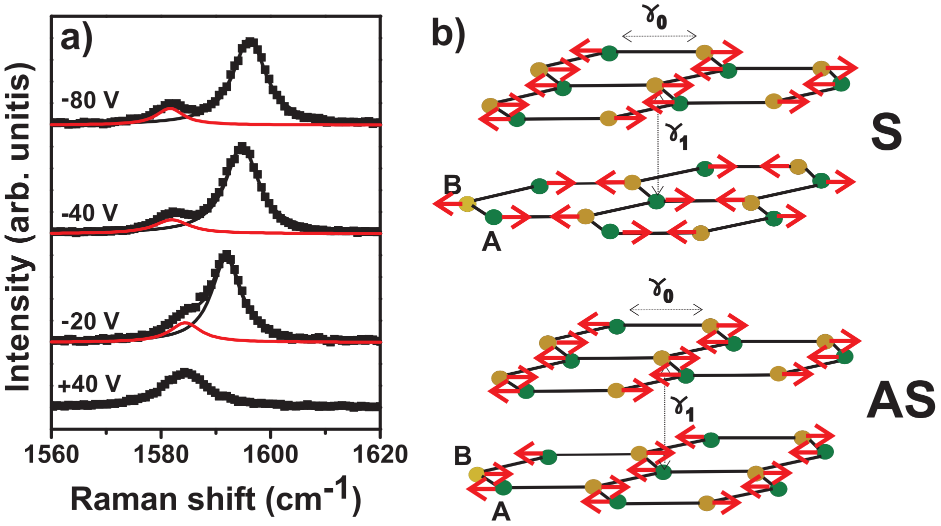

Figure 7.2: (a) Raman G-band of the bilayer graphene for -80 V, -40 V, -20 V and +40 V gate voltages . Two Lorentzian curves are needed to fit the G-band for -80 V, -40 V and -20 V. (b) Displacement of the atoms for the S and AS highest energy phonon modes in the Γ point of bilayer graphene.

observe that both the position and the shape of the G-band depend on V_g, in agreement with previous Raman studies of gated bilayer graphene [52, 54]. However, in our experiment we were not able to observe the initial softening of the G-band for $|\varepsilon_F| < \hbar\omega_G/2$, as reported by Yan et al. [52]. This result can be explained by the presence of a larger non-homogeneous charge distribution in our sample and by the fact that our experiment was done at room temperature.

Figure 7.2(a) shows the fittings of the Raman G-band of the bilayer graphene device for different values of V_g. The G-bands observed in the spectra taken at V_g equals to -80 V, -40 V and -20 V clearly exhibit two peaks. All spectra taken at positive values of gate voltage could be fitted by a single Lorentzian.

Figures 7.3(a) and 7.3(b) show the relative shift (with respect to G-band position in the + 50 V spectrum) and the full width at half maximum (FWHM) of the Lorentzians that fit the G-band as a function of the applied gate voltage, respectively. Notice that the frequency of the high energy component increases with decreasing values of V_g, whereas the opposite behavior is observed for the low energy component. Figure 7.3(b) shows that the FWHM exhibits a maximum for $V_g = +50$ V spectrum, and it clearly decreases with decreasing values of V_g.

Let us discuss the origin of the two peaks that compose the G-band shown in Fig. 7.2(a). The bilayer graphene is formed by two graphene layers in the AB Bernal stacking, where the point group at Γ point is D_{3d}. The phonon branch associated with the E_{2g} mode of monolayer graphene gives rise to two branches for bilayer graphene, one symmetric (S) and other anti-symmetric (AS) components (in-phase and out-of-phase displacements of the atoms in the two layers), which are represented at Fig. 7.2(b). At the center of the Brillouin zone (Γ point), the S and AS vibrations belong to the two doubly degenerated representations E_g and E_u, respectively. The anti-symmetric E_u mode is not Raman active since the D_{3d} group is centro-symmetric. However, if the inversion symmetry operation of the bilayer graphene is broken, the system is described by the C_{3v} point group at the Γ point. In this case, both the S and the AS modes belong to the E representation, and are Raman active.

The inversion symmetry breaking can be due to the different materials that the top and bottom graphene layers of our device are exposed to and/or to a non-homogeneous doping of the top and bottom layers. The non-equivalence between the top and bottom layers decreases the symmetry, making the anti-symmetric mode active in the Raman spectra, explaining thus the two components of the G-band. The energy separation between the S and AS components is negligible when the Fermi level is close to the Dirac point, and this can be seen in the spectrum taken at + 40 gate voltage in Fig. 7.1(b). However, the doping with electrons or holes induces a measurable energy splitting for those components, as shown in the spectra between -20 V to - 80 V in Fig. 7.1(b).

One could argue that the observed splitting of the G band is related to symmetric mode coming from the top and bottom layers, in the case of a non-homogeneous doping of the two layers. However, this interpretation has serious drawbacks in the present case. Notice that the low energy component of the G-band is about five times less intense than the higher energy one. Considering that the transmitance of visible light in monolayer graphene is about 97.7% [97], the contributions of the symmetric mode from the upper and bottom layers for the Raman scattering are expected to be almost the same. Furthermore, our results show that the energy of the low energy component decreases when the Fermi level is changed. This result would not be expected if one associates the lower energy Raman peak with the symmetric mode of the bilayer graphene bottom layer. We stress the fact that the splitting of the G-band was not reported in the two recent studies of gated bilayer graphene devices [52, 54], despite the fact that the G-band observed in reference

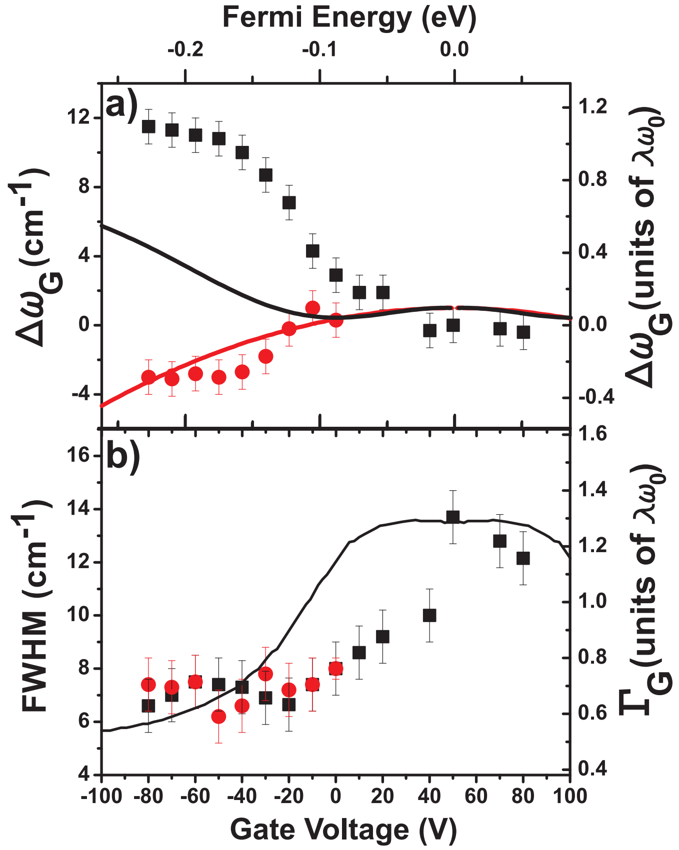

Figure 7.3: (a) The black squares and red circles correspond to the relative shift ($\Delta\omega_G$) of the S and AS components of the G band, respectively, with respect to the position in the +50 V spectrum, as a function of the applied gate voltage (bottom scale). The solid curves corresponds to the theoretical prediction for the relative G-band shift [68] in units of $\lambda\omega_0$ as a function of the Fermi energy (top scale). (b) The black squares and red circles correspond to the FWHM of the S and AS components of the G-band, respectively, and the solid curve corresponds to the theoretical prediction for the symmetric phonon mode [68].

[52] is clearly asymmetric. Possibly, our observation of this splitting is due to the characteristic of our device which leads to the inversion symmetry breaking and allows the observation of the non-active Raman AS vibration.

In order to discuss the phonon renormalization effect in bilayer graphene, we must consider the selection rules for the interaction of the S and AS phonons with the interbands or intrabands electron-hole pairs. The band structure of bilayer graphene near the K point shown in Figure 7.4 consists of four parabolic bands, two of them touch each other at the K point, and the other two bands separated by $2\gamma_1$, where $\gamma_1 \sim 0.35$ eV. The electron-phonon interaction in bilayer graphene is described by a 2x2 matrix for each phonon symmetry, where each matrix element gives the contribution of electron-hole pairs involving different electronic sub-bands [68]. For the S phonon mode, all matrix elements are different from zero, and this phonon can interact with both interband or intraband electron-hole pairs, as shown in Figure 7.4(a), giving rise to the phonon energy renormalization (Kohn anomaly). However, for the AS phonon mode, the diagonal terms of the matrix are null, showing that there is no coupling between AS phonons and interband electron-hole pairs. Therefore, no Kohn anomaly is expected for the antisymmetric phonon mode when the Fermi level is at the Dirac point.

However, if the Fermi energy is changed [for instance, $\varepsilon_F < 0$ as shown in Fig. 7.4(b)], intraband electron-hole pairs can be produced by phonons. Now, the AS phonons have also their energies renormalized, giving rise to the Kohn anomaly. Notice that as the energy separation between the π_1 and π_2 bands ($\gamma_1 \sim 0.35$ eV) is larger than the G band energy (~ 0.2 eV), the electron-hole pairs creation by those phonons is a virtual process. Therefore, we expect the dependence of the shift of the anti-symmetric mode with Fermi energy to be smoother than that of the symmetric mode. A similar result has been recently observed in gated semiconducting carbon nanotubes [69] which have the band gap larger than the phonon energy.

In order to explain our experimental results, we have also plotted in Figs. 7.3 (a) and (b) frequency shift and broadening (FWHM) of the G band calculated by T. Ando [68] as $\Delta\omega_G = Re[\Pi^{(\pm)}(\omega)]$ and $\Gamma_G = -2Im[\Pi^{(\pm)}(\omega)]$ [54], respectively, where Π is the phonon self energy given of the symmetric (+) or anti-symmetric (-) components, given by :

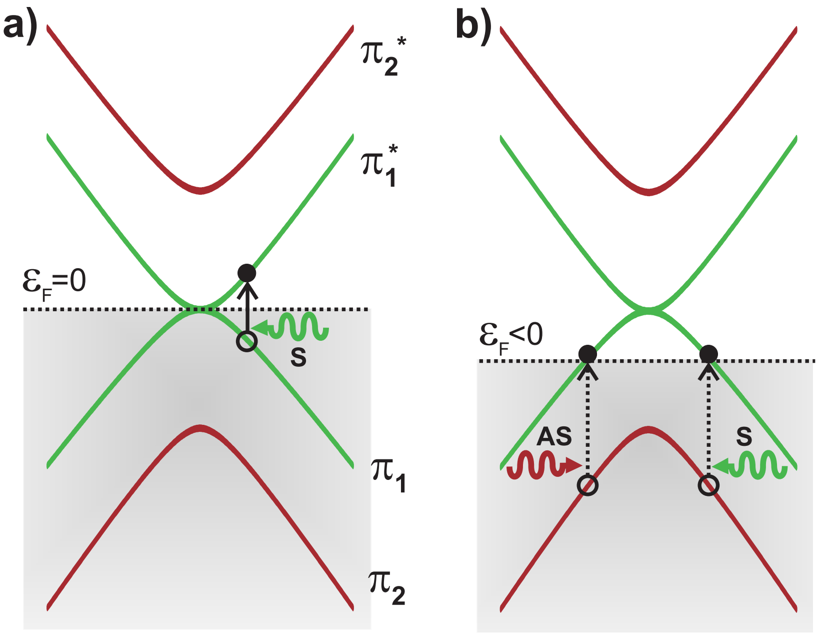

Figure 7.4: Parabolic band structure of bilayer graphene near the K point. The vertical arrows illustrates the possible transitions induced by symmetric (green) and antisymmetric (red) $\mathbf{q}$=0 phonons for (a) interband electron-hole pairs creation at (ε_F=0) and (b) intraband electron-hole pairs creation (ε_F <0). The gap opening is not considered in this diagram.

$$\Pi^{(\pm)}(\omega) = -\lambda \int_0^\infty \gamma^2 k dk \sum_{j,j'} \sum_{s,s'} \Phi^{(\pm)}_{jj'(k)} \times \frac{[f(\varepsilon_{sjk}) - f(\varepsilon_{s'j'k'})](\varepsilon_{sjk} - \varepsilon_{s'j'k'})}{(\hbar\omega + i\delta)^2 - (\varepsilon_{sjk} - \varepsilon_{s'j'k'})^2}. \tag{7.1}$$

The functions ε_{sjk} are the electronic band dispersions (k is the modulus of the wavevector), $s = +1$ and -1 denotes the conduction and valence bands, respectively, and $j = 1, 2$ specifies the two bands within the valence and conduction bands. The function $f(\varepsilon_{sjk})$ is the Fermi distribution and the matrix elements $\Phi^{\pm}_{jj'}(k)$ gives the relative contribution of the S (+) and AS (-) phonons for the interband and intraband electron-hole pairs formed in transitions [68]. The phenomenological damping parameter δ in Eq. 7.1 describes the charge inhomogeneity in the sample and washes out the logarithmic singularity present at $\varepsilon_F = \hbar\omega_0/2$. We have considered the value of $\delta = 0.1$ eV in the theoretical curves depicted in Fig. 7.3, since this is the smallest value of δ necessary to remove the initial phonon softening for $\varepsilon_F < \hbar\omega_0/2$ [41, 68].

Theoretical curves $\Delta\omega_G$ and Γ_G are calculated in units of $\lambda\omega_0$, where $\omega_0 =$ 0.196 eV is the energy of the optical phonon and λ is related to the strength of the electron-phonon coupling and given by [68]:

$$\lambda = 0.16 \times 10^{-3} ({}^{2}eV^{-2}) [\frac{\partial\gamma_0}{\partial b}]^2, \tag{7.2}$$

where γ_0 is the in-plane nearest-neighbor tight-binding parameter [see Fig. 7.2 (b)] and b is the C-C distance.

In order to compare the experimental and theoretical results depicted in Figs. 7.3 (a) and (b) we need to convert the experimental horizontal scale (applied gate voltage, in the bottom axis of Fig. 7.3) into the theoretical scale (Fermi energy, in the upper axis of Fig. 7.3), and the experimental vertical scales (in cm^{-1}, left side axes of Fig. 7.3) into the theoretical scales (in units of $\lambda\omega_0$, right side axes of Fig. 7.3).

To match the scales of the experimental (left axis) and calculated (right axis) values of $\Delta\omega_G$ and Γ_G, shown in Fig. 7.3, we have used the value $\partial\gamma_0/\partial b = 6.4$ eV $^{-1}$ in Eq. 7.2 [64]. Both theoretical curves $\Delta\omega_G$ and Γ_G are plotted in Fig. 7.3 as a function of the Fermi energy ε_F (top axis), while the experimental values are plotted as a function of gate voltage (bottom axis). In order to scale these axes, we have used the fact that both ε_F and V$_g$ are related to the electron (or hole) density n, which is assumed to be the same in both layers. The modulus of the Fermi energy $|\varepsilon_F|$ is related to the electron (or hole) density in the regime $|\varepsilon_F| < \gamma_1$ by [68] (see Chapter 4):

$$|\varepsilon_F| = \frac{1}{2}(-\gamma_1 + \sqrt{4n\pi\gamma^2 + \gamma_1^2}), \tag{7.3}$$

where $\gamma = \frac{\sqrt{3}}{2} a\gamma_0$, $a = 2.42$ is the lattice constant, $\gamma_0 \approx 3$eV and $\gamma_1 \sim 0.35$ eV is the out-of-plane nearest-neighbor parameter [see Fig. 7.2(b)]. A parallel plate capacitor model gives $n = 7.2 \times 10^{10}\text{cm}^{-2}V^{-1}(V_g - V_D)$ (Eq. 4.14), where V_D is the gate voltage needed to move the Fermi level to the Dirac point due to intrinsic doping of the sample. The value of $V_D = +\ 50$ V was obtained from the spectrum where the G-band has the largest FWHM [see Fig. 7.3(b)], since the symmetric phonon lifetime is minimum for $\varepsilon_F = 0$ [68].

Figure 7.3 shows that there is a qualitative agreement between our experimental results and the theoretical prediction of the dependence of the frequency and width of the symmetric and anti-symmetric optical phonons in bilayer graphene with the Fermi level. We shall stress that this good agreement is obtained despite the different approximations that have been done. Notice first that the theoretical model doesn't take into account the trigonal warping effect, the angular dependence of the electron-phonon coupling, and the strength $\partial\gamma_1/\partial b$ for the coupling between electrons and AS phonons [see Fig. 7.2(b)]. Moreover, we have used the simple model of a parallel capacitor with homogeneous carrier concentration in the two layers. A more complete model is needed to improve the fitting of the experimental data.

7.3 Summary

In summary, we have shown in this work that bilayer graphene is a unique material where the phonon renormalization tuned by charge transfer depends strongly on the symmetry of the phonons involved in the creation of electron-hole pairs. The hardening of the S mode and the softening of the AS phonon mode is explained by the creation of interband or intrabands electron-hole pairs by S and AS optical phonons, giving an experimental support for the theoretical predictions of the optical phonons dependence on charge concentration in bilayer graphene [68].

Chapter 8

Conclusion

8.1 General remarks

In the first part of this work we have presented Resonance Raman studies of monolayer and bilayer graphene, where the energy of the excitation laser line can be tuned continuously. Due to the double-resonance Raman mechanism, photons with different energies interact with electrons and phonons with different wavevectors. Therefore, by changing the energy of the excitation laser, it is possible to probe the dispersion of electrons and phonons near the Dirac point of graphene [47]. In particular, we performed a resonant Raman investigation of the G$'$ band in bilayer graphene which allowed us to obtain information about the electronic structure and to determine its tight-binding parameters [46, 116]. We found that there is a strong electron-hole asymmetry in bilayer graphene [46, 116].

Based in a group theory analysis, we have obtained the reducible representations of electrons and phonons in N-layer graphene systems. We have used this result to find the selection rules for light absorption, infrared activity, first-order Raman activity, second-order Raman processes and, in particular, for the double resonance Raman process.

The electron-phonon interaction is very strong in graphene, and some special phonons, specially those responsible for the main Raman features, can create an electron-hole pair. This process renormalizes the phonon energy giving rise to the so-called Kohn anomaly. However, it is suppressed when the Fermi level position is changed by an amount larger than half of the phonon energy. In the second part of this work we have presented experimental results in bilayer graphene [53], where the position of the Fermi level is tuned by applying a gate voltage. By monitoring the frequency and the width of the G-band we could probe distinct electron-phonon couplings in bilayer graphene which agrees well with the theory proposed by T. Ando [68]. The dependence of the energy and damping of these phonons modes on the Fermi level position is explained in terms of distinct couplings of the symmetric and anti-symmetric phonons with intra- and inter-band electron-hole transitions. Our results show that while the symmetric Raman mode hardens its frequency, the anti-symmetric mode softens when the Fermi level is moved away from the neutrality point.

Moreover, new theoretical predictions on electron-phonon in bilayer graphene show that it is possible to quantify the amount of doping in the two layers independently. Our experimental results were used in this theory to monitor the doping effects coming from the atmosphere and from the substrate.

8.2 Perspectives

Raman spectroscopy has already reveled new insights about physical properties in graphene systems, and is becoming a powerful tool to probe the quality, doping, number of layers and strain in graphene. Although this technique is well established for exfoliated graphene, it is clear that there are still today many open questions concerning the Raman spectra of epitaxial graphene. There are many contradictory results in the literature, concerning the peak frequency, the lineshape of the Raman G and G′ bands. With the improvements of graphene growth in different substrates and with a larger precision and homogeneity of the number of layers, Raman spectroscopy can answer these questions in a near future.

Another application of Raman in graphene is to further study the electron-phonon coupling mechanisms near the Γ and K points. Specially, in bilayer graphene with the application of top and bottom gate voltages, we expect to find correlations in the Raman spectra with the gap opening and to quantify the size of the gap with Raman spectroscopy. This would allow a fast characterization of the bilayer graphene gap by applying different values of gate voltage.

Moreover, the application of strain in graphene can be monitored in the Raman spectra, and the combination of resonance Raman scattering should provide information about the modifications of the phonon and electronic structure of graphene due to strain. Also the presence of defects modifies both electronic and phonon structures of graphene, but its implications in the Raman spectra are not yet fully understood. For example, until today it is not yet possible to distinguish different kind of defects.

Also, experimental Raman studies on graphene nanoribbons are still in a very early stage in the literature. On the other hand, a significant amount of theoretical effort has already been made to provide a framework that can be used to probe nanoribbon properties by Raman spectroscopy. One can then envision the determination of energy levels as a function of the edge structure and width of individual nanoribbons by Raman spectroscopy, as has been done for single wall carbon nanotubes.

For sure, Raman spectroscopy is a powerful tool for the graphene community. There are still unanswered questions about basic concepts of Raman process in graphene systems and applications yet to be discovered. Like in the carbon nanotubes field, Raman spectroscopy should play a major role for the understanding of the physical properties of graphene.

Appendix A

The electron-phonon Hamiltonian

A complete calculation of the electron-phonon interactions should start with the Hamiltonian of the ions of lattice whose mutual interaction should include a long-range Coulomb potential. Then one would include the electron gas, which will partially shield the interaction between the ions. Here we will treat a Hamiltonian that deals with short range interactions, where the Coulomb potential of an ion is screened due to the presence of other ions in the lattice. Also we neglect electron-electron interactions. We start with the unperturbed Hamiltonian where the electrons and the phonons are treated separately:

$$\mathcal{H}_0 = \sum_{\mathbf{k}} \varepsilon_{\mathbf{k}} c^{\dagger}_{\mathbf{k}} c_{\mathbf{k}} + \sum_{\mathbf{q}} \hbar\omega_{\mathbf{q}} a^{\dagger}_{\mathbf{q}} a_{\mathbf{q}}, \tag{A.1}$$

where $c^{\dagger}_{\mathbf{k}}$ ($c_{\mathbf{k}}$) is the creation (destruction) operator for the electrons with energy $\varepsilon_{\mathbf{k}}$, and the phonon creation (destruction) operators are $a^{\dagger}_{\mathbf{q}}$ ($a_{\mathbf{q}}$) with energy $\hbar\omega_q$ with momentum $\mathbf{q}$. To the Hamiltonian $\mathcal{H}_0$ we add the interaction Hamiltonian $\mathcal{H}_I$ for the electrons with the screened ions as:

$$\begin{aligned} \mathcal{H}_I &= \sum_{\mathbf{k},\mathbf{k}',\mathbf{l}} \langle \mathbf{k} | V(\mathbf{r} - \mathbf{l} - \mathbf{y}_{\mathbf{l}}) | \mathbf{k}' \rangle c^{\dagger}_{\mathbf{k}} c_{\mathbf{k}'} && \text{(A.2)} \\ &= \sum_{\mathbf{k},\mathbf{k}',\mathbf{l}} e^{i(\mathbf{k}-\mathbf{k}')\cdot(\mathbf{l}+\mathbf{y}_{\mathbf{l}})} V_{\mathbf{k},\mathbf{k}'} c^{\dagger}_{\mathbf{k}} c_{\mathbf{k}'}. && \text{(A.3)} \end{aligned}$$

The term inside the brakets means that an electron has been scattered from $\mathbf{k}$ to $\mathbf{k}'$ by a potential $V_{\mathbf{r}-\mathbf{l}-\mathbf{y}_{\mathbf{l}}}$ of a single ion, where $\mathbf{l}$ is the equilibrium position of the ion and $\mathbf{y_l}$ is the displacement of the ion. In the second line of Eq. A.2 we wrote the potential $V_{\mathbf{r-l-y_l}}$ in the form of a Fourier transform $V_{\mathbf{k,k'}}$. Assuming the the displacement $\mathbf{y_l}$ of the ion is very small that $(\mathbf{k'-k})\cdot\mathbf{y_l} \ll \mathbf{1}$, we have:

$$
\begin{aligned}
e^{i(\mathbf{k'-k})\cdot\mathbf{y_l})} &\simeq 1 + i(\mathbf{k'}-\mathbf{k})\cdot\mathbf{y_l}) \qquad (A.4)\\
&= 1 + iN^{-1/2}(\mathbf{k'}-\mathbf{k})\cdot\sum \mathbf{q}\mathbf{e}^{\mathbf{iq\cdot l}}\mathbf{y_q}, \qquad (A.5)
\end{aligned}
$$

where $\mathbf{q}=\mathbf{k}-\mathbf{k'}$. Then, $\mathcal{H}_I$ can be separated into $\mathcal{H}_{Bloch}+\mathcal{H}_{e-p}$, where $\mathcal{H}_{Bloch}$ is independent of the displacements. The $\mathcal{H}_{e-p}$ is dependent of the displacement, and thus it is the relevant part for the electron-phonon interaction. It can be written as:

$$
\begin{aligned}
\mathcal{H}_{e-p} &= iN^{-1/2}\sum_{\mathbf{k,k',l,q}} e^{i(\mathbf{k'-k+q})}(\mathbf{k'}-\mathbf{k})\cdot\mathbf{y_q}V_{\mathbf{k-k'}}c^{\dagger}_{\mathbf{k}}c_{\mathbf{k'}} \qquad (A.6)\\
&= iN^{-1/2}\sum_{\mathbf{k,k'}}(\mathbf{k'}-\mathbf{k})\cdot\mathbf{y_q}V_{\mathbf{k-k'}}c^{\dagger}_{\mathbf{k}}c_{\mathbf{k'}}. \qquad (A.7)
\end{aligned}
$$

The displacement $\mathbf{y_q}$ can be written in the harmonic approximation as a function of the phonon creation and destruction operators as:

$$
\mathbf{y_q} = \sqrt{\frac{\hbar}{2M\omega_{\mathbf{q}}}}(a^{\dagger}_{-\mathbf{q}} + a_{\mathbf{q}})\mathbf{s}, \qquad (A.8)
$$

where ω_q is the phonon frequency and M is the mass of the system (ions) and $\mathbf{s}$ is the direction of the displacement. Inserting Eq. A.6 in Eq. A.8 we have:

$$
\mathcal{H}_{e-p} = i\sum_{\mathbf{k,k',s}}\left(\frac{N\hbar}{2M\omega_{\mathbf{k,k',s}}}\right)^{1/2}(\mathbf{k'}-\mathbf{k})\cdot\mathbf{s}V_{\mathbf{k-k'}}(a^{\dagger}_{\mathbf{k'-k,s}} - a_{\mathbf{k-k',s}})c^{\dagger}_{\mathbf{k}}c_{\mathbf{k'}}. \qquad (A.9)
$$

Depending on the relative direction of $\mathbf{s}$ and $\mathbf{q}$, the phonons can be either longitunally or transversely polarized. Then, only the longitudinal modes, which $\mathbf{s}$ are parallel to $\mathbf{k}' - \mathbf{k}$, enter in the $\mathcal{H}_{e-p}$. With these simplifications we are left with the Frohlich Hamiltonian:

$$\mathcal{H} = \sum_{\mathbf{k}} \varepsilon_{\mathbf{k}} c^{\dagger}_{\mathbf{k}} c_{\mathbf{k}} + \sum_{\mathbf{q}} \hbar\omega_{\mathbf{q}} a^{\dagger}_{\mathbf{k}} a_{\mathbf{k}} + \sum_{\mathbf{k},\mathbf{k}'} M_{\mathbf{k}\mathbf{k}'} (a^{\dagger}_{-\mathbf{q}} + a_{\mathbf{q}}) c^{\dagger}_{\mathbf{k}} c_{\mathbf{k}'}, \tag{A.10}$$

where the electron-phonon matrix element is defined by:

$$M'_{\mathbf{k}\mathbf{k}} = i \left(\frac{N\hbar}{2M\omega_{\mathbf{k},\mathbf{k}',\mathbf{s}}} \right)^{1/2} |\mathbf{k}' - \mathbf{k}| V_{\mathbf{k}-\mathbf{k}'}. \tag{A.11}$$

The electron-phonon interaction given in Eq. A.10 can viewed as two parts, the first operator $a^{\dagger}_{-\mathbf{q}} c^{\dagger}_{\mathbf{k}} c_{\mathbf{k}}$ represents an electron being scattered from $\mathbf{k}'$ to $\mathbf{k}$ with a emission of a phonon with wavevector $-\mathbf{q}$. The second operator $a_{\mathbf{q}} c^{\dagger}_{\mathbf{k}} c_{\mathbf{k}}$ represents the electron being scattered from $\mathbf{k}'$ to $\mathbf{k}$ with the absorption of a phonon with wavevector $\mathbf{q}$. These two process are represented in Fig. A.1 (a) and (b) respectively. In both process the total wavevector of the scattering process is conserved.

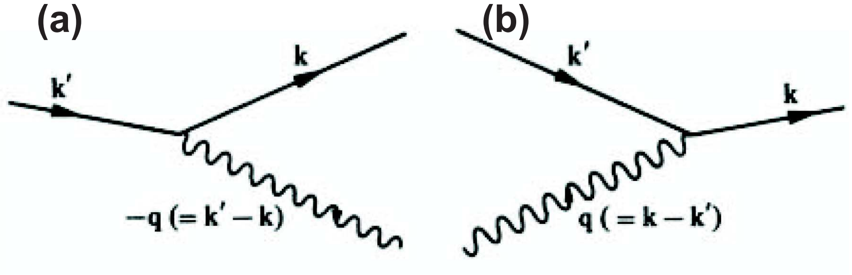

Figure A.1: (a) An electron being scattered from $\mathbf{k}'$ to $\mathbf{k}$ with the emission of a phonon with wavevector $-\mathbf{q}$. (b) The same but with the absorption of a phonon with wavevector $\mathbf{q}$.

To calculate the phonon frequencies we use pertubation theory to second order in the electron-phonon Hamiltonian $\mathcal{H}_{ep}$ (third term in Eq. A.10):

$$\varepsilon = \varepsilon_0 + \langle \Phi_{\mathbf{k}} | \mathcal{H}_{ep} | \Phi_{\mathbf{k}} \rangle + \langle \Phi_{\mathbf{k}} | \frac{\mathcal{H}_{ep}\mathcal{H}_{ep}}{\varepsilon_0 - \mathcal{H}_0} | \Phi_{\mathbf{k}} \rangle, \tag{A.12}$$

where ε_0 is the unpertubed energy of the state $\Phi_{\mathbf{k}}$ having n_q phonons in the mode $\mathbf{q}$ and n_k electrons in the state $\mathbf{k}$. The first order term vanishes, since $\mathcal{H}_{ep}$ either creates or destroy an electron in the state $\mathbf{k}$, leaving the resulting wavefunction ortogonal to Φ_k. The second order term ε_2 can be written as:

$$\begin{aligned}\varepsilon_2 &= \langle\Phi_k|\sum_{k,k'} M_{kk'}\frac{(a^\dagger_{-\mathbf{q}}+a_{\mathbf{q}})c^\dagger_{\mathbf{k}}c_{\mathbf{k}'}}{\varepsilon_0-\mathcal{H}_0}\times\sum_{k'',k'''} M_{k''k'''}\frac{(a^\dagger_{-\mathbf{q}'}+a_{\mathbf{q}'})c^\dagger_{\mathbf{k}''}c_{\mathbf{k}'''}}{\varepsilon_0-\mathcal{H}_0}|\Phi_{\mathbf{k}}\rangle && \text{(A.13)}\\ &= \langle\Phi_k|\sum_{k,k'}|M_{kk'}|^2[\frac{(a^\dagger_{-\mathbf{q}}a_{-\mathbf{q}})c^\dagger_{\mathbf{k}}c_{\mathbf{k}}c^\dagger_{\mathbf{k}'}c_{\mathbf{k}'}}{\varepsilon_0-\mathcal{H}_0}+\frac{(a^\dagger_{-\mathbf{q}}a_{-\mathbf{q}})c^\dagger_{\mathbf{k}}c_{\mathbf{k}}c^\dagger_{\mathbf{k}'}c_{\mathbf{k}'}}{\varepsilon_0-\mathcal{H}_0}]|\Phi_{\mathbf{k}}\rangle, && \text{(A.14)}\end{aligned}$$

all other matrix elements are zero. For example:

$$\langle\Phi_{\mathbf{k}}|(a^\dagger_{-\mathbf{q}}a^\dagger_{-\mathbf{q}})c^\dagger_{\mathbf{k}}c^\dagger_{\mathbf{k}}c_{\mathbf{k}'}c_{\mathbf{k}'}|\Phi_{\mathbf{k}}\rangle = \langle\Phi_{\mathbf{k}'}|\Phi_{\mathbf{k}}\rangle = 0. \qquad \text{(A.15)}$$

The first therm in the brackets represents an electron being scattered from $\mathbf{k}$ to $\mathbf{k}'$ by absorbing a phonon with wavenumber $\mathbf{q} = \mathbf{k} - \mathbf{k}'$. The first denominator $(\varepsilon_0 - \mathcal{H}_0)$ can be written as the energy difference between the initial and intermediated, thus it can written as $(\varepsilon_{\mathbf{k}} + \hbar\omega_{_{-\mathbf{q}}} - \varepsilon_{\mathbf{k}'})$. In the final state the electron is scattered back with the emission of a phonon. Similarly the denominator of the second term in the brackets can be written as $(\varepsilon_{\mathbf{k}} - \hbar\omega_{_{-\mathbf{q}}} - \varepsilon_{\mathbf{k}'})$.

Now we write the creation and destruction operator in terms of occupation numbers ($n_{\mathbf{k}}$ or $n_{\mathbf{q}}$). For fermions (electrons) we use following properties:

$$\begin{aligned} c^\dagger_{\mathbf{k}}c_{\mathbf{k}} &= n_{\mathbf{k}} && \text{(A.16)}\\ c_{\mathbf{k}}c^\dagger_{\mathbf{k}} &= 1 - n_{\mathbf{k}}, && \text{(A.17)}\end{aligned}$$

and for bosons (phonons):

$$\begin{aligned} a^\dagger_{\mathbf{q}}a_{\mathbf{q}} &= n_{\mathbf{q}} && \text{(A.18)}\\ a_{\mathbf{q}}a^\dagger_{\mathbf{q}} &= 1 + n_{\mathbf{q}}, && \text{(A.19)}\end{aligned}$$

then Eq. A.13 can be written as:

$$\varepsilon_2 \propto \frac{n_{-\mathbf{q}} n_{\mathbf{k}}(1-n_{\mathbf{k}'})}{\varepsilon_{\mathbf{k}} + \hbar\omega_{_{-\mathbf{q}}} - \varepsilon_{\mathbf{k}'}} + \frac{n_{(1+\mathbf{q})} n_{\mathbf{k}}(1-n_{\mathbf{k}'})}{\varepsilon_{\mathbf{k}} - \hbar\omega_{_{-\mathbf{q}}} - \varepsilon_{\mathbf{k}'}}, \tag{A.20}$$

making $\omega_{-\mathbf{q}} = \omega_{\mathbf{q}}$ and $\langle n_{-\mathbf{q}} \rangle = \langle n_{\mathbf{q}} \rangle$, we have:

$$\begin{aligned} \varepsilon_2 \quad & \propto n_{\mathbf{k}}(1-n_{\mathbf{k}'}) \frac{2n_{\mathbf{q}}(\varepsilon_{\mathbf{k}} - \varepsilon_{\mathbf{k}'}) + \varepsilon_{\mathbf{k}} - \varepsilon_{\mathbf{k}'} + \hbar\omega_{\mathbf{q}}}{(\varepsilon_{\mathbf{k}} - \varepsilon_{\mathbf{k}'})^2 - (\hbar\omega_{\mathbf{q}})^2} \\ & \propto n_{\mathbf{k}} \left(\frac{2n_{\mathbf{q}}(\varepsilon_{\mathbf{k}} - \varepsilon_{\mathbf{k}'})}{(\varepsilon_{\mathbf{k}} - \varepsilon_{\mathbf{k}'})^2 - (\hbar\omega_{\mathbf{q}})^2} + \frac{(1-n_{\mathbf{k}})(\varepsilon_{\mathbf{k}} - \varepsilon_{\mathbf{k}'} + \hbar\omega_{\mathbf{q}})}{(\varepsilon_{\mathbf{k}} - \varepsilon_{\mathbf{k}'} + \hbar\omega_{\mathbf{q}})(\varepsilon_{\mathbf{k}} - \varepsilon_{\mathbf{k}'} - \hbar\omega_{\mathbf{q}})} \right), \end{aligned} \tag{A.21}$$

where we had use the fact that $\langle n_{\mathbf{k}} n_{\mathbf{k}'} n_{\mathbf{q}} \rangle$ is zero. Then the total energy ε of the system can be written as:

$$\varepsilon = \varepsilon_0 + \sum_{\mathbf{k},\mathbf{k}'} |M_{\mathbf{k},\mathbf{k}'}|^2 \langle n_{\mathbf{k}} \rangle \left(\frac{2\langle n_{\mathbf{q}} \rangle (\varepsilon_{\mathbf{k}} - \varepsilon_{\mathbf{k}'})}{(\varepsilon_{\mathbf{k}} - \varepsilon_{\mathbf{k}'})^2 - (\hbar\omega_{\mathbf{q}})^2} + \frac{(1 - \langle n_{\mathbf{k}} \rangle)}{\varepsilon_{\mathbf{k}} - \varepsilon_{\mathbf{k}'} - \hbar\omega_{\mathbf{q}}} \right). \tag{A.22}$$

Now the perturbed phonon energy $\hbar\omega^p_{\mathbf{q}}$, is the energy required to increase $\langle n_{\mathbf{q}} \rangle$ by unit, then we find $E(\mathbf{k}) \propto \mathbf{k^2}$:

$$\hbar\omega^p_{\mathbf{q}} \quad = \frac{\partial \varepsilon}{\partial \hbar\omega_{\mathbf{q}}} \tag{A.23}$$

$$= \hbar\omega_{\mathbf{q}} + \sum_{\mathbf{k}} |M_{\mathbf{k},\mathbf{k}'}|^2 \frac{2\langle n_{\mathbf{k}} \rangle (\varepsilon_{\mathbf{k}} - \varepsilon_{\mathbf{k}'})}{(\varepsilon_{\mathbf{k}} - \varepsilon_{\mathbf{k}'})^2 - (\hbar\omega_{\mathbf{q}})^2}. \tag{A.24}$$

Appendix B

The electric dipole approximation

Here we will give more details, why the electric dipole approximation given in Sec. 3.1.1 can be used in crystals. For a atom or molecule the approximation where the the wavevector of the light $\mathbf{k_L}$ is larger then the dimensions of the atom or molecule is reasonable. However for crystals this approximation is not direct, but can be applied in the same way as we shall see below.

Consider the light-matter interaction Hamiltonian given as [70]:

$$H_I = \frac{eE_0}{im\omega}[e^{i(\mathbf{k_L}\cdot\mathbf{R}-\omega t)} - e^{-i(\mathbf{k_L}\cdot\mathbf{R}-\omega t)}](\hat{\mathbf{e}}\cdot\hat{\mathbf{p}}), \tag{B.1}$$

this equation is the same as shown in Sec. 3.1.1. For simplicity we will write this equation taking in account only the first term and without including the time dependence. Then we have:

$$H_I \propto [e^{i(\mathbf{k_L}\cdot\mathbf{R})}](\hat{\mathbf{e}}\cdot\hat{\mathbf{p}}). \tag{B.2}$$

Now the initial state will correspond to electrons in the valence ($|v\rangle$) band, and the final state as electrons in the conduction ($|c\rangle$) band. Writing the Bloch functions for these states we have [76]:

$$|v\rangle = \quad u_{v,k_v}(\mathbf{r})e^{[i(\mathbf{k_v}\cdot\mathbf{R})]} \tag{B.3}$$

$$|c\rangle = \quad u_{c,k_c}(\mathbf{r})e^{[i(\mathbf{k_c}\cdot\mathbf{R})]}. \tag{B.4}$$

Given the initial and final states written in terms of Bloch functions we compute the matrix element $|\langle c|H_I|v\rangle|^2$, which from Eq. B.2 can be written as:

$$\langle c|H_I|v\rangle \propto \int u^*_{c,k_c} e^{[i(\mathbf{k_L}-\mathbf{k_c})\cdot\mathbf{R}]}(\hat{\mathbf{e}}\cdot\hat{\mathbf{p}})u_{v,k_v}e^{[i\mathbf{k_v}\cdot\mathbf{R}]}d\mathbf{R}. \tag{B.5}$$

Operating with $\hat{\mathbf{p}}$ on $u_{v,k_v}e^{[i\mathbf{k_v}\cdot\mathbf{R}]}$ yields two terms [76]:

$$\hat{\mathbf{p}}u_{v,k_v}e^{[i\mathbf{k_v}\cdot\mathbf{R}]} = e^{[i\mathbf{k_v}\cdot\mathbf{R}]}\hat{\mathbf{p}}u_{v,k_v} + \hbar\mathbf{k_v}u_{v,k_v}e^{[i\mathbf{k_v}\cdot\mathbf{R}]}. \tag{B.6}$$

The second term when multiplied by $\mathbf{u}^*_{\mathbf{c},\mathbf{k_c}}$ in Eq. B.5 vanishes, since $\mathbf{u}_{\mathbf{c},\mathbf{k_c}}$ and $\mathbf{u}_{\mathbf{v},\mathbf{k_v}}$ are orthogonal. Then we are left with the following integral of Eq. B.5 [76]:

$$\int \mathbf{u}^*_{\mathbf{c},\mathbf{k_c}} e^{[i(\mathbf{k_L}-\mathbf{k_c}+\mathbf{k_v})\cdot\mathbf{R}]}\hat{\mathbf{p}}\mathbf{u}_{\mathbf{v},\mathbf{k_v}}\mathbf{dR}. \tag{B.7}$$

Now we write $\mathbf{R}$ in terms of the lattice vector $\mathbf{R_l}$ and a vector $\mathbf{r}'$ which lies in the unit cell, $\mathbf{R} = \mathbf{R_l} + \mathbf{r}'$ [76], and inserting it in the above equation we have:

$$\int \mathbf{u}^*_{\mathbf{c},\mathbf{k_c}} e^{[i(\mathbf{k_L}-\mathbf{k_c}+\mathbf{k_v})\cdot\mathbf{R}]}\hat{\mathbf{p}}\mathbf{u}_{\mathbf{v},\mathbf{k_v}}\mathbf{dR} \tag{B.8}$$

$$\left(\sum_l e^{[i(\mathbf{k_L}-\mathbf{k_c}+\mathbf{k_v})\cdot\mathbf{R}_l]}\right)\int_{\text{unitcell}} \mathbf{u}^*_{\mathbf{c},\mathbf{k_c}} e^{[i(\mathbf{k_L}-\mathbf{k_c}+\mathbf{k_v})\cdot\mathbf{r}']}\hat{\mathbf{p}}\mathbf{u}_{\mathbf{v},\mathbf{k_v}}\mathbf{dr}'. \tag{B.9}$$

The summation between the parenthesis is over all lattice vectors, then it results in a delta function $\delta(\mathbf{k_L}-\mathbf{k_c}+\mathbf{k_v})$, which results in the wavevector conservation rule [76]:

$$\mathbf{k_L}+\mathbf{k_v} = \mathbf{k_c}. \tag{B.10}$$

This wavevector conservation rule is a consequence of the translational symmetry of a perfect crystal, but it can be relaxed in presence of defects [76]. If the wavevector of the incident light is neglected, then $\mathbf{k_v} = \mathbf{k_c}$, and the transitions are said to be vertical [70, 76]. This is valid if we compare the size of $\mathbf{k_L}$ with typical sizes of a unit cell of a crystal.

Using Eq. B.10 into the integral of Eq. B.8 we have:

$$\int_{\text{unitcell}} \mathbf{u}^*_{\mathbf{c},\mathbf{k_v}+\mathbf{k_L}} \hat{\mathbf{p}} \mathbf{u}_{\mathbf{v},\mathbf{k_v}} \mathbf{dr}'. \tag{B.11}$$

Now if we assume that the wavevector of the light is much smaller than the size of the Brillouin zone of the crystal, then $\mathbf{u}^*_{\mathbf{c},\mathbf{k_v}+\mathbf{k_L}}$ can be expanded in Taylor series around $\mathbf{k_L}$ as [76]:

$$\mathbf{u}^*_{\mathbf{c},\mathbf{k_v}+\mathbf{k_L}} = \mathbf{u}^*_{\mathbf{c},\mathbf{k_v}} + \mathbf{k_L} \cdot \nabla_{\mathbf{k}} \mathbf{u}^*_{\mathbf{c},\mathbf{k_v}} + ... \tag{B.12}$$

To first order, the light-matter interaction matrix element can be written as [76]:

$$|\langle c|H_I|v\rangle|^2 = \left(\int_{\text{unitcell}} \mathbf{u}^*_{\mathbf{c},\mathbf{k_v}} (\hat{\mathbf{e}} \cdot \hat{\mathbf{p}}) \mathbf{u}_{\mathbf{v},\mathbf{k_v}} \mathbf{dr}' \right)^2. \tag{B.13}$$

Eq. B.13 is the electric dipole approximation. Notice that the electric dipole approximation done here is equivalent to what was done in Sec. 3.1.1, where we expanded the exponential term $e^{i(\mathbf{k_L} \cdot \mathbf{R})}$ and kept only the first term [76].

However if the electric dipole matrix element is null, then one should consider higher terms in the Taylor series in Eq. B.13. For example the next term $\mathbf{k_L} \cdot \nabla_{\mathbf{k}} \mathbf{u}^*_{\mathbf{c},\mathbf{k_v}}$ in the Taylor expansion gives rise to electric quadrupole and magnetic dipole transitions [76].

APPENDIX C

Character tables

In this Appendix, the character tables for all points inside the first Brillouin zone of monolayer graphene (Sec. C.1), N-even (Sec. C.2) and N-odd (Sec. C.3) will be given. Also we give the character of equivalence (χ^{eq}) and the atom equivalence representation (Γ^{eq}) for each table. With Γ^{eq} is possible to calculate the representations for electrons and vibrations for each point in the Brillouin zone for different values of N-layer, as done in Chapter 5. Also in Sec. C.4 we give the conversion from space group to point group irreducible representations.

C.1 Monolayer graphene

Table C.1: Character table for the Γ point (D_{6h}).

	E	C_3^+ C_3^-	C_2	C_6^- C_6^+	$C_2^{\prime A}$ $C_2^{\prime B}$ $C_2^{\prime C}$	$C_2^{\prime\prime A}$ $C_2^{\prime\prime B}$ $C_2^{\prime\prime C}$	i	S_6^+ S_6^-	σ_h	S_3^- S_3^+	σ_d^A σ_d^B σ_d^C	σ_v^A σ_v^B σ_v^C		
Γ_1^+	1	1	1	1	1	1	1	1	1	1	1	1		$x^2+y^2\ ,\ z^2$
Γ_2^+	1	1	1	1	-1	-1	1	1	1	1	-1	-1		
Γ_3^+	1	1	-1	-1	-1	1	1	1	-1	-1	-1	1		
Γ_4^+	1	1	-1	-1	1	-1	1	1	-1	-1	1	-1		
Γ_5^+	2	-1	-2	1	0	0	2	-1	-2	1	0	0		(xz, yz)
Γ_6^+	2	-1	2	-1	0	0	2	-1	2	-1	0	0		(x^2-y^2, xy)
Γ_1^-	1	1	1	1	1	1	-1	-1	-1	-1	-1	-1		
Γ_2^-	1	1	1	1	-1	-1	-1	-1	-1	-1	1	1	z	
Γ_3^-	1	1	-1	-1	-1	1	-1	-1	1	1	1	-1		
Γ_4^-	1	1	-1	-1	1	-1	-1	-1	1	1	-1	1		
Γ_5^-	2	-1	-2	1	0	0	-2	1	2	-1	0	0	(x, y)	
Γ_6^-	2	-1	2	-1	0	0	-2	1	-2	1	0	0		
χ^{eq}	2	2	0	0	0	2	0	0	2	2	2	0	Γ^{eq}	$\Gamma_1^+ \oplus \Gamma_3^-$

Table C.2: Character table for the **K** point (D_{3h}).

	E	C_3^+ C_3^-	$C_2^{\prime A}$ $C_2^{\prime B}$ $C_2^{\prime C}$	σ_h	S_3^- S_3^+	σ_v^A σ_v^B σ_v^C		
K_1	1	1	1	1	1	1		$x^2+y^2\ ,\ z^2$
K_2	1	1	-1	1	1	-1		
K_3	2	-1	0	2	-1	0	(x, y)	(x^2-y^2, xy)
K_4	1	1	1	-1	-1	-1		
K_5	1	1	-1	-1	-1	1	z	
K_6	2	-1	0	-2	1	0		(xz, yz)
χ^{eq}	2	-1	0	2	-1	0	Γ^{eq}	K_3

Table C.3: Character table for the **M** point (D_{2h}).

	E	C_2	$C_2^{'A}$	$C_2^{''A}$	i	σ_h	σ_d^A	σ_v^A		
M_1^+	1	1	1	1	1	1	1	1		x^2 , y^2 , z^2
M_2^+	1	1	-1	-1	1	1	-1	-1		xy
M_3^+	1	-1	1	-1	1	-1	1	-1		xz
M_4^+	1	-1	-1	1	1	-1	-1	1		yz
M_1^-	1	1	1	1	-1	-1	-1	-1		
M_2^-	1	1	-1	-1	-1	-1	1	1	z	
M_3^-	1	-1	1	-1	-1	1	-1	1	y	
M_4^-	1	-1	-1	1	-1	1	1	-1	x	
χ^{eq}	2	0	0	2	0	2	2	0	Γ^{eq}	$M_1^+ \oplus M_4^-$

Table C.4: Character table for the Σ point (C_s).

	E	$C_2^{''A}$	σ_h	σ_d^A		
Σ_1	1	1	1	1	x	x^2 , y^2 , z^2
Σ_2	1	1	-1	-1		zy
Σ_3	1	-1	1	-1	y	xy
Σ_4	1	-1	-1	1	z	zx
χ^{eq}	2	2	2	2	Γ^{eq}	$2\Sigma_1$

Table C.5: Character table for **T** and **T**′ points (C_{2v}).

	E	$C_2^{'A}$	σ_h	σ_v^A		
T_1	1	1	1	1	y	x^2 , y^2 , z^2
T_2	1	1	-1	-1		xz
T_3	1	-1	1	-1	x	xy
T_4	1	-1	-1	1	z	yz
χ^{eq}	2	0	2	0	Γ^{eq}	$T_1 \oplus T_3$

Table C.6: Character table for the **u** point (C_s).

	E	σ_h		
u^+	1	1	x , y	x^2 , y^2 , z^2 , xy
u^-	1	-1	z	zy , zx
χ^{eq}	2	2	Γ^{eq}	$2u^+$

C.2 N-even

Table C.7: Character table for the Γ point (D_{3d}).

	E	C_3^+ C_3^-	$C_2^{\prime A}$ $C_2^{\prime B}$ $C_2^{\prime C}$	i	iC_3^+ iC_3^-	i$C_2^{\prime A}$ i$C_2^{\prime B}$ i$C_2^{\prime C}$		
Γ_1^+	1	1	1	1	1	1		x^2+y^2 , z^2
Γ_2^+	1	1	-1	1	1	-1		
Γ_3^+	2	-1	0	2	-1	0	(xz,yz)	(x^2-y^2,xy)
Γ_1^-	1	1	1	-1	-1	-1		
Γ_2^-	1	1	-1	-1	-1	1	z	
Γ_3^-	2	-1	0	-2	1	0		(x,y)
χ^{eq}	2N	2N	0	0	0	2N	Γ^{eq}	$N(\Gamma_1^+ + \Gamma_2^-)$

Table C.8: Character table for the **K** point (D_3).

	E	C_3^+ C_3^-	$C_2^{\prime A}$ $C_2^{\prime B}$ $C_2^{\prime C}$		
K_1	1	1	1	x^2+y^2 , z^2	
K_2	1	1	-1		
K_3	2	-1	0	(xz,yz)	(x^2-y^2,xy)
χ^{eq}	2N	N/2	0	Γ^{eq}	$\frac{N}{2}(K_1+K_2+K_3)$

Table C.9: Character table for **M** point (C_{2h}).

	E	$C_2^{\prime A}$	σ_d	i		
M_1^+	1	1	1	1		x^2 , y^2 , z^2 , xy
M_1^-	1	1	-1	-1	x,y	
M_2^+	1	-1	-1	1		xz , yz
M_2^-	1	-1	1	-1	z	
χ^{eq}	2N	0	N/2	0	Γ^{eq}	$N(M_1^+ \oplus M_2^-)$

Table C.10: Character table for **T** and **T′** points (C_2).

	E	$C_2^{'A}$		
T_1	1	1		x^2 , y^2 , z^2 , xy
T_2	1	-1		xz , yz
χ^{eq}	2N	0	Γ^{eq}	$N(T_1 \oplus T_2)$

Table C.11: Character table for Σ point (C_{1v}).

	E	σ_v		
Σ_1	1	1		x^2 , y^2 , z^2 , xy
Σ_2	1	-1		xz , yz
χ^{eq}	2N	2N	Γ^{eq}	$2N(\Sigma_1)$

Table C.12: Character table for **u** point (C_1).

	E		
u_1	1		x^2 , y^2 , z^2 , xy , xz , yz
χ^{eq}	2N	Γ^{eq}	$2N(u_1)$

C.3 N-odd

Table C.13: Character table for the Γ point (D_{3h}).

	E	C_3^+ C_3^-	$C_2^{'A}$ $C_2^{'B}$ $C_2^{'C}$	σ_h	S_3^- S_3^+	σ_v^A σ_v^B σ_v^C		
Γ_1^+	1	1	1	1	1	1		$x^2+y^2\ ,\ z^2$
Γ_1^-	1	1	-1	1	1	-1		
Γ_3^+	2	-1	0	2	-1	0	(x,y)	(x^2-y^2,xy)
Γ_2^+	1	1	1	-1	-1	-1		
Γ_2^-	1	1	-1	-1	-1	1	z	
Γ_3^-	2	-1	0	-2	1	0		(xz,yz)
χ^{eq}	2N	2N	2	2	2	2N	Γ^{eq}	$[(N+1)\Gamma_1^+ + (N-1)\Gamma_2^-]$

Table C.14: Character table for the **K** point (C_{3h}).

	E	C_3	C_3^2	σ_h	S_3^- S_3	$(\sigma_h C_3^2)$		
K_1^+	1	1	1	1	1	1		$x^2+y^2\ ,\ z^2$
K_1^-	1	1	1	-1	-1	-1	z	
K_2^+	1	ω	ω^2	1	ω	ω^2	(x,y)	(x^2-y^2,xy)
K_2^{+*}	1	ω^2	ω	1	ω^2	ω		
K_2^-	1	ω	ω^2	-1	-ω	-ω^2		
K_2^{-*}	1	ω^2	ω	-1	-ω^2	-ω		(xz,yz)
χ^{eq}	2N	3+ω^2	3+ω	2	1+ω^2	1+ω	Γ^{eq}	$\Gamma^{eq} = [(\frac{N-1}{2})K_1^- + (\frac{N+1}{2})K_1^+ + g(N)K_2^{-*}(K_2^-) + g(N-2)(K_2^-)(K_2^{-*}) + g(N)K_2^+ + g(N+2)K_2^{+*}]$

where $g(N) = \sum_{m=0}^{\infty} \Theta(N-4m-2)$, where $\Theta(x)$ is equal to 0 if $x < 0$ and equal 1 otherwise.

Table C.15: Character table for **M** point (C_{2v}).

	E	C_2^A	σ_v^A	σ_v^B		
M_1	1	1	1	1	y	x^2 , y^2 , z^2
M_2	1	1	-1	-1		xz
M_3	1	-1	1	-1	x	xy
M_4	1	-1	-1	1	z	yz
χ^{eq}	2N	2	2	2N	Γ^{eq}	$[(N-1)M_1 + (N+1)M_2]$

Table C.16: Character table for the **T** and **T**′ points (C_{1h}).

	E	σ_h		
T^+	1	1	x , y	x^2 , y^2 , z^2 , xy
T^-	1	-1	z	zy , zx
χ^{eq}	2N	2	Γ^{eq}	$[(N-1)T^+ + (N+1)T^-]$

Table C.17: Character table for the Σ point (C_{2v}).

	E	C_2^A	σ_v^A	σ_v^B		
Σ_1	1	1	1	1	x	x^2 , y^2 , z^2
Σ_2	1	1	-1	-1		zy
Σ_3	1	-1	1	-1	y	xy
Σ_4	1	-1	-1	1	z	zx
χ^{eq}	2N	2	2	2N	Γ^{eq}	$[(N-1)\Sigma_1 + (N+1)\Sigma_4]$

Table C.18: Character table for the **u** point (C_{1h}).

	E	σ_h		
u^+	1	1	x , y	x^2 , y^2 , z^2 , xy
u^-	1	-1	z	zy , zx
χ^{eq}	2N	2	Γ^{eq}	$[(N-1)u^+ + (N+1)u^-]$

C.4 Notation conversion from space group to point group irreducible representations

In Chapter 5 we derived the Γ_π and $\Gamma_{lat.vib}$ for all points in the first BZ of multilayer graphene maintaining the notation of space group (SG) for the irreducible representations. The conversion to point group (PG) representation is obtained considering that (***a***) superscript sign “+´´ or “-´´ applies if the character of the horizontal mirror (σ_h) or inversion (i) is positive or negative, respectively; (***b***) the subscript number is given following the order of the point group irreducible representations; (***c***) two representations can only have the same number if they have superscript with positive or negative signs. As an example we give in Table C.19 the Γ point space group notation conversion to the D_{3h} (N-odd) and D_{3d} (N-even) point groups and for the K point space group to the C_{3h} (N-odd) and D_3 (N-even) point groups.

Table C.19: Example of irreducible representation notation conversion from the Γ point space group to D_{3h} and D_{3d} point groups, and from the K point space group to C_{3h} and D_3 point groups.

Γ point				**K point**			
D_{3h}		**D_{3d}**		**C_{3h}**		**D_3**	
SG	**PG**	**SG**	**PG**	**SG**	**PG**	**SG**	**PG**
Γ_1^+	A_1'	Γ_1^+	A_{1g}	K_1^+	A'	K_1	A_1
Γ_1^-	A_1''	Γ_1^-	A_{1u}	K_1^-	A''	K_2	A_2
Γ_2^+	A_2'	Γ_2^+	A_{2g}	K_2^+	E'	K_3	E
Γ_2^-	A_2''	Γ_2^-	A_{2u}	K_2^{+*}	E'^*		
Γ_3^+	E'	Γ_3^+	E_g	K_2^-	E''		
Γ_3^-	E''	Γ_3^-	E_u	K_2^{-*}	E''^*		

APPENDIX D

Other Raman scattering experiments in graphene

In this Appendix we give an summary of other preliminary works that originated from this PhD program. In Sec. D.1, we will discuss a new work that represents an extension of our results presented in Chapter 6, but with laser lines ranging from the near infrared (NIR) to the visible range. The second work presented in Sec. D.2 is the study of the Raman bands of monolayer graphene as a function of temperature ranging from room temperature to 250° degrees.

D.1 Kohn anomaly at the K point of bilayer graphene

In order to probe electrons and phonons still closer to the K point, we have extended the range of laser energies, measuring the G' Raman band of bilayer graphene with many laser lines in the range 1.33 to 2.81 eV. The measurements in the near-IR range (1.33 to 1.69 eV) allowed us to observe a non-linear softening of the phonon branch near the K point, and the significant splitting of the symmetric (S) and anti-symmetric (AS) phonon branches. In particular, we showed that the phonon softening is stronger for the S branch. Concerning the electronic structure, we have also considered the in-plane second-neighbor hopping parameter, which is expected to be of the same order as the out-of-plane nearest-neighbor parameters, to describe the G' Raman band dispersion.

Fig. D.1 shows the phonon dispersion of the S (full circles) and AS (open circles) branches obtained from the resonance Raman results. Fig. D.1 also shows the theoretical phonon dispersion near the Dirac point of the iTO phonon branch of monolayer graphene calculated using the tight-binding approximation by Popov

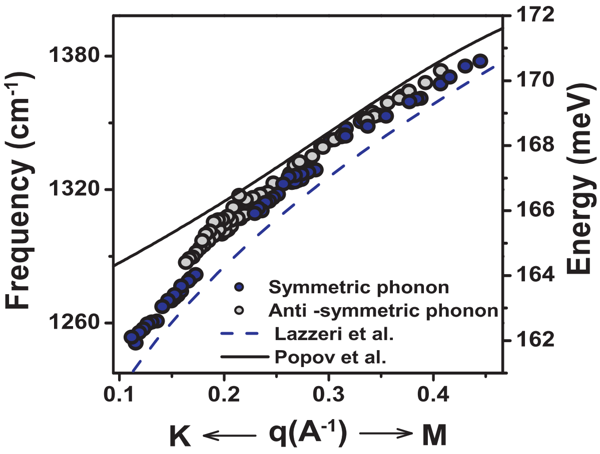

Figure D.1: Experimental iTO phonon dispersion of bilayer graphene near the K point of the S (full circles) and AS (open circles) branches. The solid and dashed curves correspond, respectively, to the theoretical iTO phonon dispersion of monolayer graphene calculated using tight-binding by Popov *et al.* [122] and using DFT by Lazzeri *et al.* [130] within the *GW* approximation.

et al. [122] (solid curve) and using DFT by Lazzeri *et al.* [130] (dashed curve) within the *GW* approximation, where electron-electron interaction is taken into account. Notice that the phonon dispersion calculated by tight-binding fails to describe the data for lower phonon energies, which are in good agreement with the calculations within the *GW* approximation. This result shows the importance of considering electron-phonon and electron-electron interactions in order to correctly describe the phonon dispersion near the K point of graphene systems [49].

D.2 Temperature effects on the Raman spectra of graphene: doping and phonon anharmonities

We have also investigated by Raman spectroscopy the modification of the electronic properties of graphene due to temperature and environment effects. We observed that different types of doping regimes occur as a function of temperature, due absorption/desorption of molecular donors/acceptors on the surface of graphene.

We prepared several graphene samples by the method of micromechanical cleavage of natural graphite with a scotch tape on top of 300 nm silicion oxide on top of heavily p doped silicon. After depositing the graphene samples, we washed out the samples using acetone followed by iso-propanol in order to clean the samples from the glue of the scotch tape. The in-situ Raman experiment were done by placing the sample inside a heater stage with a optical window under gas flow (N_2 or ultra pure Argon).

Figure D.2 shows the G band position of monolayer graphene as a function of temperature. We can divide into three different regimes for the G band frequency data as a function of temperature: (I) the G band softens for increasing temperature until ~ 180°C; (II) the G band hardens with increasing temperature above ~ 180°C; (III) the G band hardens by lowering the temperature. This thermal cycle presents an hysteresis, since the G band final frequency is blueshifted with respect to its initial value.

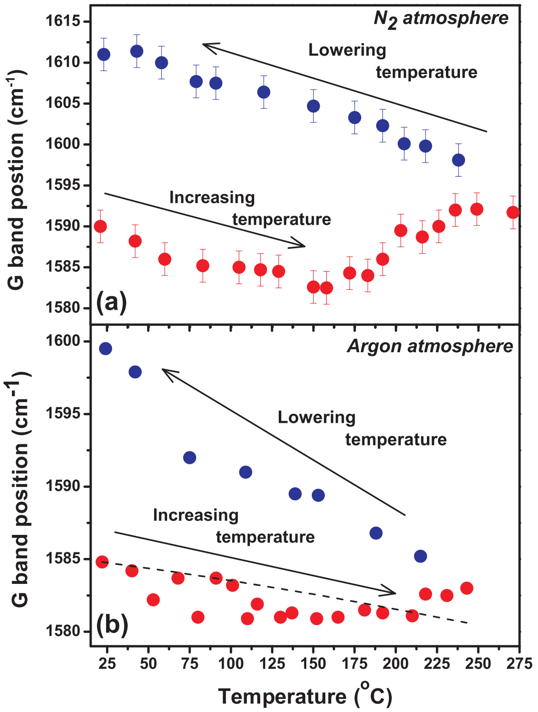

Figure D.2: (color online) G band position as a function of temperature for a monolayer graphene sample under (a) nitrogen and (b) argon gas flow. The red circles represents the heating and the blue circles the cooling.

The first regime can be understood in terms of anharmonic effects of the electron-phonon and phonon-phonon couplings in graphene. Although there is a thermal contraction in graphene by increasing temperature, the contribution of electron-phonon and phonon-phonon interactions softens the G band with temperature. The dashed line in Fig. D.2(b) corresponds to the calculation done by Bonini *et al.* [131], which takes into account these anharmonic terms, and it is in agreement with our experimental findings. Regime (I) continues until temperatures near 180 °C, the G band starts to harden with increasing temperatures [regime (II)]. Beyond anharmonic effects due to temperature, the G band frequency is also very sensitive to doping of the sample due strong electron-phonon coupling near the Γ point in first Brillouin zone of graphene. For a monolayer graphene sample in which the Fermi level is away from the Dirac point, the G band frequency is blueshifted with respect to the undoped case. In regime (II) the G band start to hardens its frequency probably due to water desorption in the sample and further doping due to organic solvents present in sample preparation. In this regime the frequency of the G band is more sensitive to doping than by the effect of temperature itself. In the third and last regime, the temperature of the sample is decreased and the G band frequency, which starts to hardens. The final measurement corresponding to room temperature the G band frequency is blueshifted with respect to the starting *undoped* sample. This hysteresis cycle represents the doping of the sample when temperature is increased.

In order to better understand this effect we are now analyzing more data from the G′ band in order to identify if the doping occurs from electrons or holes [132].

APPENDIX E

Resonance Raman study of polyynes encapsulated in single wall carbon nanotubes

Polyyne molecules are linear carbon chains, with alternating single and triple bonds, and terminated by end atoms or groups. This kind of structure is of fundamental interest since it is the perfect example of a purely sp-hybridized carbon structure, which is expected to show a completely different physics than the more common sp^2 and sp^3 structures. Moreover, they represent the ultimate linear wire, which may not only transport charge between its ends through their π electrons, but also serve as a perfect playground for studying the strong and unique effects of electron correlations in one dimensional systems. Their study has been a very attractive field of research since the pioneering work of Kroto *et al.* [3] who discovered the fullerenes in the search of these linear molecules in space. However, the investigation of the physical and chemical properties of these linear molecules is not an easy task, since they are very unstable at normal temperature and atmosphere conditions [133, 134].

Hydrogen-ended polyyne molecules, $H(-C{\equiv}C-)_nH$ or just $C_{2n}H_2$, are the simplest polyyne molecules and have been produced recently by techniques of graphite ablation in organic solvents [135, 136]. Very recently, Nishide *et al.*[137] were able to encapsulate $C_{2n}H_2$ polyynes ($n = 5$) inside single-wall carbon nanotubes (SWNTs) and have shown that these molecules can be stable even at high temperatures, up to 350 °C. Trapped inside SWNTs these molecules can be carefully studied for a complete understanding of their electronic structure, a crucial step towards future applications of these systems.

Linear chains of carbon atoms have also been observed inside multi-wall carbon nanotubes [138] and on double-wall carbon nanotubes heat-treated at high temperatures [139]. All these sp-hybridized systems exhibit Raman features in the range $1800-2100$ cm^{-1}, depending on the chain size and environment [140, 137, 141], and if their ends are free or fixed to the nanotubes. Recently, Fantini et al. [141] performed a detailed resonance Raman study of linear chain of carbon atoms formed during the coalescence of double wall carbon nanotubes, and showed that the intensity of the Raman feature associated with this chain is strongly dependent on the laser energy used in the experiment, with a peak around 2.2 eV [141].

In this work we present a resonance Raman study of two polyyne molecules ($C_{10}H_2$ and $C_{12}H_2$) encapsulated inside single wall carbon nanotubes (SWNT). By using many different laser lines covering the whole visible range, we show that the main Raman features associated with stretching modes of the linear chains in both samples ($C_{10}H_2$@SWNT and $C_{12}H_2$@SWNT) are strongly enhanced around 2.1 eV, whereas the optical absorption observed when these molecules are dispersed in isotropic medium [140] or in the gas phase [142] occur at much higher energy (4.9 and 4.5 eV for $C_{10}H_2$ and $C_{12}H_2$, respectively). The results are interpreted here in terms of dipole-forbidden transitions of the polyynes that become active due to a symmetry breaking when the molecules are encapsulated.

The $C_{10}H_2$ and $C_{12}H_2$ polyynes were made by laser ablation of graphite particles in n-hexane, and the molecules with different sizes were separated by high-performance liquid chromatography (HPLC). More detais on the sample preparation can be found in Ref. [135]. The SWNTs were prepared by laser ablation of metal-containing carbon rod, with a mean diameter distribution of 1.3 nm. For encapsulating the polyynes inside the SWNTs, a piece of nanotube film was dipped inside the separated polyyne dispersion in n-hexane and kept at 80 °C for 24 hours under vacuum [137]. Raman scattering experiments were performed at room temperature using a triple monochromator micro-Raman spectrometer (DILOR XY). The laser power used was 1 mW with a spot diameter of ~ 1 μm using a 80X objective. We used five different laser lines of an Ar-Kr laser (1.92 eV, 2.18 eV, 2.41 eV, 2.54 eV and 2.71 eV) and 15 laser lines from a dye laser ranging from 1.9 to 2.3 eV.

Figure E.1 shows the Raman spectra, recorded using the 2.18 eV (568 nm) laser line, of the carbon nanotube (SWNT) pristine sample (spectrum at the bottom of the figure) and of the two samples of $C_{10}H_2$ and $C_{12}H_2$ polyynes encapsulated

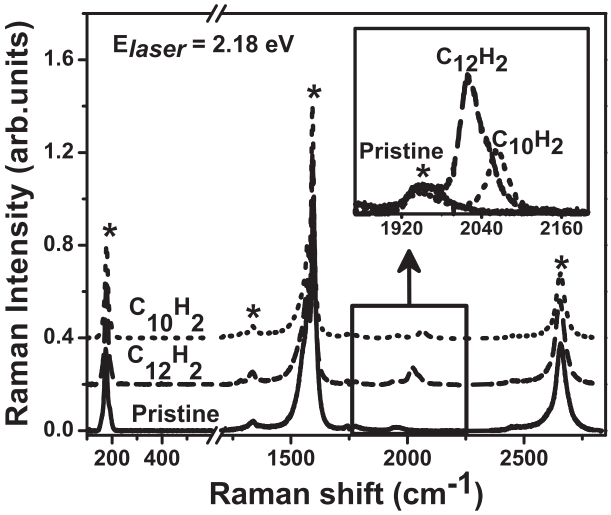

Figure E.1: Raman spectra with 2.18 eV excitation energy for the different samples: $C_{10}H_2$@SWNT(red and top spectra), $C_{12}H_2$@SWNT(blue and middle spectra) and pristine SWNT (black and bottom spectra). The inset shows a larger view of the P bands for the two polyyne samples. The asterisks indicate the most prominent Raman features of SWNTs

in SWNTs. All peaks in this figure marked by asterisks are associated with the most prominent Raman features of the carbon nanotubes [143], such as the radial breathing mode (RBM) around 200 cm^{-1} and the D, G and G$'$ peaks around 1350, 1590 and 2700 cm^{-1}, respectively. The bands in the range 2000-2100 cm^{-1}, denoted here by P bands, are associated with the stretching vibrations of the polyynes inside the nanotubes.

In the case of the $C_{10}H_2$@SWNT sample, the P band is composed by just one peak, centered at 2066 cm^{-1}, and it is associated with the ν_3 vibrational mode of the polyyne chain [144]. The P band of the $C_{12}H_2$@SWNT sample is clearly composed by two peaks, centered at 2020 cm^{-1} and 2050 cm^{-1}, and they have been ascribed to the ν_4 and ν_3 vibrational modes of the $C_{12}H_2$ molecule inside the carbon nanotube [144]. As a general trend, the frequency of the main Raman feature of the $C_{2n}H_2$ polyynes is inversely proportional to the number $2n$ of carbon atoms in chain [140]. These frequencies also depend on the environment of the polyyne. Nishide et al. [137] have shown that the frequency of the P-bands for the $C_{10}H_2$@SWNT and $C_{12}H_2$@SWNT samples are downshifted with respect to those of the $C_{10}H_2$ and $C_{12}H_2$ polyynes dispersed in n-hexane (57 cm^{-1} for $C_{10}H_2$, and

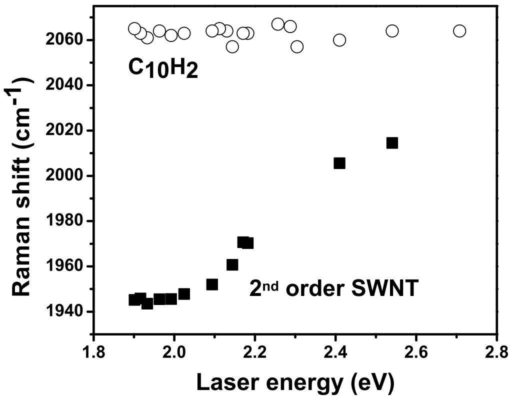

Figure E.2: The P band frequency for the $C_{10}H_2$(open circles) and the 2^{nd} order SWNT peak (closed square) as a function of laser energy.

33 cm^{-1}(ν_4) and 47 cm^{-1}(ν_3 for $C_{12}H_2$).

In this work, we will focus on the resonance behavior of the P band, by inspecting the laser energy dependence of this band. We recorded 18 spectra similar to those of Fig. E.1 by changing the laser energy between 1.92 and 2.71 eV and, in the following, we will discuss the modifications that are observed in the P-band when we change the laser energy. The inset of Fig. E.1 shows the detailed spectra of the P band for $C_{10}H_2$@SWNT and $C_{12}H_2$@SWNT as well as the spectrum of the pristine SWNT sample in this frequency range. Notice that the spectrum of the pristine sample also exhibits a weak band around 1950 cm^{-1}, which is a common feature to all kind of graphitic (sp^2) materials and that is ascribed to a second-order Raman process involving the combination of two phonons within the interior of the 1st Brillouin zone of graphite [145]. Since these second-order features are known to exhibit a strong dispersion when the laser energy is changed, we plot in Fig. E.2 the laser energy dependence of the frequency of the the Raman peaks of $C_{10}H_2$@SWNT in the range 1900 to 2100 cm^{-1}. Notice that the frequency of the second-order feature strongly depends on the laser energy, whereas the frequency of the P band remains constant by changing the laser energy. A similar behavior was observed for the $C_{12}H_2$@SWNT sample. The non-dispersive behavior of the P band confirms that it is a first-order Raman feature, and necessarily associated with the sp-carbon linear chain.

In order to analyze the laser energy dependence of the P band intensity, all spectra were normalized to keep the intensity of the *G* band of the carbon nanotube constant. Due to the large number of nanotube species in the sample, the G-band intensity is not expected to depend significantly on E_{laser} and, thus, it can be considered as a good internal parameter for normalization. Fig. E.3 shows the laser energy dependence of the intensity of the P band for the $C_{10}H_2$@SWNT and $C_{12}H_2$@SWNT samples. There is a clear resonance enhancement in the intensity of these bands between 2.0 and 2.3 eV, the maximum occurring at approximately 2.14 eV and 2.10 eV, for the $C_{10}H_2$@SWNT and $C_{12}H_2$@SWNT samples, respectively.

The electronic transitions of different $C_{2n}H_2$ polyynes in gas phase[142] and in neon matrixes [146] have been measured by absorption spectroscopy. The strong UV absorption observed for the $C_{2n}H_2$ molecules with a small number of carbon atoms was interpreted based on quantum chemistry models, as arising from the transition between the ground state and the first dipole-allowed transition of the molecule. The energy of this electronic transition was observed to increase with decreasing value of n [146]. From Ref. [142], one can estimate the gas phase values for the UV transition energy to be 5.4 eV for $C_{10}H_2$ and 5.0 eV for $C_{12}H_2$.

Tabata et al. [140] reported recently the UV absorption spectra of different $C_{2n}H_2$ polyynes dispersed in n-hexane and, for each value of n, the spectrum was composed by peaks separated by the energy of one stretching mode of the linear chain (a vibronic spectrum). In the case of the $C_{10}H_2$ and $C_{12}H_2$ molecules, the longest wavelength peak observed in the UV absorption spectra, and that corresponds to a zero-phonon process, was observed at 4.90 eV and 4.50 eV for the $C_{10}H_2$ and $C_{12}H_2$ polyynes, respectively. Notice the strong redshift due to solvent effects, as compared to the gas phase transitions. In a recent resonance Raman study of polyynes in solution, Wakabayashi *et al.* [147] showed that the intensity of the Raman peaks of the polyynes increases significantly when the Raman spectra is recorded with UV lines in the vicinity of the UV absorptions of these molecules.

A possible explanation for the resonance behavior observed here in the visible range can be related to resonances with lower energy electronic transitions in the polyynes that are not allowed when the molecule is surrounded by an isotropic medium. When the polyyne is encapsulated in the interior of a single wall carbon nanotube, the axial symmetry is broken due to the interaction with the nanotube wall, and new electric dipole electronic transitions can be activated in this case.

In order to test this hypothesis, we perform time-dependent density functional

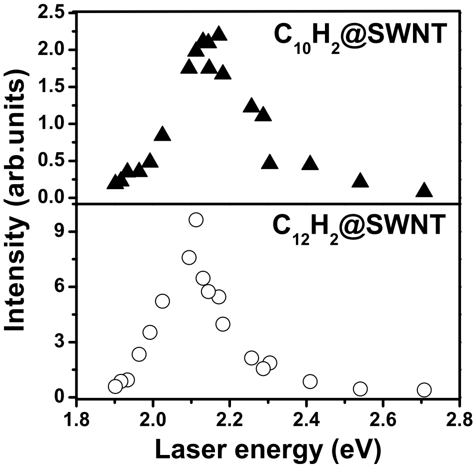

Figure E.3: Raman intensity of the P bands for $C_{10}H_2$(closed triangles) and for the $C_{12}H_2$(open circles) as a function of laser excitation energy.

theory (TDDFT) [148] and semi-empirical ZINDO [149] calculations of the optical spectra of $C_{10}H_2$ and $C_{12}H_2$. Since the electronic structure of these molecules critically depends on the degree of carbon-carbon bond-length alternation (BLA) along the chain [150], we take extra care in determining the molecular geometries. It is well known that pure DFT functionals do not describe the BLA of such systems in an accurate way. Usually, hybrid DFT methods (mixing with exact exchange) perform better, and the BLA typically increases with the amount of exact exchange [150]. We perform geometry optimization with two hybrid schemes: PBE1PBE [151], which mixes 25% of exact exchange, and BHandHLYP [152], which mixes 50%. BHandHLYP describes well the BLA of the related systems polyacetylene and polydiacetylene [150]. We use the Gaussian03 program [152] with the 6-31G* Gaussian-type basis sets.

The nature and symmetries of the excited states in the polyynes can be understood in a simple way. Both the HOMO and the LUMO are doubly-degenerate, transforming according to the Π_g and Π_u representations of the $D_{\infty h}$ point group, respectively. They correspond to bonding and anti-bonding combinations of p_x and p_y orbitals at the triple bonds. If we restrict our reasoning to single excitations within these four orbitals, the excited states should transform as $\Pi_g \otimes \Pi_u = \Sigma_u^- + \Sigma_u^+ + \Delta_u$. From these states, only Σ_u^+ is dipole-allowed, the others being forbidden (dark) states.

Our results are summarized in Table E.1. As expected, BHandHLYP gives a larger BLA than PBE1PBE, and the optical transition energies are strongly dependent on geometry. Also, even for a given geometry, there is substantial scattering in the theoretical transition energies, indicating the degree of uncertainty at this level of calculation. We find the dipole-allowed states with Σ_u^+ symmetry between 5.2 eV and 5.7 eV for $C_{10}H_2$ and between 4.7 eV and 5.3 eV for $C_{12}H_2$, depending on the BLA. These values compare rather well to the gas phase transition energies [142]. The dark states with Σ_u^- and Δ_u symmetries are found at much lower energies: from 2.2 eV to 3.3 eV for $C_{10}H_2$ and from 2.0 to 3.0 eV for $C_{12}H_2$. These values are very close to our measured resonances in encapsulated polyynes[1]. Notice the huge ($\sim$ 2.5 eV) splitting, due to Coulomb interactions, between bright and dark many-electron states which are essentially composed by different linear combinations of the same set of single-particle states. For comparison, similar bright-dark splittings in carbon nanotubes are of the order of tens of meV [153]. Moreover, the Σ_u^--Δ_u energy splittings are roughly 0.1-0.3 eV for the two molecules, also in good agreement with our resonance width.

We therefore propose that our observed resonances between 2.0 and 2.3 eV are due to the dipole-forbidden Σ_u^- and Δ_u states of the polyynes. These transitions are made "bright" due to a lowering of the site symmetry from $D_{\infty h}$ to C_{2h} when the encapsulated molecules are displaced from the central axis of the nanotube. Indeed, for the diameter range of nanotubes considered in our study, there is plenty of room for the polyynes to adopt an off-center position, close to the inner wall of the tube, due to van der Waals attraction. Such behavior has been observed in total energy calculations of polyyne@SWNT systems [154].

In summary, we have measured the resonance Raman spectra of two polyyne molecules ($C_{10}H_2$ and $C_{12}H_2$) encapsulated inside SWNTs with many different laser excitation energies in the range of the visible. We observed that the intensity of the Raman band associated with the stretching mode of the linear chain inside the nanotube is strongly enhanced for laser energies around 2.1 eV. This energy value is much lower than the absorption peaks of the $C_{10}H_2$ and $C_{12}H_2$ polyynes dispersed in organic solvents, (4.9 eV and 4.5 eV, respectively), or in the gas

---

[1] The agreement can be even better if one considers that substantial redshifts in the optical transition energies (with respect to the gas phase or theory) can occur when the molecule is immersed in a solution or another environment. For instance, optical transitions of polyynes in methanol are shifted roughly -0.5 eV with respect to the gas phase [142].

Table E.1: Bond-length alternation (BLA) in the center of the chain (in Å) and optical transition energies (in eV) for $C_{10}H_2$ and $C_{12}H_2$. ”Geometry” indicates the geometry optimization method.

Molecule	Geometry	BLA	TDDFT			ZINDO		
			Σ_u^-	Δ_u	Σ_u^+	Σ_u^-	Δ_u	Σ_u^+
$C_{10}H_2$	PBE1PBE	0.116	2.76	2.89	5.20	2.20	2.50	5.50
	BHandHLYP	0.143	3.10	3.25	5.74	2.46	2.76	5.68
$C_{12}H_2$	PBE1PBE	0.109	2.48	2.59	4.65	2.03	2.31	5.07
	BHandHLYP	0.140	2.87	3.00	5.24	2.31	2.60	5.26

phase (5.4 eV and 5.0 eV, respectively). The resonance Raman behavior observed here is interpreted in terms of dipole-forbidden transitions of the polyynes that are made ”bright” due to a breaking of $D_{\infty h}$ site symmetry when the molecules are encapsulated. Our combined experiment-theory determination of a huge ($\sim$ 2.5 eV) energy splitting between bright and dark excited states sets the scale, for the first time, of the strong Coulomb effects in the most extreme one-dimensional system, a linear chain.

Appendix F

List of publications

- D. L. Mafra, G. Samsonidze, L. M. Malard, D. C. Elias, J. C. Brant, F. Plentz and M. A. Pimenta. Determination of LA and TO phonon dispersion relations of graphene near the Dirac point by double resonance Raman scattering. Physical Review. B, Condensed Matter and Materials Physics, v. 76, p. 233407, 2007.

- L. M. Malard, J. Nilsson, D. C. Elias, J. C. Brant, F. Plentz, E. S. Alves, A. H. Castro Neto and M. A. Pimenta. Probing the electronic structure of bilayer graphene by Raman scattering. Physical Review. B, Condensed Matter and Materials Physics, v. 76, p. 201401(R), 2007.

- L. M. Malard, D. C. Elias, E. S. Alves, M. A. Pimenta. Observation of Distinct Electron-Phonon Couplings in Gated Bilayer Graphene. Physical Review Letters, v. 101, p. 257401, 2008.

- L. M. Malard, J. Nilsson, D. L. Mafra, D. C. Elias, J. C. Brant, F. Plentz, E. S. Alves, A. H. Castro Neto, M. A. Pimenta. Electronic properties of bilayer graphene probed by Resonance Raman Scattering. Physica Status Solidi. B, Basic Research, p. NA-NA, 2008.

- L. M. Malard, M. H. D. Guimarães, D. L. Mafra, M. S. C. Mazzoni and A. Jorio. Group-theory analysis of electrons and phonons in N-layer graphene systems. Physical Review. B, Condensed Matter and Materials Physics, v. 79, p. 125426, 2009.

- L. M. Malard, D. L. Mafra, S. K. Doorn and M. A. Pimenta . Resonance Raman scattering in graphene: probing phonons and electrons. Solid State Communications, 2009.

- L. M. Malard, M. A. Pimenta, G. Dresselhaus and M. S. Dresselhaus . Raman Spectroscopy in Graphene. Physics Reports, v. 473, p. 51-87, 2009.

Bibliography

[1] McClure. *Phys. Rev.*, 108:612, 1957.

[2] J. C. Slonczewski and P. R. Weiss. *Phys. Rev.*, 109:272, 1958.

[3] H. W. Kroto, J. R. Heath, S. C. O'Brien, R. F. Curl and R. E. Smalley. *Nature*, 318:162, 1985.

[4] S. Ijima. *Nature*, 354:56, 1991.

[5] A. K. Geim and K. S. Novoselov. *Nature Mater.*, 6:183, 2007.

[6] N. D. Mermin. *Phys. Rev.*, 176:250, 1968.

[7] J. C. Meyer, A. K. Geim, M. I. Katsnelson, K. S. Novoselov, T. J. Booth, S. Roth. *Nature*, 446:60, 2007.

[8] K. S. Novoselov, A. K. Geim, S. V. Morozov, D. Jiang, M. I. Katsnelson, I. V. Grigorieva, S. V. Dubonos, and A. A. Firsov. *Science*, 306:666, 2004.

[9] K. S. Novoselov, D. Jiang, F. Schedin, T. J. Booth, V. V. Khotkevich, S. V. Morozov and A. K. Geim. *PNAS*, 102:10451, 2005.

[10] K. S. Novoselov, A. K. Geim, S. V. Morozov, D. Jiang, M. I. Katsnelson, I. V. Grigorieva, S. V. Dubonos, and A. A. Firsov. *Nature*, 438:197, 2005.

[11] Y. Zhang, Y. W. Tan, H. L. Stormer, and P. Kim. *Nature*, 438:201, 2005.

[12] A. K. Geim. *Science*, 324:1530, 2009.

[13] A. H. Castro Neto, F. Guinea, N. M. R. Peres, K. S. Novoselov and A. K. Geim. *Review of Modern Physics*, 81:109, 2009.

[14] M. I. Katsnelson, K. S. Novoselov and A. K. Geim. *Nature Physics*, 2:620, 2006.

[15] M. Fujita, K. Wakabayashi, K. Nakada and K. Kusakabe. *J. Phys. Soc. Jpn.*, 65:1920, 1996.

[16] K. Nakada, M. Fujita, G. Dresselhaus and M.S. Dresselhaus. *Phys. Rev. B*, 54:17954, 1996.

[17] Young-Woo Son, M. L. Cohen and S. G. Louie. *Phys. Rev. Lett.*, 97:216803, 2006.

[18] D. C. Elias, R. R. Nair, T. M. G. Mohiuddin, S. V. Morozov, P. Blake, M. P. Halsall, A. C. Ferrari, D. W. Boukhvalov, M. I. Katsnelson, A. K. Geim and K. S. Novoselov. *Science*, 323:610, 2009.

[19] K. S. Novoselov, E. McCann, S. V. Morozov, V. I. Fal'ko, M. I. Katsnelson, U. Zeitler, D. Jiang, F. Schedin and A. K. Geim. *Nature Physics*, 2:177, 2006.

[20] E. McCann. *Phys. Rev. B*, 74:161403, 2007.

[21] E. McCann and V. I. Fal´ko. *Phys. Rev. Lett.*, 96:086805, 2006.

[22] J. Nilsson, A. H. Castro Neto, F. Guinea, and N. M. R. Peres. *Phys. Rev. B*, 76:165416, 2007.

[23] J. B. Oostinga, H. B. Heersche, X. L. Liu, A. F. Morpurgo and L. M. K. Vandersypen. *Nature Materials*, 7:151, 2008.

[24] Y. Zhang, Tsung-Ta Tang, C. Girit, Z. Hao, M. C. Martin, A. Zettl, M. F. Crommie, Y. Ron Shen, F. Wang. *Nature*, 459:820, 2009.

[25] D. A. Dikin *et al.* *Nature*, 448:457, 2007.

[26] Y. Hernandez *et al.* *Nature Nanotechnology*, 3:563, 2008.

[27] A. Reina *et al.* *Nano Lett.*, 9:30, 2009.

[28] C. Berger, Z. Song, T. Li, X. Li, A. Y. Ogbazghi, R. Feng, Z. Dai, A. N. Marchenkov, E. H. Conrad, P. N. First, W. A. de Heer. *J. Phys. Chem. B*, 108:19912, 2004.

[29] C. Berger, Z. M. Song, X. Lee, Xiaosong Wu, N. Brown, C. Naud, D. Mayou, T. Li, J. Hass, A. N. Marchenkov, E. H. Conrad, P. N. First and W. A. de Heer. *Science*, 312:1191, 2006.

[30] K. V. Emtsev *et al.* *Nature Materials*, 8:203, 2009.

[31] C. V. Raman and K. S. Krishnan. *Nature*, 121:501, 1928.

[32] K. Sugihara I. L. Spain M. S. Dresselhaus, G. Dresselhaus and H. A. Goldberg. *Graphite Fibers and Filaments*, volume 5 of *Springer Series in Materials Science.* Springer-Verlag, Berlin, 1988.

[33] G. Dresselhaus R. Saito and M. S. Dresselhaus. *Physical Properties of Carbon Nanotubes.* Imperial College Press, London, 1998.

[34] F. Tuinstra and J. L. Koenig. *J. Chem. Phys.*, 53:1126, 1970.

[35] F. Tuinstra and J. L. Koenig. *J. Composite Materials*, 4:492, 1970.

[36] P. Lespade, A. Marchand, M. Couzi and F. Cruege. *Carbon*, 22:375, 1984.

[37] M. S. Dresselhaus, G. Dresselhaus, R. Saito, and A. Jorio. *Physics Reports*, 409:47, 2005.

[38] A. C. Ferrari, J. C. Meyer, V. Scardaci, C. Casiraghi, M. Lazzeri, F. Mauri, S. Piscanec, D. Jiang, K. S. Novoselov, S. Roth, and A. K. Geim. *Phys. Rev. Lett.*, 97:187401, 2006.

[39] A. Gupta, G. Chen, P. Joshi, S. Tadigadapa, and P. C. Eklund. *Nano Lett.*, 6:2667, 2006.

[40] D. Graf, F. Molitor, K. Ensslin, C. Stampfer, A. Jungen, C. Hierold and L. Wirtz. *Nano Lett.*, 7:238, 2007.

[41] T. Ando. *J. Phys. Soc. Jpn.*, 75:124701, 2006.

[42] M. Lazzeri *et al.* *Phys. Rev. B*, 73:155426, 2006.

[43] S. Pisana, M. Lazzeri, C. Casiraghi, K. S. Novoselov, A. K. Geim, A. C. Ferrari and F. Mauri. *Nature Mater.*, 6:198, 2007.

[44] J. Yan, Y. Zhang, P. Kim and A. Pinczuk. *Phys. Rev. Lett.*, 98:166802, 2007.

[45] A. Das, S. Pisana, B. Chakraborty, S. Piscanec, S. K. Saha, U. V. Waghmare, K. S. Novoselov, H. R. Krishnamurthy, A. K. Geim, A. C. Ferrari and A. K. Sood. *Nature Nanotech.*, 3:210, 2008.

[46] L. M. Malard, J. Nilsson, D. C. Elias, J. C. Brant, F. Plentz, E. S. Alves, A. H. Castro Neto, and M. A. Pimenta. *Phys. Rev. B*, 76:201401, 2007.

[47] D. L. Mafra, G. Samsonidze, L. M. Malard, D. C. Elias, J. C. Brant, F. Plentz, E. S. Alves, and M. A. Pimenta. *Phys. Rev. B*, 76:233407, 2007.

[48] R. Saito A. Jorio and M. S. Dresselhaus. *Raman spectroscopy in carbon materials.* in preparation, 2009.

[49] D. L. Mafra, L. M. Malard, S. K. Doorn, H. Htoon, J. Nilsson, A. H. Castro Neto, M. A. Pimenta . *arXiv:0907.3322*, 2009.

[50] T. M. G. Mohiuddin *et al.* *Phys. Rev. B*, 79:205433, 2009.

[51] M. Huang, H. Yan, C. Chen, D. Song, T. F. Heinz and J. Hone. *PNAS*, 106:7304, 2009.

[52] Jun Yan, Erik A. Henriksen, Philip Kim, and Aron Pinczuk. *Phys. Rev. Lett.*, 101:136804, 2008.

[53] L. M. Malard, D. C. Elias, E. S. Alves and M. A. Pimenta. *Phys. Rev. Lett.*, 101:257401, 2008.

[54] A. Das *et al.* *Phys. Rev. B*, 79:155417, 2009.

[55] C. Faugeras, M. Amado, P. Kossacki, M. Orlita, M. Sprinkle, C. Berger, W.A. de Heer, M. Potemski. *arXiv:0907.5498*, 2009.

[56] B. Partoens and F. M. Peeters. *Phys. Rev. B*, 74:075404, 2006.

[57] L. M Malard, M. H. D. Guimaraes, D. L. Mafra, M. S. C. Mazzoni and A. Jorio. *Phys. Rev. B*, 79:125426, 2009.

[58] Ge. G. Samsonidze, E. B. Barros, R. Saito, J. Jiang, G. Dresselhaus, and M. S. Dresselhaus. *Phys. Rev. B*, 75:155420, 2007.

[59] J. Maultzsch, S. Reich, C. Thomsen, H. Requardt, and P. Ordejon. *Phys. Rev. Lett.*, 92:075501, 2004.

[60] K. A. Wang, A. M. Rao, P. C. Eklund, M. S. Dresselhaus, and G. Dresselhaus. *Phys. Rev. B*, 48:11375, 1993.

[61] J. Jiang, R. Saito, Ge. G. Samsonidze, S. G. Chou, A. Jorio, G. Dresselhaus, and M. S. Dresselhaus. *Phys. Rev. B*, 72:235408, 2005.

[62] P. L. Taylor and O. Heinonen. *Quantum approach to condesed matter physics.* Cambridge University Press, 2002.

[63] T. Ando. *J. Phys. Soc. Jpn.*, 75:024707, 2006.

[64] A. H. Castro Neto and F. Guinea . *Phys. Rev. B*, 75:045404, 2007.

[65] W. Kohn. *Phys. Rev. Lett.*, 2:393, 1959.

[66] S. Piscanec, M. Lazzeri, M. Mauri, A. C. Ferrari, and J. Robertson. *Phys. Rev. Lett.*, 93:185503, 2004.

[67] E. V. Zarochentsev V. G. Baryakhtar and E. P. Troitskaya. *Theory of adiabatic potential and atomic properties of simple metals.* Gordon and Breach Science Publishers, 1999.

[68] T. Ando. *J. Phys. Soc. Jpn.*, 76:104711, 2007.

[69] J. C. Tsang *et al. Nature Nanotech.*, 2:725, 2007.

[70] J. H. Davies. *The physics of low-dimensional semiconductors.* Cambridge University Press, Cambridge, 1998.

[71] B. Diu C. Cohen-Tannoudji and F. Laloë. *Quantum mechanics.* John Wiley and Sons, New York, 1977.

[72] A. F. R. de Toledo Piza. *Mecânica quântica.* EDUSP, São Paulo, 2003.

[73] A. Grüneis, R. Saito, Ge. G. Samsonidze, T. Kimura, M. A. Pimenta, A. Jorio, A. G. Souza Filho, G. Dresselhaus, and M. S. Dresselhaus. *Phys. Rev. B*, 67:165402, 2003.

[74] L. G. Cançado, M. A. Pimenta, R. A. Neves, G. Medeiros-Ribeiro, T. Enoki, Y. Kobayashi, K. Takai, K. Fukui, M. S. Dresselhaus, R. Saito, and A. Jorio. *Phys. Rev. Lett.*, 93:047403, 2004.

[75] L. G. Cançado, M. A. Pimenta, B. R. A. Neves, M. S. S. Dantas, and A. Jorio,. *Phys. Rev. Lett.*, 93:247401, 2004.

[76] P. Y. Yu and M. Cardona. *Fundamentals of Semiconductors: Physics and Materials Properties*. Springer-Verlag, Heidelberg, 2005.

[77] G. Dresselhaus M. S. Dresselhaus and A. Jorio. *Group Theory: Application to the Physics of Condensed Matter*. Springer, Berlin, 2008.

[78] J. Jiang, R. Saito, A. Grüneis, S. G. Chou, Ge. G. Samsonidze, A. Jorio, G. Dresselhaus, and M. S. Dresselhaus. *Phys. Rev. B*, 71:205420, 2005.

[79] J. Maultzsch, S. Reich, C. Thomsen. *Phys. Rev. B*, 70:155403, 2004.

[80] M. Ramsteiner and J. Wagner. *Appl. Phys. Lett.*, 51:1355, 1987.

[81] I. Pócsik, M. Hundhausen, M. Koós, and L. Ley. *Journal of Non-Crystalline Solids*, 227:1083, 1998.

[82] M. J. Matthews, M. A. Pimenta, G. Dresselhaus, M. S. Dresselhaus, and M. Endo. *Phys. Rev. B*, 59:R6585, 1999.

[83] A. V. Baranov, A. N. Bekhterev, Y. S. Bobovich, and V. I. Petrov. *Opt. Spectrosk.*, 62:1036, 1987.

[84] C. Thomsen and S. Reich. *Phys. Rev. Lett*, 85:5214, 2000.

[85] R. Saito, A. Jorio, A. G. Souza Filho, G. Dresselhaus, M. S. Dresselhaus and M. A. Pimenta. *Phys. Rev. Lett.*, 88:027401, 2002.

[86] G. Ge. Samsonidze. *Photophysics of Carbon Nanotubes*. PhD thesis, Department of Electrical Engineering and Computer Science, Massachusetts Institute of Technology, 2007.

[87] R. Saito, A. Grüneis, Ge. G. Samsonidze, V. W. Brar, G. Dresselhaus, M. S. Dresselhaus, A. Jorio, L. G. Cançado, C. Fantini, M. A. Pimenta, and A. G. Souza Filho. *New Journal of Physics*, 5:157, 2003.

[88] C. Thomsen, S. Reich and J. Maultzsch. *Phil. Trans. R. Soc. Lond. A*, 362:2337, 2004.

[89] S. Reich and C. Thomsen. *Philos. Trans. Royal Society*, 362:2271, 2004.

[90] L. G. Cançado. *Raman spectroscopy of nanographites.* PhD thesis, Dep. de Física, UFMG, 2006.

[91] D. L. Mafra. Dispersão de fônons na vizinhaça do ponto de dirac do grafeno por espalhamento raman. Master's thesis, Dep. de Física, UFMG, 2008.

[92] B. Partoens and F. M. Peeters. *Phys. Rev. B*, 74:075404, 2006.

[93] L. G. Cançado, A. Reina, J. Kong and M. S. Dresselhaus. *Phys. Rev. B*, 77:245408, 2008.

[94] L. M. Malard, M. A. Pimenta, G. Dresselhaus, M. S. Dresselhaus. *Physics Reports*, 473:51, 2009.

[95] L. G. Cançado, M. A. Pimenta, R. Saito, A. Jorio, L. O. Ladeira, A. Grüneis, A. G. Souza-Filho, G. Dresselhaus and M. S. Dresselhaus. *Phys. Rev. B*, 66:035415, 2002.

[96] P. Blake, E. W. Hill, A. H. Castro Neto, K. S. Novoselov, D. Jiang, R. Yang, T. J. Booth, and A. K. Geim . *Applied Physics Letters*, 91:063124, 2007.

[97] R. R. Nair, P. Blake, A. N. Grigorenko, K. S. Novoselov, T. J. Booth, T. Stauber, N. M. R. Peres, and A. K. Geim. *Science*, 320:1308, 2008.

[98] G. R. Fowles. *Introduction to modern optics.* Dover Publications, New York, 1989.

[99] D. J. Griffiths. *Introduction to electrodynamics.* Prentice Hall, Upper Saddle River, 1999.

[100] Çağlar Ö. Girit and A. Zettl. *App. Phys. Lett.*, 91:193512, 2007.

[101] N. W. Ashcroft and N. D. Mermin. *Solid State Physics.* Saunders College Publishing, Fort Worth, 1989.

[102] T. Ohta, A. Bostwick, T. Seyller, K. Horn, and E. Rotenberg. *Science*, 313:951, 2006.

[103] E. V. Castro, K. S. Novoselov, S. V. Morozov, N. M. R. Peres, J. M. B. Lopes dos Santos, J. Nilsson, F. Guinea, A. K. Geim, and A. H. Castro Neto. *Phys. Rev. Lett.*, 99:216802, 2007.

[104] W. Kohn and L. J. Sham. *Phys. Rev.*, 140:A1133, 1965.

[105] P. Ordejón, E. Artacho, and J. M. Soler. *Phys. Rev. B*, 53:R10441, 1996.

[106] J. M. Soler, E. Artacho, J. D. Gale, A. Garcia, J. Junquera, P. Ordejón, and D. Sánchez-Portal. *J. Phys.: Condens. Matter*, 14:2745, 2002.

[107] T. Ohta, A. Bostwick, J. L. McChesney, T. Seyller, K. Horn, and E. Rotenberg. *Phys. Rev. Lett.*, 98:206802, 2007.

[108] M. Koshino and E. McCann. *Phys. Rev. B*, 79:125443, 2009.

[109] S. Latil and L. Henrard. *Phys. Rev. Lett.*, 97:036803, 2006.

[110] J. L. Mañes, F. Guinea, and M. A. H. Vozmediano. *Phys. Rev. B*, 75:155424, 2007.

[111] C. Casiraghi, S. Pisana, K. S. Novoselov, A. K. Geim, and A. C. Ferrari. *Appl. Phys. Lett.*, 91:233108, 2007.

[112] S. K. Saha, U. V. Waghmare, H. R. Krishnamurthy, and A. K. Sood. *Phys. Rev. B*, 78:165421, 2008.

[113] J. W. Jiang, H. Tang, B. S. Wang, and Z. B. Su. *Phys. Rev. B*, 77:235421, 2008.

[114] C. Fantini, A. Jorio, M. Souza, M. S. Strano, M. S. Dresselhaus and M. A. Pimenta. *Phys. Rev. Lett.*, 93:147406, 2004.

[115] A. C. Ferrari and J. Robertson. *Phys. Rev. B*, 64:075414, 2001.

[116] L. M. Malard, D. Nishide, L. G. Dias, Rodrigo B. Capaz, A. P. Gomes, A. Jorio, C. A. Achete, R. Saito, Y. Achiba, H. Shinohara and M. A. Pimenta. *Phys. Rev. B*, 76:233412, 2007.

[117] R. A. Jishi, M. S. Dresselhaus, G. Dresselhaus, K. Wang, P. Zhou, A. M. Rao, and P. C. Eklund. *Chem. Phys. Lett.*, 206:187, 1993.

[118] G. Benedek and G. Onida. *Phys. Rev. B*, 47:16471, 1993.

[119] A. Grüneis, R. Saito, T. Kimura, L. G. Cançado, M. A. Pimenta, A. Jorio, A. G. Souza Filho, G. Dresselhaus, and M. S. Dresselhaus. *Phys. Rev. B*, 65:155405, 2003.

[120] O. Dubay and G. Kresse. *Phys. Rev. B*, 67:035401, 2003.

[121] G. G. Samsonidze, R. Saito, A. Jorio, A. G. Souza Filho, A. Grüneis, M. A. Pimenta, G. Dresselhaus, and M. S. Dresselhaus. *Phys. Rev. Lett.*, 90:027403, 2004.

[122] N. V. Popov and P. Lambin. *Phys. Rev. B*, 73:085407, 2006.

[123] R. Nicklow, N. Wakabayashi, and H. G. Smith. *Phys. Rev. B*, 5:4951, 1972.

[124] J. L. Wilkes, R. E. Palmer, and R. F. Willis. *J. Electron Spectrosc. Relat. Phenom.*, 44:355, 1987.

[125] C. Oshima, T. Aizawa, R. Souda, Y. Ishizawa, and Y. Sumiyoshi. *Solid State Commun.*, 65:1601, 1999.

[126] S. Siebentritt, R. Pues, K.-H. Rieder, and A. M. Shikin. *Phys. Rev. B*, 55:7927, 1997.

[127] M. Mohr, J. Maultzsch, E. Dobardžić, S. Reich, I. Milošević, M. Damnjanović, A. Bosak, M. Krisch, and C. Thomsen. *Phys. Rev. B*, 76:035439, 2007.

[128] N. B. Brandt, S. M. Chudinov, and Ya. G. Ponomarev. *Semimetals 1: Graphite and its Compounds*. North-Holland (Amsterdam), 1988.

[129] Ç. Ö. Girit and A. Zettl. *Appl. Phys. Lett.*, 91:193512, 2007.

[130] M. Lazzeri, C. Attaccalite, L. Wirtz and F. Mauri . *Phys. Rev. B*, 78:081406, 2008.

[131] N. Bonini, M. Lazzeri, N. Marzari and F. Mauri. *Phys. Rev. Lett.*, 99:176802, 2007.

[132] L. M. Malard and M. A. Pimenta. *in preparation*, 2009.

[133] L. Ravagnan, F. Siviero, C. Lenardi, P. Piseri, E. Barborini, P. Milani, C. S. Casari, A. Li Bassi and C. E. Bottani. *Phys. Rev. Lett.*, 89:285506, 2002.

[134] C. S. Casari, A. Li Bassi, L. Ravagnan, F. Siviero, C. Lenardi, P. Piseri, G. Bongiorno, C. E. Bottani and P. Milani. *Phys. Rev. B*, 69:075422, 2004.

[135] M. Tsuji, T.Tsuji, S. Kuboyama, S.-H. Yoon, Y. Korai, T. Tsujimoto, K. Kubo, A. Mori, and I. Mochida. *Chem. Phys. Lett.*, 355:101, 2002.

[136] F. Cataldo. *Carbon*, 42:129, 2004.

[137] D. Nishide *et al.* *Chem. Phys. Lett.*, 428:356, 2006.

[138] X. Zhao, Y. Ando, Y. Liu, M. Jinno, and T. Suzuki. *Phys. Rev. Lett.*, 90:187401, 2003.

[139] M. Endo, H. Muramatsu, T. Hayashi, Y.-A. Kim, G. Van Lier, J.-C. Charlier, H. Terrones, M. Terrones, and M. S. Dresselhaus. *Nano Lett.*, 5:1099, 2005.

[140] H. Tabata, M. Fujii, S. Hayashi, T. Doi, T. Wakabayashi. *Carbon*, 44:3168, 2006.

[141] C. Fantini, E. Cruz, A. Jorio, M. Terrones, H. Terrones, G. Van Lier, J-C Charlier, M. S. Dresselhaus, R. Saito, Y. A. Kim, T. Hayashi, H. Muramatsu, M. Endo, and M. A. Pimenta. *Phys. Rev. B*, 73:193408, 2006.

[142] T. Pino, H. Ding, F. Güthe and J. P. Maier. *J. Chem. Phys.*, 114:2208, 2001.

[143] A. M. Rao, E. Richter, S. Bandow, B. Chase, P. C. Eklund, K. W. Williams, M. Menon, K. R. Subbaswamy, A. Thess, R. E. Smalley, G. Dresselhaus, and M. S. Dresselhaus. *Science*, 275:187, 1997.

[144] D. Nishide, T. Wakabayashi, T. Sugai, R. Kitaura, H. Kataura, Y. Achiba and H. Shinohara. *J. Phys. Chem. C*, *in press*, 2007.

[145] V. W. Brar *et al.* *Phys. Rev. B*, 66:155418, 2002.

[146] M. Grutter, M. Wyss, J. Fulara and J. P. Maier. *J. Chem. Phys. A*, 102:9785, 1998.

[147] T. Wakabayashi *et al.* *Chem. Phys. Lett.*, 433:296, 2007.

[148] E. Runge and E. K. U. Gross. *Phys. Rev. Lett.*, 52:997, 1984.

[149] J. E. Ridley and M. C. Zerner. *Theor. Chim. Acta*, 32:111, 1972.

[150] S. Yang and M. Kertesz. *J. Chem. Phys. A*, 110:9771, 2006.

[151] C. Adamo and V. Barone. *J. Chem. Phys.*, 110:6158, 1999.

[152] M. J. Frisch *et al.* *Gaussian 03, revision C.02; Gaussian, Inc.*

[153] R. B. Capaz *et al.* *Phys. Rev. B*, 74:121401, 2006.

[154] S. Irle *et al.* *unpublished*.